NUCLEAR STRUCTURE OF PROTON-RICH INTERMEDIATE MASS NUCLEI STUDIED WITH ADVANCED LIFETIME MEASUREMENT TECHNIQUES

By

Christopher Scott Morse

A DISSERTATION

Submitted to
Michigan State University
in partial fulfillment of the requirements
for the degree of

Physics - Doctor of Philosophy

2015

ABSTRACT

NUCLEAR STRUCTURE OF PROTON-RICH INTERMEDIATE MASS NUCLEI STUDIED WITH ADVANCED LIFETIME MEASUREMENT TECHNIQUES

By

Christopher Scott Morse

The transition matrix elements between excited nuclear states provide valuable information about the structure of exotic nuclei. Lifetime measurements are a model-independent way to deduce these matrix elements from experimental data. Two studies of proton-rich nuclei near mass 70 are presented herein using advanced lifetime measurement techniques.

The first study is a measurement of the 8_1^+ and 9_1^+ states in the odd-N, odd-Z nucleus ^{70}As. The lifetimes of these states were determined by the application of the γ-ray lineshape method to γ-γ coincidence data. The states were populated using with the ^{9}Be(^{78}Rb,^{70}As) reaction and γ rays were detected with the Segmented Germanium Array in coincidence with reaction products detected in the focal plane of the S800 Spectrograph. The $B(E1; 8^+ \rightarrow 7^-)$ and $B(M1; 9^+ \rightarrow 8^+)$ transition strengths were deduced and were found to support the assignment of these states to a coupling of the odd proton and neutron in the $g_{9/2}$ orbital.

The second study is a measurement of the 2_1^+ state lifetime in the $N = Z$ nucleus ^{74}Rb. A novel technique called the Differential Recoil Distance Method was used to extract the lifetime from the γ-ray spectra. The next-generation γ-ray detector array GRETINA was used in the experiment, again coupled to the S800 Spectrograph to detect residues from ^{9}Be(^{74}Kr,^{74}Rb) charge exchange reactions. The $B(E2; 2_1^+ \rightarrow 0_1^+)$ strength was calculated and is consistent with the measured strength of the transition between the isobaric analogue states in ^{74}Kr, which may be a signature of shape coexistence in ^{74}Rb.

Copyright by
CHRISTOPHER SCOTT MORSE
2015

AMDG

ACKNOWLEDGMENTS

No work is done in a vacuum, especially when that work comprises several years of one's life. Many people have contributed to this work either directly or indirectly, and it is beyond my capability to acknowledge everyone individually. However, know that if you have talked with me, laughed with (or possibly at) me, sung, studied, worked, played, or otherwise been a part of my life during these past five years, you have helped me reach this point and for that I am grateful.

Special thanks must go first to my advisor, Dr. Hironori Iwasaki, for being a continual source of help and encouragement. Although I knew nothing of nuclear physics at the start of my graduate career, he has always been patient and willing to guide me when I became lost. Being his student has been the opportunity of a lifetime. I also wish to thank the members of my guidance committee, Drs. Alex Brown, Wade Fisher, Alexandra Gade, and Carlo Piermarocchi, for their insightful comments and for always pushing me to become a better scientist. I would also be remiss if I did not acknowledge my undergraduate physics professors at Westmont College. They laid the foundation of my work in physics, and that foundation has proven itself sound.

Many people at the NSCL have been a great help over the years. My fellow Lifetime group members have always been there to listen and discuss, and in some instances to play. Many members of the Gamma group have also acted as mentors to me, for which I am extremely grateful. The staff at the NSCL also deserve no small amount of credit in bringing this document to fruition, as without their tireless efforts there would be nothing to write.

Several individuals have played a pivotal role in bringing me to this place and also deserve recognition. I am indebted to Antoine Lemasson for recognizing that, while I had

the enthusiasm, I lacked both the skill to be a competent programmer and the knowledge to be a capable experimenter. Our impromptu discussions on these and many other subjects were invaluable both for enabling me to be an effective researcher and kindling an interest in programming of which I was only vaguely aware. Second, I wish to extend my heartfelt thanks to Warren Rogers, who introduced me to the idea of studying nuclear physics. Without his invitation to visit the NSCL, I surely would have taken a different path. Similarly, the fact that I chose to study physics at all is due in large part to Chris Sullivan. If not for his enthusiastic exclamation of "Join me!" upon hearing that I was considering a physics major, I might still be stuck doing titrations.

Many friendships have been forged during this journey through graduate school. I have enjoyed immensely the chance to make music with the members of the Grand Canonical Ensemble. I will always remember with fondness the late-night board game sessions and their attendant shenanigans ("MAUOOOOB!"). Likewise, the encounters shared with adventuring companions gathered around the DM screen have formed a staple of my time here at MSU. For those who tolerated my brief stint running a D&D campaign, may our "frondships" endure forever. And for all the other friends I have made, even if our relationship was as simple as shooting the breeze from time to time, thank you for making my time as a graduate student that much more enjoyable.

Last, but certainly not least, my family deserves an immense amount of thanks for their never-ending support. They have endured an inordinate amount of venting and lamentation from me and provided in return a constant stream of optimism and confidence. Without their encouragement, I could not have achieved what I have. I can only hope to be a son and brother worthy of their faithfulness.

TABLE OF CONTENTS

LIST OF TABLES

LIST OF FIGURES

Chapter 1

Introduction

1.1 The atomic nucleus

At the center of every atom is an atomic nucleus. The nucleus carries the positive charge of the atom in the form of electrically positive protons, which keep the electrons bound through the Coulomb force. It also contains neutrons, which are electrically neutral. A given nucleus is labeled in the notation ${}^{A}_{Z}X_{N}$, where X is the chemical symbol which specifies the number of protons Z, N is the number of neutrons, and $A = N + Z$ is the mass number. This label is often abbreviated to ${}^{A}X$, since the number of protons determines the element and hence Z, and N can be determined from $N = A - Z$. The nucleus occupies only a tiny fraction of the atomic volume: typical atomic radii are on the order of angstroms (10^{-10} m) while typical nuclear radii are on the order of 10 femtometers (10^{-14} m). Despite this, nuclei contain nearly all of the mass of the atom (over 99.9%), making them extremely dense. Since only positive charges exist in this dense object, another force must be present which keeps the protons and neutrons (collectively called nucleons) bound. This force is the strong nuclear force, and understanding how it governs nuclear behavior is one of the primary goals of nuclear science.

Just as atoms are arranged according to the number of electrons which they have, nuclei are organized according to the number of protons and neutrons that they contain. This gives rise to the so-called *chart of the nuclides* (sometimes called the *Segrè chart*, after

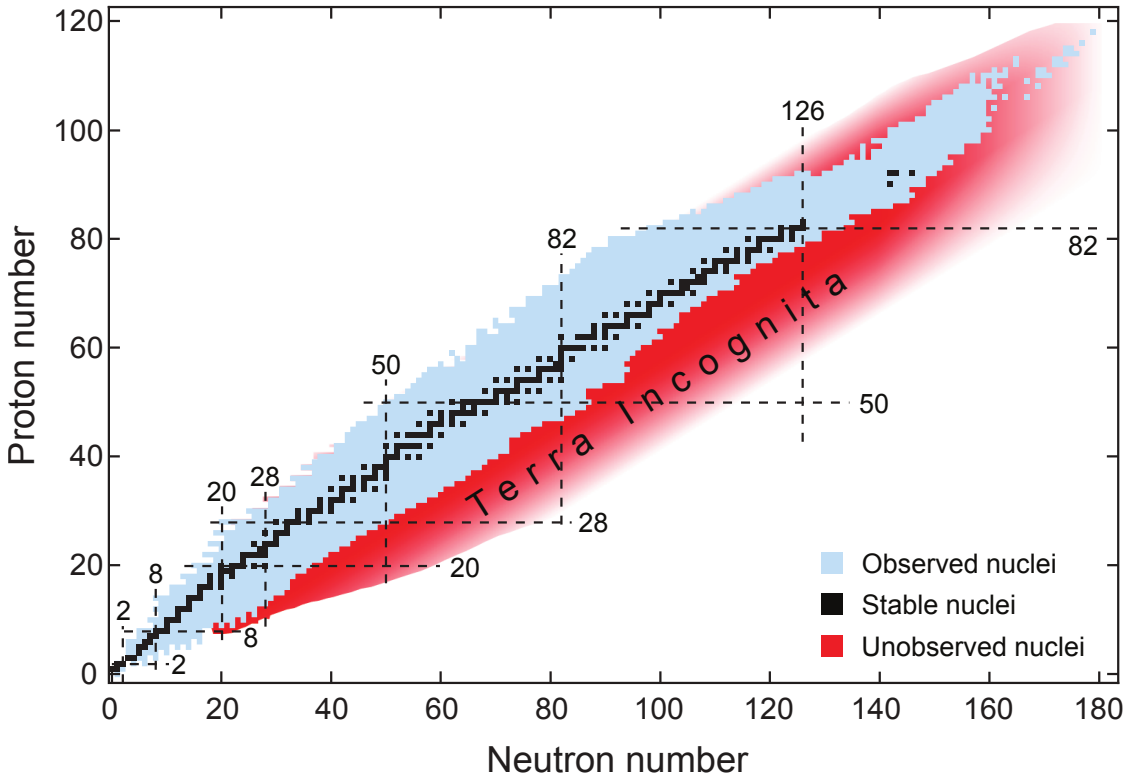

Figure 1.1: A drawing of the chart of the nuclides. The number of protons is plotted on the vertical axis and the number of neutrons on the horizontal axis. The black squares are the stable nuclei, and lie along the so-called "valley of stability." The blue area indicates nuclei which have been observed, while the red area represents nuclei which are predicted to exist but have not been seen experimentally. Finally, the dashed lines indicate the locations of the canonical magic numbers. For interpretation of references to color in this and all other figures, the reader is referred to the electronic version of this dissertation.

Emilio Segrè), shown in Fig. 1.1. In this plot, the nuclei are arranged such that the number of protons in a nucleus is plotted on the vertical axis and the number of neutrons is plotted on the horizontal axis. Rows of nuclei with the same number of protons are called isotopes, while columns of nuclei with the same number of neutrons are called isotones. Nuclei which have the same mass but different numbers of protons and neutrons lie along diagonal lines sloping downward and to the right, and are termed isobars. The black boxes in the figure indicate the stable nuclei, while the blue area represents observed unstable nuclei. The red portion of the figure indicates those nuclei predicted to exist but which have never been

observed. The borders of the shaded area are known as the *driplines* and represent the limits of nuclear binding, beyond which additional nucleons will simply "fall off" the nucleus. The upper left boundary is known as the proton dripline, beyond which no more protons may be added to a nucleus. On the other side of the shaded area is the corresponding neutron dripline, beyond which no more neutrons may be added to a nucleus.

The dashed lines in Fig. 1.1 represent the so-called *magic numbers* of 2, 8, 20, 28, 50, 82, and 126 [1]. Nuclei that have a magic number of either protons or neutrons are called *magic nuclei*, while those that have a magic number of both protons and neutrons are said to be *doubly magic*. Such nuclei exhibit certain unique behavior, such as an increased amount of energy necessary to unbind them compared to neighboring nuclei, as well as higher first excited state energies and smaller transition probabilities between the first excited and ground states (more on this in Sec. 1.3) compared to their neighbors. Together, these traits suggest that magic nuclei are especially stable, and this in turn suggests that some internal organization of the constituent nucleons in a nucleus exists. Understanding and predicting how this structure arises is a natural goal once this observation has been made.

Another noteworthy feature of Fig 1.1 is that the stable nuclei all fall along a relatively narrow band known as the *valley of stability*. These stable nuclei represent only a small fraction of the nuclei depicted on the chart: of the roughly 7000 nuclear systems predicted to exist [2], only about 300 do not undergo spontaneous decay to more stable species. In light systems, the stable nuclei tend to have the same number of protons and neutrons, but for heavier nuclei the valley of stability trends towards having more neutrons than protons. This is because, as more protons are added to the nucleus, a greater number of neutrons are required to balance the increasing contribution of the repulsive Coulomb force. This also explains why the majority of the nuclei that are expected to exist but have so far not been

observed lie on the neutron-rich side of the valley of stability. As protons are added to a nucleus, the Coulomb potential tends to unbind the nucleus, whereas neutrons do not feel the Coulomb potential and so more may be added before the nucleus becomes unbound. For this reason, the location of the proton dripline is determined to a much higher mass than the neutron dripline, which lies much further from stability.

An important feature of the nuclear force is that it is *charge symmetric* and, more generally, *charge independent*. That is to say, the nuclear force does not distinguish between protons and neutrons. It is therefore convenient to introduce a formalism which capitalizes on this feature, and treat protons and neutrons as different states of the same particle, i.e. the nucleon. This formalism is called *isospin*, and the charge independence of the nuclear force is the manner in which the *isospin symmetry* between protons and neutrons is manifested [3, 4]. This symmetry is only approximate, however, since it is violated by the Coulomb potential. In the isospin description of the nucleus, nucleons (both protons and neutrons) have isospin $T = \frac{1}{2}$, but opposite isospin projections T_z. The convention in nuclear physics is to assign neutrons an isospin projection of $+\frac{1}{2}$ and protons a projection of $-\frac{1}{2}$. In this sense, the isospin states of the nucleon are analogous to (and follow the same mathematical rules as) intrinsic spin, and hence the name isospin was given to it.

Just as with angular momentum, the isospin of individual nucleons can be coupled to describe the overall isospin of the nuclear state they comprise. This leads to the concept of isospin multiplets, i.e. groups of states with the same isospin T but different isospin projections T_z. Such states are termed *isobaric analogue states*, and they can be identified by examining the spectra of nuclei with the same number of nucleons but different numbers of protons and neutrons. Figure 1.2 illustrates this concept for several nuclei with mass $A = 58$. The energies of several excited states, for which the contribution of the Coulomb

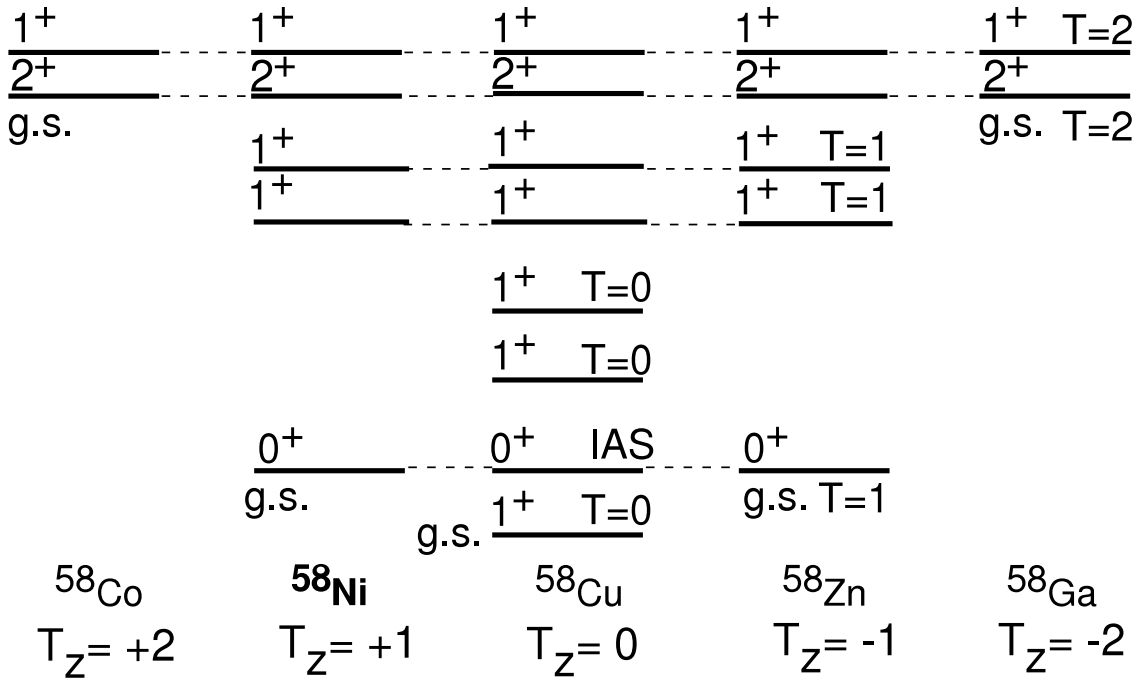

Figure 1.2: A schematic diagram showing a portion of the level schemes for several nuclei with mass $A = 58$, with ^{58}Ni bolded to indicate that it is stable. The levels joined together by dashed lines indicate isobaric analogue states with the indicated value of isospin T. The isobaric analogue states have been drawn at exactly the same energy in this figure to emphasize their relationship with each other, effectively removing the contribution of the Coulomb interaction which violates isospin symmetry. Also shown for the $T_z = 0$ nucleus ^{58}Cu are several $T = 0$ states that have no analogue states and are thus isospin singlet states. Figure is taken and modified from [5].

interaction has been removed, are drawn. The isobaric analogue states are shown connected by dashed lines. As can be seen, the $T_z = 0$ nucleus $^{58}_{29}\mathrm{Cu}_{29}$ has several states without analogues, which are isospin singlet states with $T = 0$. Several other states form triplets in the Ni, Cu, and Zn nuclei with $T = 1$, and higher states form $T = 2$ quintets with all five nuclei represented. In principle, states with isospin up to $T = A/2$ will be present, but in practice such states cannot be observed as they must lie at extremely high excitation energies. However, the identification of the low-lying isobaric analogue states is important because, due to isospin symmetry, the nature of the analogue states should be the same in all nuclei in a multiplet. Therefore, information obtained on one nuclear state in a multiplet

can provide predictions about the other states in the multiplet, thereby giving guidance to experimental studies. This concept will be important for the work presented in Ch. 5.

1.2 Nuclear structure models

The realization that nuclei possess an internal structure leads naturally to a desire to understand and predict this structure. Given that nuclei are composed of quantum mechanical particles, their behavior can, in principle, be predicted by solving the Schrödinger equation for a system of A nucleons:

$$\mathcal{H}\Psi = E\Psi, \tag{1.1}$$

with $\mathcal{H} = T + U$, where T is the kinetic energy and U is the nuclear potential. Unfortunately, while various properties of the nuclear force are known, the exact form of the nuclear potential U is not known. For this reason, a great deal of effort has gone and continues to go into discovering ways to model the nucleus despite not knowing the nuclear potential. As the results of the studies presented within this work are primarily applicable to the study of nuclear structure, a few comments about nuclear structure models are germane to this discussion.

1.2.1 The nuclear shell model

The *nuclear shell model* [6] is perhaps the best known example of a nuclear structure model, and it has been very successful in describing various facets of nuclear structure [7, 8, 9]. In this model, nucleons are organized into groups of orbitals or *shells*. These orbitals are characterized by the quantum numbers of the nucleons that occupy them: the principal (or radial) quantum number n, which denotes the number of times the radial wave function

changes sign; the orbital angular momentum quantum number l, which is usually given in spectroscopic notation such that $l = 0, 1, 2, 3, 4, 5, ...$ is denoted as $s, p, d, f, g, h, ...$; and the total angular momentum quantum number $j = l \pm s$, where $s = \frac{1}{2}\hbar$ is the spin of the nucleon. Since nucleons are fermions, no more than one can have any given combination of quantum numbers in a nucleus. This restricts the number of nucleons that can occupy an orbital to the number of magnetic substates m_j (of which there are $2j + 1$) associated with a given orbital. Orbitals for protons and neutrons are treated separately because these two kinds of particles can be distinguished by their isospin, and are typically denoted with a π for protons or a ν for neutrons. The full notation for a given proton orbital with, e.g. $n = 1$, $l = 2$, and $j = \frac{5}{2}$, would be $\pi 1d_{5/2}$.

Historically, it was the observation of the magic numbers that prompted the development of the shell model. After all, a proper model of the nucleus should be able to reproduce the signature of structure that the magic numbers provide. However, it took some effort to get the model to this point. As shown in Fig. 1.3, the convenient choice of the harmonic oscillator as the nuclear potential proves to be insufficient. The levels drawn on the left-hand side of the figure show that, while the harmonic oscillator does result in certain numbers of nucleons that correspond to filled shells, they do not correspond to the magic numbers. A more realistic potential is the Woods-Saxon potential, which has the form

$$U(r) = \frac{U_0}{1 + \exp(r - R)/a}, \tag{1.2}$$

where U_0 is the depth of the potential well, R is the nuclear radius and a is a parameter that describes the diffuseness of the nuclear surface. The main effect of this potential is to break the degeneracy of the orbitals with different l in the harmonic oscillator, but this

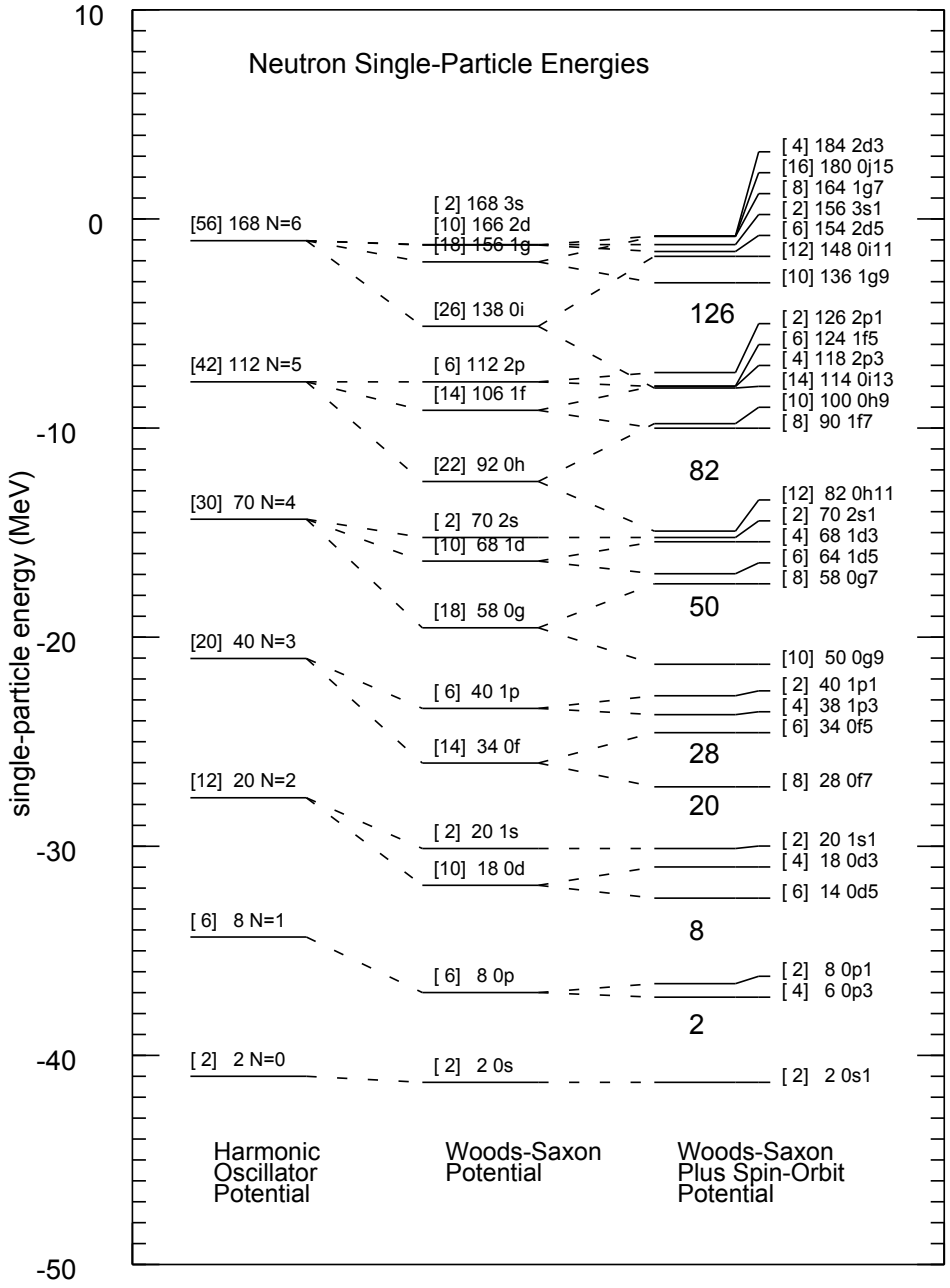

Figure 1.3: The energies of the orbitals generated with several different interactions in the shell model, calculated for ^{208}Pb. In the left and center columns are shown the harmonic oscillator and Woods-Saxon potentials, respectively, neither of which is able to reproduce the correct degeneracy of levels that gives the magic numbers. Adding a spin-orbit term to the Woods-Saxon potential, however, does reproduce the magic numbers, as shown by the column on the right. Figure is taken from [10]

potential still does not reproduce the magic numbers, as shown in the center column of Fig. 1.3. The breakthrough that solved the puzzle came with the addition of a term that couples the intrinsic spin and orbital angular momentum of a nucleon (the so-called *spin-orbit term* [11, 12]): $U_{so} = -U_{so}(r)\vec{l} \cdot \vec{s}$. This term breaks the degeneracy between orbitals with intrinsic spin and orbital angular momentum aligned and antialigned. The right-hand column of Fig. 1.3 shows these energy levels, along with the location of the shell gaps which correspond to the observed magic numbers.

The shell model can be used to make predictions about nuclear structure, such as the nuclear energy levels and transition probabilities between those levels. However, the complexity of the calculations increases very quickly with increasing numbers of nucleons. To make the computational size of the problem tractable, the standard approach in the shell model is to make the assumption that a subset of the nucleons in a nucleus form an inert *core* which does not contribute to the calculation. A common choice is to choose the core to be a doubly magic nucleus close to the nucleus for which the calculation is being performed. The number of particles in the calculation is then reduced to those remaining outside the core, called *valence nucleons*. The number of orbitals available to the valence nucleons (called the *valence space*) is also typically restricted to only a few orbitals above the closed core to further reduce the computational cost of the calculation. To compensate for this truncation of the calculation, *effective interactions* must be developed which make up for the effects of the missing degrees of freedom. The validity of a given effective interaction can be tested by comparing its predictions against experiments. In turn, the results of experiments can prompt the development of new effective interactions.

1.2.2 The Nilsson model

While the shell model has been very successful in describing nuclei which have a spherical shape, a large number of nuclei exhibit non-spherical properties. To describe these nuclei, it is important to have tools that can deal with deformed shapes. One example of such a theoretical tool is the *Nilsson model*, which is an extension of the shell model to non-spherical (but still axially symmetric) potentials [13]. The effect of the non-spherical potential breaks the degeneracy of the states with different projections of the angular momentum, so that each spherical shell model orbital gives rise to $(2j+1)/2$ Nilsson orbitals. Since the orbitals are now distinct, they are given new labels according the scheme $\Omega[Nn_z\Lambda]$, where Ω is the projection of the particle angular momentum onto the symmetry axis of the potential, N is the principal quantum number of the major harmonic oscillator shell (see Fig. 1.3), n_z is the number of nodes of the wavefunction along the symmetry axis direction, and Λ is the component of the orbital angular momentum along the symmetry axis of the potential. The splitting of these orbitals is dependent on both the sign of the deformation (i.e. whether the nucleus is prolate or oblate) and also on its magnitude. For a prolate deformation, the orbitals with the lowest projection of their angular momentum (the lowest Ω) are the lowest in energy, while for an oblate deformation the highest projections are lowered the most.

A diagram showing the Nilsson orbitals for nuclei with $N \approx 82-126$ is shown in Fig. 1.4 and demonstrates the effect of the lowering or raising of the orbitals with different angular momentum projections with changing deformation, which is plotted along the horizontal axis. Notice that for no deformation (i.e. a spherical nucleus) the Nilsson model reverts to the standard shell model with the canonical magic numbers. However, for non-zero deformation, the large gaps between the orbitals corresponding to magic numbers quickly disappear as

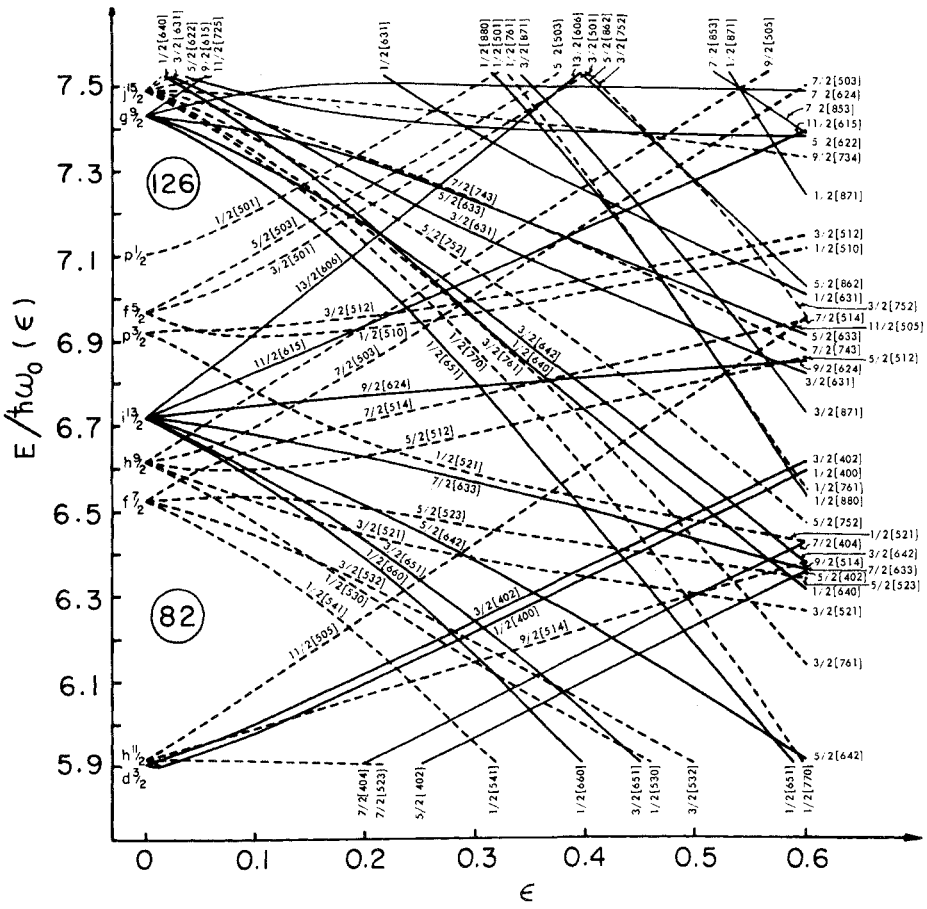

Figure 1.4: A Nilsson diagram showing the single-particle energy levels in the Nilsson scheme, plotted against the deformation parameter along the horizontal axis. For zero deformation, the shell model magic numbers are obtained, but for other deformation parameters (prolate only in this figure), the splitting of the shell model orbitals fills in the gaps between magic numbers, giving rise to a more complicated series of single-particle energy levels. Figure is taken from [14].

the now non-degenerate orbitals quickly fill the space between the spherical single-particle orbitals. However, at certain deformations, new gaps will sometimes open up between the Nilsson orbitals, which can indicate that a nucleus with a certain number of nucleons may experience a particular stability at that value of the deformation. This can be a way to predict the shape of a deformed nucleus associated with a particular nucleon number.

1.2.3 Collective nuclear models

Beyond the microscopic calculations of the shell model and the Nilsson model, attempts to model nuclei have also been made using a macroscopic geometrical description of the nucleus as a whole [15]. This is especially useful for nuclei in which many nucleons are actively determining the properties of the nucleus. Such models are called *collective models* because they attempt to describe the nucleus from the standpoint of a collection of nucleons moving coherently, rather than many independently acting particles. Two such descriptions are especially well-known: the *vibrational model* and the *rotational model*. These models are usually discussed for even-even nuclei, which always have 0^+ ground states and usually have 2^+ first excited states. It is also possible to extend the discussion to odd-A and odd-odd nuclei by considering the coupling of one or a few nucleons to an even-even core.

The vibrational model describes nuclei which, while still spherical, experience oscillations involving many of their constituent nucleons. Most typically, quadrupole vibrations around a spherical shape are considered, although in principle any order vibration could be considered. However, since a dipole term in leading order corresponds only to the overall translation of the nucleus, the quadrupole vibration is typically considered first. The excited states in this model are treated as arising from quadrupole phonon excitations in the nucleus. Starting from the 0^+ ground state, the creation of one phonon produces a 2^+ first excited state (denoted 2_1^+). Creation of another phonon produces a triplet of nearly degenerate states at twice the energy of the 2_1^+ state. These three states arise from the coupling of the two phonons together to gives states with spin-parities of 0^+, 2^+, and 4^+. Adding yet another phonon creates a quintet of states with 0^+, 2^+, 3^+, 4^+, and 6^+ from the coupling of three phonons. As might be expected, these five states are also nearly degenerate with an energy of

three times that of the 2_1^+ state. Generally, the excitation spectrum of a vibrational nucleus has sets of evenly spaced states with energies given by

$$E_n = nE_{2_1^+}, \tag{1.3}$$

where n denotes the number of phonons. Identification of such a spectrum is experimental evidence that a nucleus has a vibrational character.

In a rotational nucleus, the spherical symmetry is broken in the intrinsic frame of reference of the nucleus, which takes on a static deformation. A quadrupole deformation is the most common shape considered, although higher order deformations are also sometimes included. For a quadrupole deformation, the radius of the nucleus is given by

$$R = R_0 \left[1 + \sum_\mu \alpha_\mu Y_{2\mu}(\theta, \phi) \right], \tag{1.4}$$

where R_0 is the undeformed radius, $Y_{2\mu}$ are the second order spherical harmonics, and the α_μ are the coefficients of the expansion of the nuclear shape in spherical harmonics. As with the vibrational nucleus, the center of mass motion is not of interest, and so the expansion coefficients which correspond to it (α_1 and α_{-1}) are set to 0. The remaining coefficients are then parameterized in terms of the quadrupole deformation β and the axial asymmetry γ: $\alpha_0 = \beta \cos\gamma$ and $\alpha_2 = \alpha_{-2} = \beta \sin\gamma$. In this formalism, β denotes the deviation of the nucleus from sphericity along an axis of cylindrical symmetry and is positive-definite. This assumes that the parameter γ takes one of two limiting values: $\gamma = 0^\circ$ or $\gamma = 60^\circ$. If $\gamma = 0^\circ$, then $\beta > 0$ corresponds to a nucleus with an elongated ellipsoidal or *prolate* shape. Conversely, $\gamma = 60^\circ$ and $\beta > 0$ corresponds to a compressed or *oblate* shape. In both cases,

the nucleus remains rotationally symmetric about the axis of deformation. For $0^\circ < \gamma < 60^\circ$, however, the nucleus becomes *triaxially deformed* and is no longer rotationally symmetric about any axis. With the nucleus now statically deformed, it can have excited states based upon its rotation. For axially symmetric nuclei (the majority of nuclei), the energy levels of a rotational nucleus are given by

$$E(J) = \frac{\hbar^2}{2I} J(J+1), \tag{1.5}$$

where I is the moment of inertia for a nucleus of the appropriate shape. Such level schemes are well-known in many nuclear systems [16] and serve as a reliable method of identifying rotation of nuclei.

1.3 Lifetime measurements

Just as a wide variety of models exist to predict nuclear structure, a large number of techniques have been developed to measure it. This dissertation focuses on studies using one particular category of these techniques: the measurement of the lifetimes of excited nuclear states. This section will briefly describe the utility of lifetime measurements in general and their connection to nuclear structure. An overview of some of the techniques used in lifetime measurements, including those used in this work, will be presented in Ch. 2.

In studying nuclear structure, one often desires to get information about the construction of states of a given nucleus. Lifetime measurements provide a particularly transparent approach for gaining such insights. The connection of the lifetime to the nuclear structure

is given by the equation

$$\frac{1}{\tau_i} = T_{i\to f} = \sum_{\lambda,\pi} k_{\lambda\pi} E_\gamma^{2\lambda+1} \frac{|\langle J_f||\mathcal{M}(\pi\lambda)||J_i\rangle|^2}{2J_i+1},$$
$$k_{\lambda\pi} = \frac{8\pi(\lambda+1)}{\lambda[(2\lambda+1)!!]^2\hbar(\hbar c)^{2\lambda+1}}. \tag{1.6}$$

In this expression, the mean lifetime τ_i of the initial state i is the inverse of the transition rate $T_{i\to j}$ between the initial state i and final state f. The expression on the right gives this transition rate in terms of a sum over all the allowed multipolarities λ allowed in the transition as well as the character π of the decay, where $\pi = E$ for an electric transition and $\pi = M$ for a magnetic transition. The matrix element on the right gives the overlap of initial and final wavefunctions of the nuclear states connected by the electromagnetic transition operator $\mathcal{M}(\pi\lambda)$. For electric type decays, this operator takes the form

$$\mathcal{M}(E\lambda) = \sum_j e_j r_j^\lambda Y_{\lambda\mu}, \tag{1.7}$$

and for magnetic decays

$$\mathcal{M}(M\lambda) = \sum_j \left[g_j^s \vec{s}_j + \frac{2}{\lambda+1} g_j^l \vec{l}_j \right] \cdot \vec{\nabla}[r^\lambda Y_{\lambda\mu}]\mu_N. \tag{1.8}$$

In these expressions, $Y_{\lambda\mu}$ are the spherical harmonics, e_j is the charge of the j^{th} nucleon, μ_N is the nuclear magneton, and g_j^s and g_j^l are the spin and orbital gyromagnetic ratios, respectively. The operators $\vec{s}_j$ and $\vec{l}_j$ are the spin and orbital angular momentum operators for the j^{th} nucleons, respectively.

Certain selection rules govern the permissible multipolarities for a given transition. The

$Y_{\lambda\mu}$ can only connect states with spin J_i and J_f that differ by at most λ. This is often expressed as the so-called *triangle condition*

$$|J_i - J_f| \leq \lambda \leq J_i + J_f. \tag{1.9}$$

Turning this statement around, a transition that connects states that have a difference in angular momentum ΔJ must have multipolarity $\lambda \geq \Delta J$. Since photons have an intrinsic angular momentum of one unit, $\lambda = 0$ is forbidden and therefore $J_i = 0 \rightarrow J_f = 0$ transitions cannot proceed by γ decay. The parities of the states involved are also important and determine the electric or magnetic character of the decay. When the parities π are such that $\pi_i \pi_f (-1)^\lambda$ is even, the transition must be of the electric type, otherwise it is magnetic.

The last fraction on the right of Eq. 1.6 is the so-called *reduced transition strength* and is commonly given the symbol $B(\pi\lambda)$:

$$B(\pi\lambda) = \frac{|\langle J_f||\mathcal{M}(\pi\lambda)||J_i\rangle|^2}{2J_i + 1}. \tag{1.10}$$

This quantity is the one that contains the nuclear structure information. When discussing nuclear structure, it is common to do so in terms not of the lifetime itself, but of the transition strength which is derived directly from the lifetime:

$$B(\pi\lambda) = \frac{k_{\pi\lambda}}{\tau E_\gamma^{2\lambda+1}}. \tag{1.11}$$

With this expression, the transition strength and therefore the nuclear structure can be discussed so long as one knows the energy of the transition, the lifetime of the initial state, and the electric/magnetic character and multipolarity of the transition. Typically, the transition

energy is one of the first experimental observables obtained for a given level, and the character of the decay is often not far behind. The lifetime is usually measured last, and constitutes the final piece of information necessary to calculate the transition strength.

Finally, having defined the transition strength and its relationship to lifetime measurements, a word about the insight that these quantities can give about nuclear structure is in order. First, since the transition strength is directly related to the overlap of the wavefunctions of the states involved in the transition, the transition strength provides insight into the configuration of the nuclear states. It also provides a method for direct comparison with theoretical predictions of the transition strength made using wavefunctions calculated with any appropriate nuclear model, including those discussed above. Agreement between theory and experimental results then offers a way to test whether the calculated wavefunctions accurately describe the physical states. Even without theoretical calculations, however, transition strengths are still a valuable tool for interpreting the results of experiments. The relative strength (or weakness) of a transition can be judged by expressing it in so-called *single-particle units* or *Weisskopf units* [17]. The Weisskopf unit is an estimate of the strength that would be observed for a given transition assuming that it is due to only a single nucleon. The expressions for the Weisskopf estimate for electric and magnetic transitions are given by [18]

$$\begin{aligned} B(E\lambda) &= \frac{1}{4\pi}\left(\frac{3}{\lambda+3}\right)^2 (1.2A^{1/3})^{2\lambda}\ e^2\mathrm{fm}^{2\lambda} \\ B(M\lambda) &= \frac{10}{\pi}\left(\frac{3}{\lambda+3}\right)^2 (1.2A^{1/3})^{2\lambda-2}\ \mu_N^2\mathrm{fm}^{2\lambda-2}. \end{aligned} \tag{1.12}$$

If a transition is observed to have a strength which is comparable to the single-particle estimates given here, it can be taken as an indication that single-particle degrees of freedom may be appropriate to describe the nuclear behavior. However, if the measured strength

deviates from this estimate by an order of magnitude or more, then it can be an indication that the structure of the nucleus is significantly different than that which a single-particle picture would predict. In this way, the structure of nuclear states can be discussed even when detailed theoretical information is missing.

The specific case of electric quadrupole ($B(E2)$) transition strengths is especially interesting from the perspective of studying nuclear structure. In particular, for an even-even nucleus, the ground state always has a spin-parity of 0^+ and frequently the first excited state will be 2^+. Therefore, the lowest multipole transition that can connect these two states is an electric quadrupole transition, and this can be used to quantify the collective nature of the nucleus. For quadrupole collectivity as described in Sec. 1.2.3, transitions between states involve many nucleons acting coherently, and so the transition strength is significantly enhanced over the single-particle estimate. The observation of such an enhancement can therefore be taken as evidence for the collective nature of the nucleus being studied. Furthermore, for a statically deformed nucleus, the $B(E2)$ can be related to the quadrupole deformation parameter β [19]:

$$B(E2; 2_1^+ \rightarrow 0_1^+) = \frac{1}{5}\left\{\frac{3}{4\pi} Z e R_0^2 \beta\right\}^2, \tag{1.13}$$

where R_0 is the undeformed nuclear radius. Because of this sensitivity to the deformation and the collectivity in general, $B(E2; 2_1^+ \rightarrow 0_1^+)$ values provide valuable insight into the structure of nuclei.

The remainder of this work will focus on the application of lifetime measurements to understand nuclear structure. Two studies will be presented: one on the nucleus ^{70}As and one on ^{74}Rb. These proton-rich nuclei lie in a portion of the nuclear chart which is known

to be a site of many nuclear structure phenomena. Some nuclei can be described well using the single-particle language of the shell model, while others necessitate the use of collective descriptions. In addition, the transition between these behaviors can be abrupt, both as a function of the nucleons that make up a nucleus as well as the excitation energy present in the system. However, these nuclei also present a challenge to experiment and theory alike. On the experimental side, the nuclei near mass $A \approx 70$ near the proton dripline can be hard to produce in sufficient quantities to study. In addition, the nuclei in this work have an odd number of both protons and neutrons, and such nuclei usually exhibit very complicated spectra which can hinder analyses. From a theoretical standpoint, the rapid evolution of nuclear structure in this region makes it difficult to create a universal description which can simultaneously reproduce the features of all of these nuclei. These systems also have enough nucleons that they require quite large model spaces for microscopic calculations such as the shell model, which in turn requires a great deal of effort to keep the computational requirements tractable. The work detailed in this dissertation is intended to contribute to the solution of this situation from the experimental side. The results of the analyses provide important information about the structure of the nuclei studied herein and help to improve the understanding of nuclear structure in this region. In addition, the methods used to perform these studies constitute a contribution in their own right. Both are lifetime measurements that are advanced versions of their more well-known counterparts intended to solve specific problems frequently encountered in nuclear spectroscopy. The next chapter will go into detail about lifetime measurements in general, and will also introduce these two methods and their utility. Following that, the equipment necessary for these studies will be reviewed, and then each of the studies presented in turn. Finally, some closing remarks will be made about the results of these studies and the future prospects they present.

Chapter 2

Lifetime Measurement Techniques

The measurement of the lifetimes of nuclear states has led to the development of a wide variety of experimental techniques. One of the driving factors of this proliferation of techniques is the rather large range of values that these lifetimes can take, such that multiple methods have been necessary to cover as much of the spectrum of lifetimes as possible. In addition, since a nucleus can decay through multiple channels, it has been necessary to develop methods which are tailored to specific kinds of nuclear decays in order to measure their lifetimes. Figure 2.1 shows several techniques for measuring lifetimes along with the approximate range of lifetimes which can be measured with that technique. This chapter will introduce and give a brief summary of a few common methods for measuring excited state lifetimes, focusing mostly on those involving the detection of γ rays. After that, the two methods used in the experiments described in this work will be covered: the *lineshape* method and the *Differential Recoil Distance* method.

2.1 Overview of lifetime measurements

Despite the great variety of strategies for measuring lifetimes, all lifetime experiments seek to answer the same question: Given that excited nuclear states follow the law of radioactive decay,

$$N = N_0 e^{-t/\tau}, \tag{2.1}$$

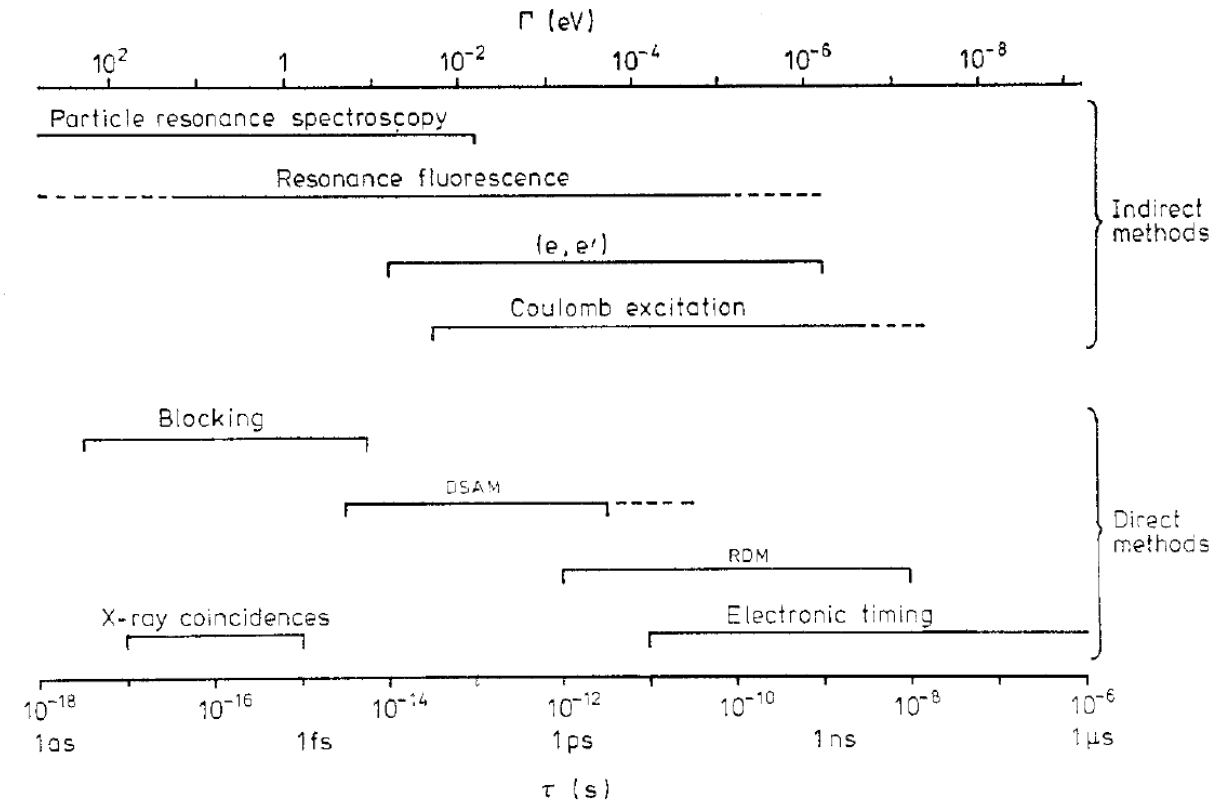

Figure 2.1: A diagram showing the approximate ranges in which various lifetime measurement techniques are effective. The methods labeled "direct" measure the lifetime itself, whereas the "indirect methods" measure the width $\Gamma = \hbar/\tau$ or cross-sections of electromagnetic transitions. Figure is from [20].

how can the lifetime τ be extracted from the experimental data? The answer to this question is very much dependent on the details of the state being analyzed, including the level scheme of the nucleus, the difficulty of populating the state, and the value of the lifetime itself. An additional complication presents itself when using secondary beams of rare isotopes, as the intensities of such beams are usually limited and the beam emittance (that is, the distribution of the beam in position and momentum space) can be large. This section will briefly introduce a few of the more common methods employed to measure lifetimes in nuclear physics. More specifically, since this dissertation is focused on direct methods for lifetime measurements with fast rare isotope beams, the indirect methods shown in Fig. 2.1 will not be discussed.

In addition, the blocking and X-ray coincidence techniques listed in Fig. 2.1 will also be omitted, as they are suited for lifetime measurements orders of magnitude shorter than the lifetimes presented herein. The interested reader is referred to [20] for a review of these methods.

2.1.1 Electronic timing measurements

Perhaps the most conceptually straight-forward method of measuring the lifetime of a nuclear state is by directly measuring the time difference between two signals, one which corresponds to the population of the state and another to its depopulation. This kind of measurement is called an *electronic timing measurement*. Broadly speaking, there are two methods used within the category of electronic timing methods: the *slope method*, used for longer lifetimes greater than about 1 ns, and the *centroid shift method*, for shorter lifetimes less than about 1 ns [20]. Of necessity, this discussion of electronic timing measurements will be brief, but much more information can be found in Ref. [21], from which this discussion is largely drawn.

In general, the timing signals generated by any detector system are subject to some level of fluctuation, due both to the intrinsic timing characteristics of the detector system and to the electronics used with it. Therefore, even for two radiation signals emitted simultaneously, there is some finite width associated with the distribution of timing signals recorded by the radiation detectors that sense this radiation. This distribution is known as the *prompt time distribution* (PTD) or *prompt response function* (PRF). This is typically characterized by the full width at half maximum of the distribution, which may also be referred to as the "time resolution," and an exponential tail which has some characteristic decay constant called the "apparent half-life ($\tau_{1/2}$)" or the "slope" of the distribution. It is the slope of the PTD that determines which of the methods listed in the previous paragraph will be

used. If the apparent half-life of the PTD is small compared to the half-life of the state to be measured, then the slope method can be used. On the other hand, if this is not the case, then the difference between the centroids of the PTD and the time distribution of the delayed signal from the decaying state can be used to measure the lifetime. As stated in [20], centroid shifts as small as 0.5% of the FWHM of the PTD may be measured in this fashion. For reference, values for the FWHM of the PTD may be a few hundred picoseconds for scintillator detectors, while for germanium detectors this may be several nanoseconds. Typical values of the apparent half-life are tens to around 100 ps for scintillators, and several hundred picoseconds for germanium detectors.

Mathematically, the problem can be stated as an analysis of the time spectrum of the delayed coincidence events $F(t)$, which is a convolution of the PTD $P(t)$ and an exponential function $f(t)$ with lifetime τ:

$$f(t) = (1/\tau)\exp(-t/\tau), \tag{2.2}$$

for $t \geq 0$ and 0 for $t < 0$. The function $F(t)$ can then be written as

$$F(t) = \int_0^\infty f(t')P(t-t')dt', \tag{2.3}$$

as long as $F(t)$, $P(t)$, and $f(t)$ have their areas normalized to unity. The time delay $t - t'$ in Eq. 2.3, which is just due to the width of the PTD, can be eliminated by the substitution $y = t - t'$, and further substituting in $f(t)$ gives

$$F(t) = 1/\tau \exp(-t/\tau) \int_{-\infty}^{t} \exp(y/\tau)P(y)dy, \tag{2.4}$$

which when differentiated yields

$$\frac{dF(t)}{dt} = \frac{P(t) - F(t)}{\tau}. \tag{2.5}$$

Moving $F(t)$ to the left side, it can be seen that

$$\frac{d \ln F(t)}{dt} = \frac{dF(t)/dt}{F(t)} = -\frac{1}{\tau}\left(1 - \frac{P(t)}{F(t)}\right). \tag{2.6}$$

Equation 2.6 gives the condition for using either the slope method or the centroid shift method. Specifically, as stated earlier, at those times when the prompt timing distribution makes a negligible contribution to the overall decay curve, i.e. when $F(t) \gg P(t)$, then the slope method can be used. In this case, the lifetime is found simply as

$$\frac{d[\ln F(t)]}{dt} = -\frac{1}{\tau}, \tag{2.7}$$

and can be obtained from the slope of the function $F(t)$ on a logarithmic plot at points sufficiently far from the prompt timing curve.

For cases when the lifetime to be measured is small compared to the decay time of the prompt timing distribution, then the condition $F(t) \gg P(t)$ is never fulfilled. In this case, the centroid shift method can be used. With this technique, the lifetime is given by the difference of the first moments (centroids) of the delayed time distribution $F(t)$ and the prompt time distribution $P(t)$. This result is not particularly difficult to derive. The first moment of Equation 2.3 is

$$\mathcal{M}^{(1)}[F(t)] = \int_{-\infty}^{\infty} tF(t)dt. \tag{2.8}$$

From Eq. 2.5, this integral can be rewritten as

$$\mathcal{M}^{(1)}[F(t)] = \int_{-\infty}^{\infty} t \left(P(t) - \tau \frac{dF(t)}{dt} \right) dt. \tag{2.9}$$

The term on the left is the first moment of $P(t)$, while the term on the right can be integrated by parts:

$$\mathcal{M}^{(1)}[F(t)] = \mathcal{M}^{(1)}[P(t)] - \tau \left\{ tF(t)\big|_{-\infty}^{\infty} - \int_{-\infty}^{\infty} F(t)dt \right\}. \tag{2.10}$$

Because $F(t)$ is normalized to unit area, the last integral in this expression is unity. Since $f(t) = 0$ for $t < 0$, the lower evaluation limit in the first term in brackets can be set to zero:

$$\mathcal{M}^{(1)}[F(t)] = \mathcal{M}^{(1)}[P(t)] - \tau \left\{ tF(t)\big|_{0}^{\infty} - 1 \right\}. \tag{2.11}$$

Physically, the delayed time spectrum $F(t)$ must approach zero for very long times t, since the population of a radioactively decaying state must eventually approach zero. The first term in the brackets therefore vanishes at both the upper and lower limits, leaving the desired relation:

$$\tau = \mathcal{M}^{(1)}[F(t)] - \mathcal{M}^{(1)}[P(t)]. \tag{2.12}$$

This simple expression is attractive because all that is required to determine the lifetime is to read off the centroids of the two distributions $F(t)$ and $P(t)$. However, care needs to be taken in practice to avoid systematic errors when the centroids of the distributions become very close to each other, as noted in [20, 21]. It has also been shown that higher moments of $F(t)$ and $P(t)$ may be used in the analysis [22]. Under the right circumstances this can allow the lifetime to be analyzed even when the PTD is not known very precisely, but systematic

errors may become large. More details can be found in [21].

2.1.2 The Recoil Distance Method

The Recoil Distance Method (RDM), originally described in Ref. [23] and in more detail in Ref. [24], is applicable to the measurement of lifetimes in the range from a few picoseconds to nanoseconds and is described in its modern incarnation in Ref. [25]. Although there is some overlap with electronic timing methods in terms of the lifetimes which can be measured, the RDM represents a very different measurement paradigm than the electronic methods of the previous section. In particular, rather than attempting to directly measure the time delay between the creation and destruction of an excited state, which is quite challenging for picosecond lifetimes, the RDM transforms the problem into one of measuring distances. This takes advantage of the fact that an excited nuclear state is often created "in-flight" by reaction of a moving nucleus on a fixed target. Assuming the reacting nucleus is not stopped in the target material, it will recoil out of the target into vacuum, where it will have a well-defined velocity. If the lifetime and the velocity are large enough, then the average distance this nucleus will travel before decaying becomes macroscopic and can be measured accurately. The problem is therefore translated from evaluating challengingly short times to determining measurable distances.

The challenge of measuring the distance that the decaying nuclei travel still remains. To solve this problem, the concept of a device which is called a "plunger" was developed, illustrated in Fig. 2.2. These devices are designed to mount two foils in the beamline and position them very precisely. The first foil that the beam encounters is called the target and is used to populate excited states of the nucleus to be studied. The function of the second foil is to change the velocity of the recoiling nucleus. For a low-energy study, the beam

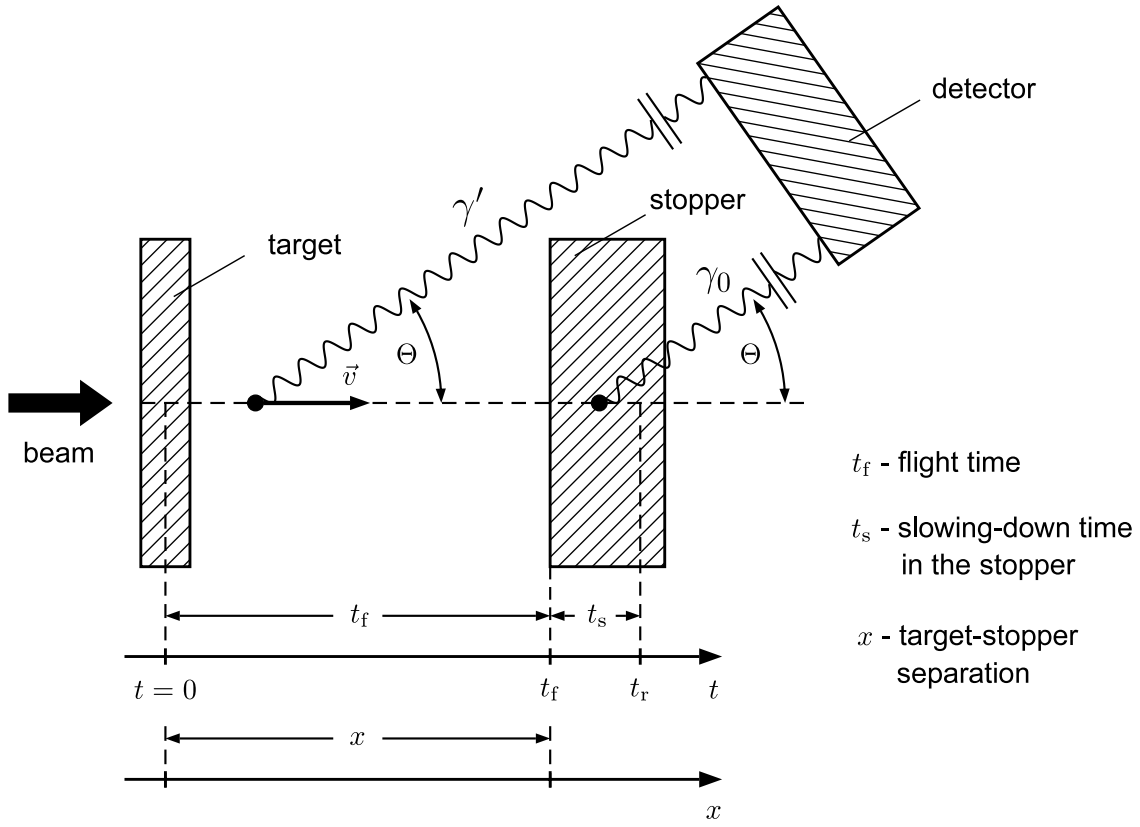

Figure 2.2: An illustration of the concept of the plunger setup for measuring the lifetimes of excited nuclear states. A beam of nuclei comes from the left and interacts with a target foil, producing the excited states to be studied. The beam then recoils out of the target, emitting γ rays as it travels toward a second foil. In this figure, the beam is stopped in the second foil, where any nuclei which have not yet decayed will do so. Both Doppler shifted and non-Doppler shifted photons are detected, and the ratio of the shifted and unshifted photons gives the sensitivity to the lifetime. Figure is from [25].

velocity is typically a few percent of the speed of light, in which case the recoiling nucleus is brought to rest in the second foil. In this case, the second foil is called a "stopper." In a high-energy experiment, which is more typical of the experiments performed at the NSCL where the beam velocity is closer to 30% of the speed of light, the recoiling nucleus will pass through the second foil. For these experiments, the second foil is called a "degrader." In either case, the reaction of the beam in the target defines a time $t = 0$. The second foil is placed at a precisely measured distance D from the target, and if the velocity of the nucleus as it recoils out of the target is known, then the time $t = D/v$ at which it reaches the second

target is well-determined. The number of excited states which decay before the nucleus is slowed or stopped in the second foil is governed by the lifetime. By systematically changing the distance between the two foils during the experiment, the number of decays observed as a function of distance can be mapped out, converted to a function of time, and the lifetime extracted.

In principle, any method of detecting the decay of an excited state in a nucleus can be used with the RDM, so long as it is sensitive to whether the decay happens before or after the nucleus encounters the degrader/stopper. In practice, this most often involves the detection of γ rays that are emitted as the nucleus decays to lower energy states. However, some experiments have detected other radiations for the purposes of measuring lifetimes, for example, from a proton-emitting nucleus [26]. Whatever the radiation detected, however, it is necessary to determine whether it is emitted before or after the second foil is reached. For the most common case of detecting photons, this can be done by noting that those nuclei which decay before reaching the second foil do so in-flight, and therefore the γ-rays they emit will be Doppler shifted according to

$$E_\gamma^{lab} = \frac{E_\gamma^{cm}}{\gamma(1 - \beta \cos\theta_{lab})}, \tag{2.13}$$

where E_γ^{cm} is the photon energy in the center-of-mass frame, θ_{lab} is the laboratory-frame angle at which the photon is emitted relative to the velocity vector of the nucleus, β is the velocity of the nucleus as a fraction of the speed of light, and $\gamma = (1-\beta^2)^{-1/2}$ is the Lorentz factor. On the other hand, those nuclei that decay after encountering the second foil will exhibit either no Doppler shift if the second foil is a stopper or a reduced Doppler shift if the second foil is a degrader. Therefore, in the γ-ray spectrum, there will be two photopeaks

associated with the decay of each excited state which is populated in the nucleus: the shifted peak for those nuclei decaying in-flight and the unshifted or less shifted peak for those nuclei that decay after reaching the second foil. The number of decays happening before and after reaching the second foil (and hence the lifetime of the state being studied) can then be determined from the areas of the two peaks.

As it was originally stated [23], the mathematical justification for the Recoil Distance Method is very simple. If the total number of γ rays observed from an excited state is given by I_0, then the number of counts in the Doppler shifted peak is given by

$$I_s = I_0(1 - \exp(-D/v\tau)) \tag{2.14}$$

and the counts in the unshifted peak (assuming a stopper is used) is

$$I_u = I_0 \exp(-D/v\tau). \tag{2.15}$$

If these two quantities are measured for several different distances D, then the ratio

$$R(D) = \frac{I_u}{I_s + I_u} = \exp(-D/v\tau) \tag{2.16}$$

can be constructed as a function of D and the lifetime can be extracted from this function. However, this doesn't take into account the possibility of feeding from higher-lying states. As written in Ref. [25], a more general approach can be taken to find the correct lifetime. In this case, if the level of interest is L_i, the higher-lying levels are L_h, and the levels to which

L_i decays are L_j, the population of the level L_i is governed by the differential equation

$$\frac{dn_i(t)}{dt} = -\lambda_i n_i(t) + \sum_{h=i+1}^{N} \lambda_h n_h(t) b_{hi}, \tag{2.17}$$

where N denotes the highest state considered, $\lambda_k = 1/\tau_k$ is the decay constant of the state k, and b_{hi} is the *branching ratio* which indicates the fraction of the population of the state h which decays to state i. Each of the higher states is also governed by a similar differential equation, so that a system of coupled differential equations must be solved in order to find the lifetime of the state i. The solution to this system of equations is given by

$$R_i(t) = P_i \exp(-t\lambda_i) + \sum_{h=i+1}^{N} M_{hi}[(\lambda_i/\lambda_h)\exp(-t\lambda_h) - \exp(-t\lambda_i)], \tag{2.18}$$

where P_n is the direct population of the state n which is not due to feeding and the term on the right describes the feeding to this state, with

$$M_{hi} = \frac{1}{\lambda_i/\lambda_h - 1}\left\{ b_{hi}P_h - b_{hi}\sum_{m=h+1}^{N} M_{mh} + \sum_{m=i+1}^{h-1} M_{hm} b_{mi}(\lambda_m/\lambda_h) \right\}. \tag{2.19}$$

In this last equation, the first term quantifies the direct population of the feeding state h, the second term accounts for even higher-lying states that feed h, and the last term describes any feeding of i by h through any intermediate states. Practically speaking, what this means is that the data from an experiment with significant feeding must be fit with many parameters, so that the lifetime, populations, and branching ratios for each state are extracted from the data if they are not already known.

2.1.3 The Doppler Shift Attenuation Method

For lifetimes of nuclear states that are shorter than about one picosecond, measurements that rely on the excited nuclei recoiling into vacuum become difficult. This is due to the fact that a significant number of the excited states will decay before the nucleus exits the target, and so a different approach is necessary. The Doppler Shift Attenuation Method (DSAM) is applicable in this circumstance and makes use of the fact that the recoils are decaying in-medium. As the excited nuclei pass through the target material, they will be slowed due to interactions with the target, with the consequence that the γ rays that are emitted as they relax will have a continuous distribution of Doppler shifts according to the characteristic timescale of the decay, which is just the lifetime of the state. Likewise, if the beam velocity as it enters the target is chosen appropriately, then it will be stopped inside the target with its own characteristic time scale. Comparing this stopping timescale, which is known in principle, to the timescale exhibited by the distribution of Doppler shifts of the photons from the decaying nucleus allows the lifetime to be extracted.

Practically speaking, the DSAM is based upon the measurement of the average velocity $\overline{v}$ with which the excited states being studied decay. This is then used to define a function $F = \overline{v}/v_0$, with v_0 the initial velocity of the nucleus [27]. An experimental measurement of this function can be made in one of two ways. In the first method, the centroid of the observed Doppler shifted γ-ray spectrum may be measured and used to determine $\overline{v}$ according to

$$\overline{E}_{\gamma}^{lab} = \frac{E_{\gamma}^{cm}}{\gamma(1 - \overline{\beta}\cos\theta)}. \tag{2.20}$$

The measured value of F can then be compared with a theoretically calculated value of F using stopping theory. In the second case, the lifetime can be determined by fitting the

lineshape of the γ-ray spectrum to a theoretical lineshape, again calculated using stopping theory, and which may generated using Monte Carlo methods [28]. In either case, it is important to understand the stopping theory (e.g. [29, 30]) used as well as the stopping powers they predict so that any possible uncertainties from this theory can be quantified.

Some insight into the nature of the dependence of the DSAM on stopping theories can be gained by considering the actual form of the function F, which is

$$F = \frac{\overline{v}}{v_0} = \frac{1}{v_0 \tau} \int_0^\infty v(t) \exp(-t/\tau)\, dt. \tag{2.21}$$

From this, it can be seen that to evaluate F, it is necessary to know the functional form of the velocity as a function of time. As a first approximation, the energy loss in the material can be assumed to be proportional to the velocity, $dE/dx \propto v$, if the velocity is around 1% the speed of light [27]. This leads to the result that the velocity as a function of time behaves exponentially, $v(t) = v_0 \exp(-t/\alpha)$, where α in this expression represents the characteristic slowing down time of the material. Inserting this into Eq. 2.21 and evaluating the integral results in

$$F = \frac{1}{1 + \tau/\alpha}. \tag{2.22}$$

As stated in [27], most solids have a characteristic slowing down time around 3×10^{-13} to $\sim 10^{-12}$ seconds. If values of F in the range 0.1 to 0.9 are those which can be determined with sufficient accuracy, then the lifetimes that lie within the measurable range within this assumption are roughly 10^{-14} to $\sim 10^{-11}$ seconds. However, the assumption that the velocity change is exponential is not necessarily valid. It is valid for velocities of about 1% of the speed of light, where the energy loss is chiefly due to electronic stopping. However, for higher velocities the energy loss scales more slowly with velocity, and for lower veloci-

ties nuclear stopping comes into play. Unfortunately, the treatment of the nuclear stopping necessarily involves making approximations, and therefore DSAM measurements are inherently dependent upon the choice of some model. Nevertheless, DSAM is an important tool for measuring lifetimes of femtosecond (10^{-15} s) order since few other direct methods can measure lifetimes of less than one picosecond, as shown by Fig. 2.1. For more details and further discussion of the stopping models used, see Refs. [20, 27].

2.2 The Lineshape Method

As described in Ch. 4, one of the goals of the experiments covered by this work was to measure the lifetime of some of the excited states in ^{70}As. In order to accomplish this goal, a lifetime measurement technique known as the *lineshape method* [31, 32] was used and applied to rare isotope beams. Depending upon the experimental conditions, this technique can be applied to lifetimes in the range of a few tens of picoseconds to a few nanoseconds. This section will describe the lineshape method in detail as it was used in the ^{70}As experiment.

As with many of the methods used to measure prompt γ rays, the lineshape method is predicated upon the fact that photons emitted from a source moving at relativistic speeds will be Doppler shifted, such that the energy of the γ rays emitted in the rest frame of the nucleus is related to the energy of the photons in the lab frame by the expression

$$E_\gamma^{cm} = \gamma(1 - \beta\cos\theta)E_\gamma^{lab}, \tag{2.23}$$

where β is the velocity of the emitting nucleus expressed as a fraction of the speed of light, θ is the angle (in the lab frame) at which the photon is emitted relative to the trajectory

of the nucleus, and γ is the Lorentz factor. In a typical experimental setup, the radioactive isotopes which are to be studied are produced by passing a beam of nuclei through a thin piece of target material to induce nuclear reactions. If these reactions result in nuclei in excited states, the nuclei will quickly relax to their ground state, mostly by the emission of one or more photons. Since many of these photons will be emitted extremely quickly, Eq. 2.23 is used to reconstruct the energy of the photons in the center of mass frame of the nuclei assuming that the angle of emission θ can be measured from the target position. For short-lived states this is a good assumption, but for sufficiently long-lived states the nucleus may travel a significant distance from the target before it decays. In this case the assumption of emission at the target is no longer valid and the measured emission angle no longer corresponds to the true one.

While incorrect Doppler correction is normally considered a liability, the lineshape method makes use of it to extract useful information. For a sufficiently long-lived state, the observed and true emission angle will differ enough that an observable shift in the reconstructed energy will appear. In addition, where normally a sharp peak would be present for a properly Doppler corrected γ ray, a long-lived state will produce a peak which is broadened in such a way that it acquires a low-energy tail. This shift in the peak energy and the shape of the tail are characteristic of the lifetime of the decay, and therefore can be used to deduce the lifetime of the state. Figure 2.3 shows typical lineshapes for decays with 10 ps, 100 ps, and 1000 ps lifetimes for decaying nuclei with a velocity of about 30% of the speed of light. As can be seen from the figure, while there is no low-energy tail for the 10 ps lifetime, the 100 ps lifetime has a small tail, and the 1000 ps lifetime has a prominent tail. This demonstrates the sensitivity of the γ-ray spectral shape to the lifetime.

For the purposes of this dissertation, however, the lineshape method was not sufficient

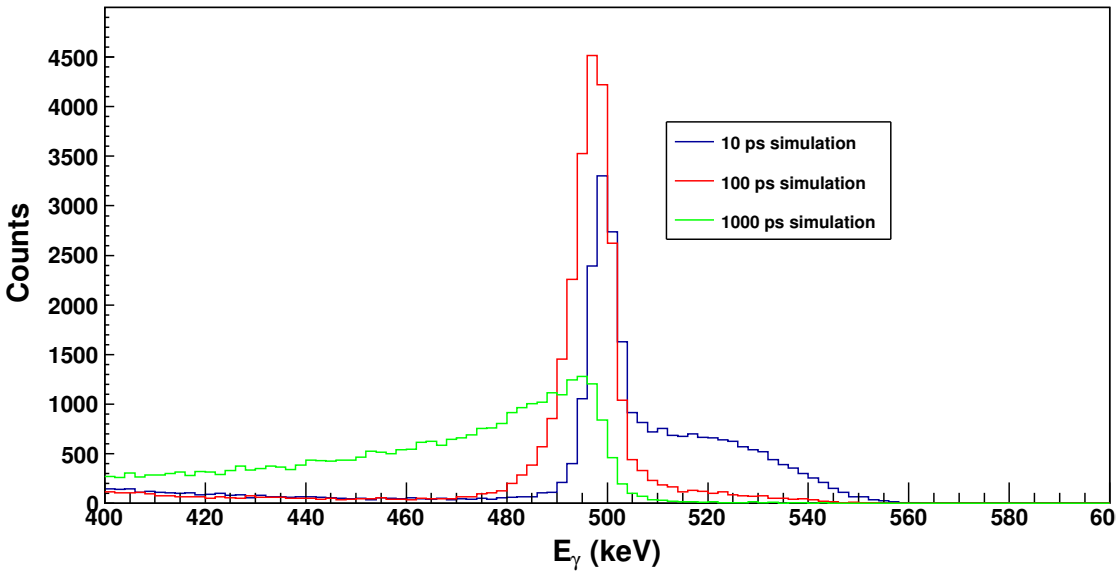

Figure 2.3: The change in the spectral lineshape of a 500 keV γ-ray transition for 10 ps, 100 ps, and 1000 ps lifetimes, shown in blue, red, and green, respectively. For the 10 ps lifetime, there is a significant high-energy shoulder which is smeared out over a large range, plus a sharp peak. This is due to some decays happening in the target where the velocity is faster than assumed having a smeared out Doppler correction and can be used as an indication of a short lifetime. The 100 ps lifetime shows only a peak, but it is shifted somewhat compared to the sharp portion of the 10 ps peak, and this shift is due to the lifetime. There is also a small low-energy tail. Finally, the 1000 ps lifetime peak has mostly a smeared out low-energy tail with only a small number of the decays happening near the target.

without some improvement. This is because ^{70}As is an odd-odd nucleus and has a very complicated level scheme. The presence of many photopeaks located close together in the γ-ray spectra made it difficult to be certain that the lineshape observed for a given state was, in fact, due to the lifetime and not to the presence of another peak at roughly the same place. In addition, when there are multiple decays happening sequentially, the lifetime of one state will have an effect on the measured lifetime of all of the states that it "feeds." If this "feeding lifetime" is long or at least comparable to the lifetime of a lower-lying state under study, then it can cause a lifetime to be measured which is too long. For this reason, in order to achieve a sufficiently clean spectrum and to control feeding, it was necessary to use the

lineshape method with γ-γ coincidence data. This enforces the requirement that a specific state is populated first before another state, and therefore the history of each observed γ-ray transition is known. It is then only necessary to know the lifetime of the state which is feeding the lower-lying state(s) in order to correct for this effect on the lifetime. In addition, the number of observed transitions in such a case is often substantially reduced and so understanding the spectrum is considerably simplified. However, the requirement that a γ ray be present in coincidence with another of a specific energy causes a large reduction in the γ-ray yields, possibly of an order of magnitude or more. Therefore, successfully implementing this technique is also challenging, as the signals from γ-ray transitions may be reduced to the point that they are difficult to identify above the background. Thus, care must be taken to optimize the selectivity of the coincidence requirements while still maintaining sufficient statistics to make a meaningful measurement.

2.3 The Differential Recoil Distance Method

As the name implies, the Differential Recoil Distance Method (DRDM) is a variant of the Recoil Distance Method (RDM) described earlier in this chapter. As will be discussed in Ch. 5, this technique was used to measure the 2_1^+ state lifetime of ^{74}Rb. Although the method was first proposed in 1989 [33], it was not possible to implement it previously due to difficulties with experimental resolution [25]. Therefore, the use of this method in this work constitutes the first successful implementation of the technique.

In order to show the value of the DRDM, it is convenient to first introduce a variant of the classic RDM known as the *Differential Decay Curve Method* (DDCM), also described in [33]. The motivation for the DRDM then arises naturally from the development of the

DDCM. Since it is related to the classic RDM, the DDCM begins with the same equation (c.f. Eq. 2.17):

$$\frac{dn_i(t)}{dt} = -\lambda_i n_i(t) + \sum_{h=i+1}^{N} \lambda_h n_h(t) b_{hi}. \tag{2.24}$$

However, rather than seeking an integral solution to the differential equations, the DDCM attempts an algebraic solution. By defining the quantities

$$\begin{aligned} R_i(t) &= \lambda_i \int_t^{\infty} n_i(t) dt \\ R_{ij} &= b_{ij} R_i, \end{aligned} \tag{2.25}$$

where b_{ij} is the branching fraction of the decay of state i to state j, Eq. 2.24 can be rewritten in the form

$$\frac{dR_{ij}(t)}{dt} = -\lambda_i \left(R_{ij}(t) - b_{ij} \sum_h R_{hi}(t) \right). \tag{2.26}$$

The quantity R_{ij} is the *decay function* of the level i as it decays to the level j, and is given by the number of states that decay after the nucleus has been in flight for a time t. Equation 2.26 requires that this function as well as its derivative be known. This is accomplished by taking data at many different flight times (that is, many different distances between the target and degrader/stopper foils). If the time t is defined as the time it takes for a nucleus to travel between the two plunger foils, then the number of states that decay after this time will just be the number of observed γ rays in the peak corresponding to the degrader/stopper. The function R_{ij} can then be determined by fitting an appropriate analytical function to the set of values of R_{ij} measured at different distances, and the derivative of the function taken to determine dR_{ij}/dt. If higher states h are present that feed the level i, then the number of γ decays observed in the degrader/stopper peaks (the second term in the numerator of

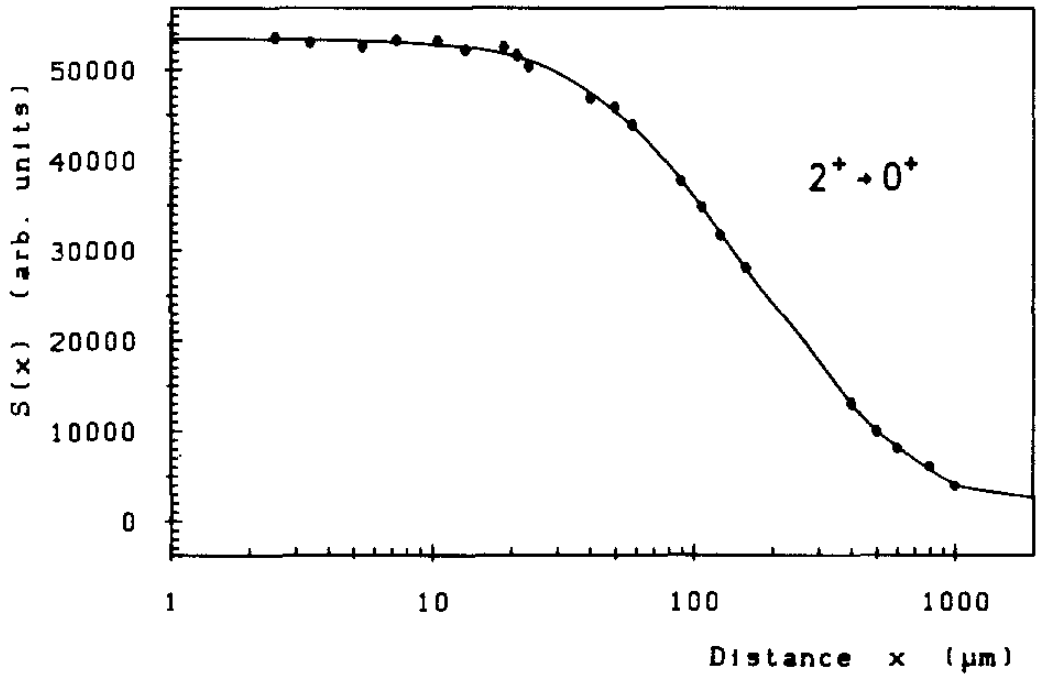

Figure 2.4: An example decay curve measured for the $2_1^+ \rightarrow 0_1^+$ transition in ^{120}Xe with the DDCM. The function S_{ij} plotted on the vertical axis is proportional to R_{ij}. As can be seen, many data points are used to determine the lifetime, which in turn requires a large amount of data to be taken. Figure is taken from [33].

Eq. 2.26) are subtracted from the decays associated with the level i in order to remove the perturbing influence of the feeding on the lifetime. Compared to the Eq. 2.18 for the RDM, which can quickly become very complicated when multiple feeding levels are involved, the lifetime analysis in the DDCM is considerably more transparent, as only a few parameters need to be determined. This facilitates accurate determination of the lifetime and reduces the reliance on very complicated fitting routines.

However, despite the advantages of the DDCM, a rather large drawback of the technique is its requirement that many data points be obtained and fit in order to determine the decay function R_{ij}, as illustrated in Fig. 2.4. For those nuclei which can be produced easily this does not pose a challenge, but for very exotic nuclei this can be a serious problem, as the amount of beam time necessary to accurately determine the derivative of the function R_{ij}

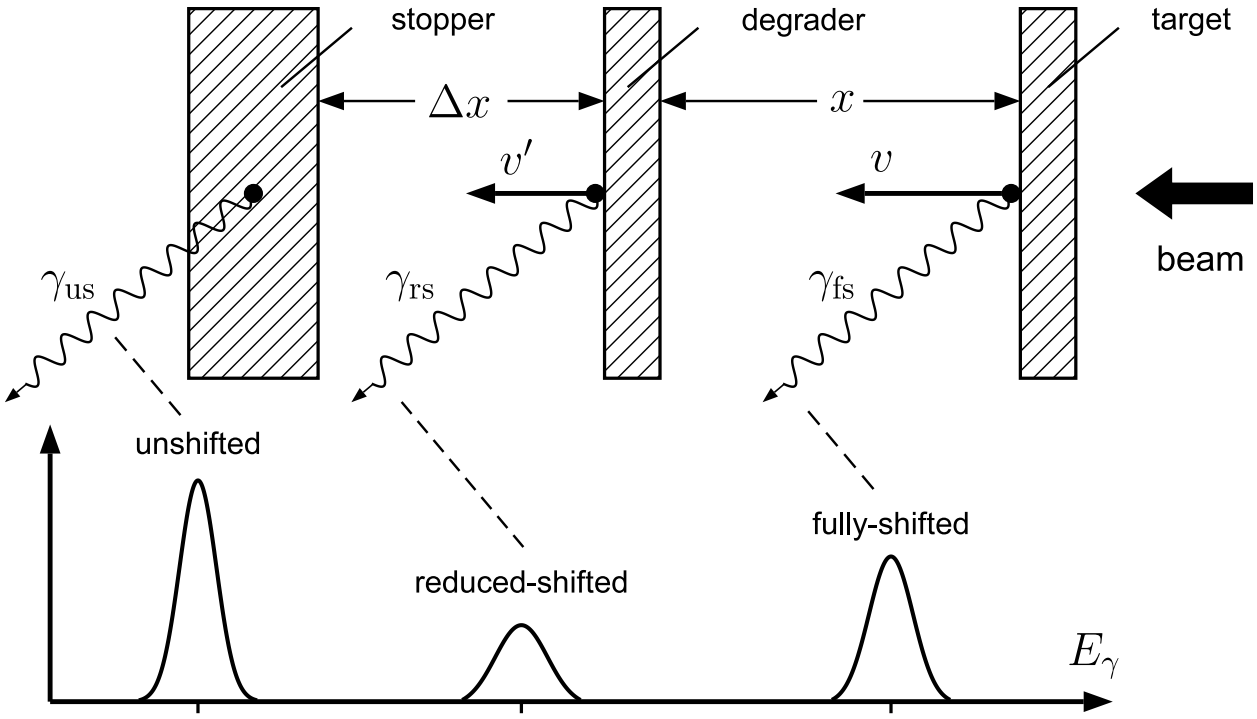

Figure 2.5: A schematic drawing of a differential plunger used for the DRDM. The beam enters from the right and excited states are created by interaction with the target. The recoiling nuclei exit the target with velocity v and travel a distance x before being slowed in the degrader. After the degrader they travel a short distance Δx at a reduced velocity v' before being stopped in the stopper. As the excited nuclei relax, they emit γ rays with different Doppler shifts at velocities v, v', and at rest, producing the γ-ray spectrum shown at the bottom. Figure is from [25].

may become prohibitively large. This is where the DRDM method comes into play. Instead of determining the derivative of the function R_{ij} by fitting many data points, the DRDM instead extracts the derivative of the decay function directly from the data. In order to do this, a modification of the plunger is necessary. As shown in Fig. 2.5, a third foil is added to the classic plunger design between the target and the degrader/stopper so that the photopeak from the decay of each state is divided into three Doppler-shifted components. This foil is always a degrader, as it is necessary that the nucleus being studied reach the third foil. With this change, it becomes possible to determine the lifetime of a state with a measurement at only one distance setting, thereby extending the family of Recoil Distance

measurements to much more exotic nuclei.

In order to see how a measurement with only one distance setting can yield the lifetime of a nuclear state, it is useful to return to Eq. 2.26 and begin rewriting it in terms of the quantities shown in Fig. 2.5. For the purposes of this discussion, it will be assumed that the last foil in the experiment is a stopper for consistency with Fig. 2.5. As in the DDCM, the decay function R_{ij} is given by the number of excited nuclei that remain after a given time t. It is convenient to take this time to be the time at which the decaying nucleus reaches the stopper foil (denoted t_s), since the number of decays observed in the unshifted peak from the stopper foil directly correspond to the number of excited states remaining at t_s and therefore to $R_{ij}(t_s)$. This number of decays will be denoted I^s_{ij}. Similarly for any feeding states, $R_{hi}(t_s)$ will be written I^s_{hi}. Now, to determine the derivative of R_{ij}, it is necessary to make an approximation. If the flight time of the nucleus is short compared to the lifetime of the state under study, then the derivative of the decay function for the state i can be found by a difference approximation of the decay function as the nucleus passes the degrader at the time t_d and as it encounters the stopper at time t_s:

$$\frac{dR_{ij}(t_s)}{dt} \approx \frac{R_{ij}(t_d) - R_{ij}(t_s)}{t_s - t_d}. \tag{2.27}$$

By noting that $t_s - t_d = \Delta t = \Delta x/v'$ in the nomenclature of Fig.2.5 and that $R^d_{ij} = I^d_{ij} + I^s_{ij}$, Eq. 2.27 can be written as

$$\frac{dR_{ij}(t_s)}{dt} \approx \frac{R_{ij}(t_d) - R_{ij}(t_s)}{t_s - t_d} = \frac{(I^d_{ij} + I^s_{ij}) - I^s_{ij}}{\Delta x/v'} = I^d_{ij}\frac{v'}{\Delta x}. \tag{2.28}$$

Plugging this into Eq. 2.26 finally gives

$$\tau = -\frac{\Delta x}{v'} \frac{I^s_{ij} - b_{ij} \sum_h I^s_{hi}}{I^d_{ij}}, \tag{2.29}$$

which is the expression for the lifetime in the DRDM.

It is worth discussing the details of the DRDM further in order to make clear the advantages of the method. As stated, the addition of a third foil makes it possible to extract lifetimes from experimentally measured quantities with only one distance setting between the foils, which is a considerable improvement over the DDCM. This allows measurements to be made of nuclei which are very difficult to produce, as significantly fewer counts are necessary to determine the lifetime. Of course, feeding is a concern, and while the expression for the lifetime in the DRDM does explicitly treat feeding contributions, the effects of feeding also warrant comment. For a feeding lifetime similar to that of the state being studied, a significant fraction of the decays observed for the level of interest will be created a significant distance from the target, and the term subtracted in the numerator of Eq. 2.29 will be very important. On the other hand, if the feeding states have a lifetime which is much shorter than that of the state being studied, the design of the DRDM is such that it automatically minimizes the effects of feeding. This is because the target is removed some distance from the degrader, and therefore a state which is short-lived compared to the transit time to the degrader will have almost entirely decayed before reaching it. Therefore, the DRDM effectively isolates the state being studied from the effects of feeding so long as the target-degrader distance is properly chosen. This is reflected in the fact that the expression for the lifetime in the DRDM does not make reference to the number of decays detected after the target (i.e. I^t_{ij}). Of course, the ideal case is when there is no feeding at all, and

then the expression for the lifetime becomes especially transparent:

$$\tau = -\frac{\Delta x}{v'} \frac{I_{ij}^s}{I_{ij}^d}. \tag{2.30}$$

As will be seen in Ch. 5, this expression can be very powerful for quickly obtaining an estimate of the lifetime of a state before performing a full analysis, as only four quantities are necessary to calculate the lifetime.

Chapter 3

Experimental Methods

The nature of rare isotopes is that they exist only for a short time before decaying towards more stable species, mainly through β decay. Therefore, in order to study these rare isotopes, it is necessary to produce them in a laboratory setting before transporting them to an experimental area for investigation. Doing so successfully often requires the use of sophisticated techniques and the simultaneous operation of multiple state-of-the-art devices. This chapter presents the process of developing and delivering a beam of rare isotopes at the National Superconducting Cyclotron Laboratory (NSCL), as well as the experimental equipment and methods relevant to the analyses presented in this work.

3.1 Beam production

The NSCL uses the projectile fragmentation method to produce exotic nuclei. In this method, a beam of stable nuclei is first produced by ionizing them in an *ion source* and then accelerating them to relativistic speeds in the *K500* and *K1200 cyclotrons*, together known as the *Coupled Cyclotron Facility* (CCF) [34, 35]. This beam of stable nuclei is called the *primary beam*, as it is the first and most intense beam of nuclei created by the facility. Once it is produced, the primary beam is then directed onto a piece of material, usually beryllium, which is known as the *primary target* or *production target*. As the primary beam passes through the primary target, nuclear reactions may be induced which can produce

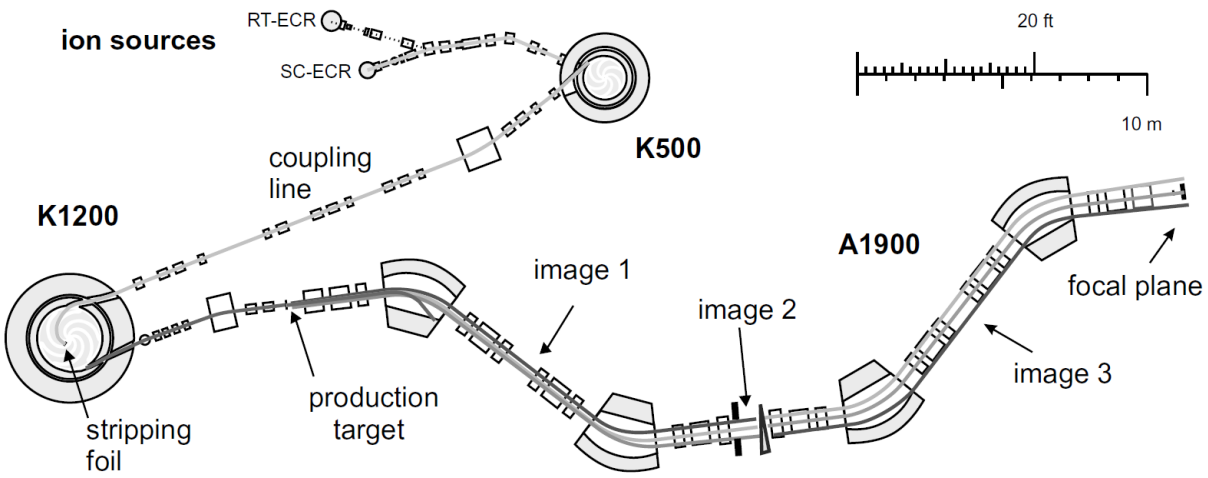

Figure 3.1: An illustration of the equipment used to create a beam of rare isotopes at the NSCL. A beam of ions with a only a few electrons removed is generated in one of the ion sources, then injected into the K500 cyclotron. After being accelerated, the beam is transported to the K1200, where it is further stripped of most or all of its electrons and accelerated again. The beam is reacted on the production target and a single species is selected to study in the A1900 before being transported to an experimental endstation. Figure is from [36].

many different species of nucleus. These species typically contain fewer nucleons than the primary beam, giving rise to the name "fragmentation." Once past the primary target, one or a few of the species produced can be selected in the *A1900 Fragment Separator* [36] based on their charge and momentum in order to create the *secondary beam*, which then can be transported to one of the experimental areas for further processing or analysis. Figure 3.1 shows the arrangement of the equipment just mentioned, and details of this process are presented in the following subsections.

3.1.1 Primary beam production

The creation of a beam of rare isotopes at the NSCL begins with the production of ionized stable nuclei. There are two ion sources available to accomplish this task: the Superconducting Source for Ions (SuSI) [37, 38] and the Advanced Room TEMperature Ion Source

(ARTEMIS) (see Ref. [39] for a description of ARTEMIS-B, an identical copy of the ion source used for primary beam production), both of which operate on the principle of electron cyclotron resonance. If the stable species that will be accelerated is gaseous, then it may be used directly in the ion sources. However, if it is metallic, then the material must be placed into an oven to produce a vapor that the ion sources can use. With the atoms now prepared in a gaseous state, *electron cyclotron resonance heating* [40] is used to ionize them. The atoms to be accelerated are injected into a plasma confined within a magnetic field while they are being ionized by microwave radiation applied at the electron cyclotron resonance frequency ω_c, given by

$$\omega_c = \frac{eB}{m_e}, \tag{3.1}$$

where e is the charge of the electron, B is the magnetic field strength, and m_e is the mass of the electron. This causes energy to be transferred to the electrons of the plasma, accelerating them. Multiple ionization is achieved by the accelerated electrons repeatedly impacting the species to be used to form the primary beam, ionizing the beam material step-by-step to the desired charge state before it is extracted from the ion source by an applied electric field gradient. For both of the experiments described in this work, SuSI was used to produce ^{78}Kr ions with a charge state of 14+. For more details on electron cyclotron resonance ion sources, see Ref. [40].

After extraction from the ion source, the two cyclotrons of the Coupled Cyclotron Facility [34, 35] are used to accelerate the ions up to the desired beam energy. The operating principle of the cyclotrons is based upon the application of a radio-frequency electric field for acceleration and a magnetic field for confinement of the ions. The electric field is produced by three pairs of blade-shaped electrodes known as "dees," to which a rapidly switched elec-

tric potential is applied. When the ions are injected into the cyclotrons, they experience an acceleration whenever they pass through the space between each pair of dees. Meanwhile, a magnetic field is applied transverse to the plane in which the dees lie. Because the ions are in motion, the magnetic field causes them to experience a Lorentz force that produces a circular trajectory in the cyclotrons. The radius ρ of this trajectory for a given velocity can be found by equating the Lorentz force due to the magnetic field with the centripetal force experienced by the ions in the non-relativistic limit:

$$qvB = \frac{mv^2}{\rho}, \tag{3.2}$$

where q, m, and v, are the charge, mass, and velocity magnitude of the ions, respectively, and B is the magnitude of the applied magnetic field. In the absence of the accelerating electric field, the radius of the circular orbit in the cyclotrons is then

$$\rho = \frac{mv}{qB}. \tag{3.3}$$

However, the acceleration from the electric field continually increases the velocity of the ions, causing them to spiral outward towards the edge of the cyclotrons where they are extracted. For a particular cyclotron with a given radius and magnetic field, the energy of the ions at extraction is determined by their charge and mass and can be found by rearranging Eq. 3.3 for the velocity at the maximum radius:

$$E = \frac{1}{2}mv^2 = \frac{1}{2}m\left(\frac{qB\rho}{m}\right)^2 = \frac{q^2B^2}{2m\rho^2} \propto \frac{q^2}{m}. \tag{3.4}$$

At the Coupled Cyclotron Facility, the NSCL operates two cyclotrons connected in series:

the K500 cyclotron and the K1200 cyclotron (see Ref. [41] for several schematic drawings and photographs of the K500). The names correspond to the so-called "K-number" of the devices, which corresponds to the maximum energy to which a beam of protons can be accelerated, although in practice this is not typically done. In principle, however, the K500 can produce a beam of 500 MeV protons, while the K1200 can produce a beam of 1200 MeV protons. Both cyclotrons are isochronous, such that the RF frequency of their accelerating electric fields is constant at about 23 MHz. As a consequence, in order to compensate for the relativistic effects of the ions accelerating in these fields, the magnetic fields increase in strength from the center of the cyclotrons towards their outer radii. In order to accelerate ions most efficiently, the cyclotrons are coupled to produce higher energy beams. According to Eq. 3.4, the highest energy beams for a given species can be produced when the charge of that species is maximized. However, in order to produce ions which have the maximum number of electrons removed, a significant penalty in beam current must be incurred. To compensate for this, partially stripped ions are extracted from the ions sources, which have a much higher beam rate, and injected into the K500. These ions are accelerated to their maximum velocity of about $0.15c$ in the K500 before being extracted and then directed through a thin carbon *stripper foil* whose purpose is to remove the remaining electrons from the ion species. The now fully- (or mostly-) stripped ions are then injected into the K1200 where they are accelerated up to their final velocity of about $0.5c$. For the works described in this dissertation, the K500 produced beams of ^{78}Kr ($Z = 36$) with an energy of 13.02 MeV/nucleon and a charge state of 14+ which were subsequently sent to the K1200 to produce primary beams of ^{78}Kr with an energy 150 MeV/nucleon and a charge state of 34+.

3.1.2 Secondary beam selection

Although some experiments at the NSCL are performed using stable beams, the majority of experiments make use of radioactive species to perform experiments. To produce these radioisotopes, the technique of *projectile fragmentation* [42, 43] is used to produce the nucleus to be used in the experiment. For this technique, the primary beam is impinged upon a piece of material called the *primary production target* or simply the *primary target*. Beryllium is usually chosen to be the target material because it has a high number density of target atoms, a high melting point, and good thermal conductivity so that it can withstand and release the significant heat deposition from the primary beam. Most of the primary beam particles will pass through the primary target without interaction, but some fraction will undergo a nuclear reaction which can produce many different species lighter than (or, in the case of a charge exchange reaction like in Ch. 4, of an equal weight to) the primary beam. At this point, it is necessary to select the desired isotope from all other isotopes produced by the interaction of the primary beam with the primary target, as well as any beam particles which did not react.

In order to select the desired nuclear species from all other species present in the now-composite beam, the A1900 Fragment Separator [36] is used. The A1900 is composed of four superconducting 45° dipole bending magnets and 24 superconducting quadrupole focusing magnets which are collectively used to eliminate unwanted reaction products as well as unreacted primary beam particles from the beamline. Each dipole magnet is separated by two triplets of quadrupole magnets, and between each pair of quadrupole triplets is an image plane where a pair of slits with variable width is located. A wedge of material can be inserted at the momentum dispersive focal plane (Image 2 in Fig. 3.1) position which serves to aid

in isotope separation [44], and finally a suite of detectors is located at the achromatic focal plane at the end of the separator (the *focal plane detectors*, Image 3 in Fig. 3.1) which provide information about the now purified secondary beam.

The A1900 achieves isotopic separation by taking advantage of the fact that each species present in the beam will have a specific (although not necessarily unique) *magnetic rigidity*, given by

$$B\rho = \frac{mv}{q} \propto \frac{A}{Z}v, \tag{3.5}$$

where B and ρ are the magnetic field strength and radius of curvature of the dipole magnet through which a particle is traveling, and m, v, and q are the mass, velocity, and charge of the particle as defined in Eq. 3.3. This quantity (which is often simply called the "$B\rho$") has the advantage that it identifies the ratio $\frac{A}{Z}$ of a given particle, independent of the device used to produce the magnetic field. The velocity v is typically almost constant for species produced in fragmentation, and so the velocity dependence of the $B\rho$ does not interfere with identifying nuclei. The first step in purifying the beam in the A1900 is to select in the dipole magnets a specific $B\rho$ which includes the isotope to be studied. Those nuclei which do not match this $B\rho$ will follow a path with a radius of curvature different than that of the magnets and will fail to be accepted into the next section of the beamline. Because the beam is now spread out in the dispersive direction (i.e. the direction in which the beam bends), further selection is provided by the pairs of slits at the intermediate image locations. These slits are positioned such that they block all but a narrow portion of the beam which selectively contains the isotopes to be studied.

The separation of the beam based on the magnetic rigidity may still allow multiple species with the same A/Z ratio as the desired nucleus to pass through the separator. In order to

remove such persistent contaminants from the beam, an aluminum "wedge" is inserted into the beamline at the Image 2 location. This wedge (which actually may be a curved piece of aluminum of uniform thickness if it is thin enough) results in the different components of the beam experiencing a different effective thickness as they pass through the wedge. The various components of the beam will experience a unique energy loss which is governed mainly by their charge q and velocity v and is given according to the Bethe formula [45]:

$$-\frac{dE}{dx} = \frac{4\pi e^4 q^2}{m_e v^2} NZ \left[\ln \frac{2m_e v^2}{I(1-\beta^2)} - \beta^2 \right]. \tag{3.6}$$

In this expression, N is the number density and Z the atomic number of the atoms in the wedge, e is the unit of electric charge, I is a parameter specific to the stopping material (the aluminum wedge in this case), and β is the beam velocity expressed as a fraction of the speed of light c. This energy loss causes the different parts of the beam, which were degenerate in $B\rho$, to now have a different magnetic rigidity. The desired isotope can then be selected in the second half of the A1900 by a similar $B\rho$ separation as in the first half, providing a beam which is largely free of contaminants. This beam is then sent to the focal plane of the A1900 where various detectors may be used for beam diagnostics and identification purposes. The most important of these for the purposes of this work is the extended focal plane (xfp) scintillator which, together with the object scintillator in the S800 (see Sec. 3.2.1), is used for identifying the components of the beam in the experiment.

3.2 Experimental devices and detector systems

The previous section describes the radioactive ion beam production process that is common to most experiments done at the NSCL. However, a wide array of other devices are available at the laboratory. Depending on the physics goals of a given experiment, the secondary beam may be sent to one of several different vaults that are dedicated to certain setups. For the purposes of the experiments described in this work, it was necessary to select an area where the products of secondary reactions induced in the beam could be detected along with γ radiation being emitted by these reaction products. Therefore, in both experiments presented in this work the secondary beam was transported to the S3 vault, where the S800 spectrograph is located and can be coupled with γ-ray detection systems. This section will discuss the experimental apparatus and detector systems used in these experiments, including S800 and the two different γ-ray detector arrays used, as well as the TRIPLEX plunger device, which was critical to the success of the lifetime measurement of ^{74}Rb.

3.2.1 The S800 Spectrograph

For in-beam experiments performed at the NSCL, further manipulation of the secondary beam may be necessary in order to extract the desired physics. This may be the case, for instance, for reaction studies in which it is necessary to measure the angular distribution of reaction products or for experiments which are intended to study nuclear states created in the reacted beam at the experimental station. In such cases where further reactions of the secondary beam are necessary, the ability to again identify one reaction product from the potentially many newly created species is necessary. For this purpose, the S800 spectrograph [46], shown in Fig. 3.2, may be used.

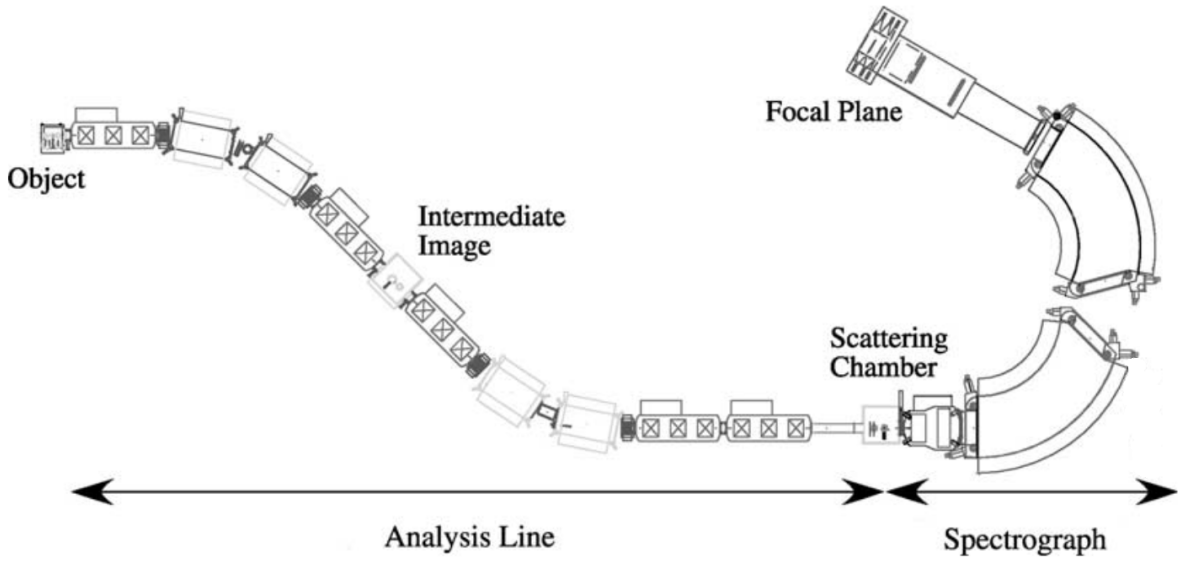

Figure 3.2: A diagram showing the layout of the S800 spectrograph. The beam enters at the Object position and is bent down through an analyzing beamline towards the location labeled scattering chamber, where experimental apparatus and target materials are typically located. After passing this location, the beam is bent upward through the two dipoles of the spectrograph and beam particles are identified in a suite of detectors located inside the focal plane. Figure adapted from [46].

The S800 is composed of an analyzing beamline and the spectrograph itself. The beamline is built of superconducting magnets which are used to direct and focus the beam, while the spectrograph is comprised of two superconducting dipole bending magnets plus a suite of particle detectors located just past these dipoles in the final focal plane [47]. The S800 can be operated in two modes: focused mode and dispersion matching mode. In focused mode, the beamline is achromatic such that the beam is focused at the target position but dispersed in the focal plane. This mode allows for the widest momentum acceptance of roughly $\pm 2.5\%$, but the momentum resolution is then limited by the momentum spread of the incoming beam. By contrast, in dispersion matching mode the entirety of the S800 is tuned to be achromatic so that the beam is dispersed across the target but this dispersion is canceled in the focal plane. For typical targets, the momentum acceptance is limited to $\pm 0.25\%$ in

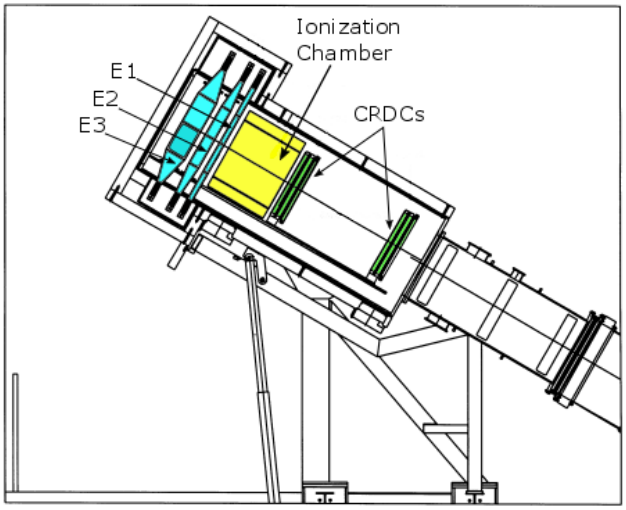

Figure 3.3: An illustration of the detectors located in the focal plane of the S800 spectrograph. The beam first passes through the two CRDCs which provide position and angle information. Next the beam passes through the ionization chamber which measures the energy loss of the beam as it passes through the detector. Next the beam passes through the E1 scintillator, which serves as both a timing signal and a trigger. In the figure there are two more plastic scintillators, but these have been replaced with a 32 crystal CsI(Na) hodoscope for charge state identification [49]. Figure is taken and modified from [47].

this mode [48], but greater precision in the momentum measurement of the beam can be achieved. Both of the experiments described in this work were run in focused mode.

3.2.1.1 S800 particle detection systems

The S800 makes use of a variety of particle detectors for the purposes of beam diagnostics and identification. The majority of these are housed in the focal plane, shown in Fig. 3.3, and include two Cathode Readout Drift Chambers (CRDCs) for position and angle determination, an Ionization Chamber (IC) which measures energy loss, a plastic scintillator (called the E1 scintillator) for timing and triggering information, and a hodoscope composed of 32 CsI(Na) crystals for charge state identification. Besides the focal plane detectors, there is also a scintillator at the object position (known as the OBJ scintillator) which together with the E1 scintillator gives the time of flight for the ions through the entire spectrograph.

Optionally, tracking detectors may be inserted at the intermediate object image of the spectrograph beamline to characterize the path of the beam before it interacts with the target. However, these detectors were not used in the experiments described in this work, and so will not be discussed further here.

3.2.1.1.1 Time of Flight Scintillators Thin plastic scintillators in the S800 serve to identify the time of flight of the particles through the spectrograph. When beam particles pass through these scintillators, light is emitted and collected in the photomultiplier tubes attached to the ends of the scintillators. While they have poor energy resolution, the light pulse that they emit has a very fast decay time, resulting in excellent time resolution (with a FWHM of the timing signal on the order of 100 ps [47]) ideal for time of flight measurements. The two scintillators used in the S800 are the E1 scintillator in the focal plane, and another scintillator located at the object position of the spectrograph. In the focal plane, the E1 scintillator is located just before the hodoscope and is used as a trigger signal for the S800 readout as well as providing a timing signal. When this timing signal is combined with that from the scintillator at the object position, the time of flight of a particle through the spectrograph can be calculated.

3.2.1.1.2 The Ionization Chamber The ionization chamber is located in the S800 focal plane just after the CRDCs. As with the CRDCs, the ionization chamber has an active area of roughly 30 cm by 60 cm, but has a depth of 16 inches. The volume of the detector is filled with P10 gas (a mixture of 90% argon and 10% methane) and is divided into 16 1-inch sections along the beam direction. Previously this segmentation was achieved by having 16 separate anodes paired with a cathode on the opposite side of the detector. However, this design was replaced with a new detector in which there are 16 cathode-anode pairs

formed from aluminized mylar foils. As beam particles pass through the detector, energy is deposited in the gas and a number of electron-ion pairs are created proportional to the energy deposited. The electrons are collected on the anodes and the ions on the cathodes. The charge collected in this way is determined by the number of pairs created and is therefore proportional to the energy loss of the particle. Since the energy loss is in turn proportional to the square of the charge of the particle as given by Eq. 3.6, this gives identification of the element of the particle in the focal plane.

3.2.1.1.3 Cathode Readout Drift Chambers The CRDCs measure the position and the angle of the beam as it traverses the focal plane of the S800. These detectors have an active area of roughly 30 by 60 cm and a depth of 1.5 cm, and are separated by 1 m. The CRDCs are filled with a gas mixture which is 80% CF_4 and 20% C_4H_{10}, and when a beam particle passes through this gas mixture electrons are dislodged from the gas and are collected on an anode wire. The position in the dispersive direction (the x position) is determined by measuring the induced signal on the neighboring cathodes which sandwich the anode and are divided into 224 pads. The distribution of induced charges on the pads is fit with a Gaussian function to determine the x-position. The y-position is determined by the drift time of the electrons in the gas, where the time is measured between the collection of the charge on the anode wire and the timing signal from the E1 scintillator. The first CRDC is located at the optical focus of the S800 and so the dispersive and non-dispersive coordinates of a beam particle in the focal plane (called x_{fp} and y_{fp}, respectively) are taken from this detector. The angles in the dispersive and non-dispersive directions relative to a central trajectory through the S800 focal plane (termed a_{fp} and b_{fp}, respectively) at which a particle travels is determined by the difference in the positions measured in each of the

CRDCs.

3.2.1.1.4 Trajectory Reconstruction While the detectors of the S800 provide the ability to determine the position and momentum of beam particles in the focal plane, it is often of greater interest to know the beam properties at the location of the target. For this purpose, the S800 provides the capability to reconstruct the trajectory of the beam at the target position on an event-by-event basis. This was critical for both of the experiments described in this work, as both relied heavily on reproducing the experimental measurements with simulations (see section 3.3 for more details). The simulations rely on the ability to accurately reproduce the properties of the beam as it exits the target, and so the particle tracking facility of the S800 is very important to these analyses.

The trajectory reconstruction is achieved by way of an analytical calculation in the code COSY INFINITY [50]. Using the measured magnetic field maps of the magnets, this program constructs a transfer map $\mathbf{S}$ which transforms the beam parameters at the target to those at the focal plane. In practice, since the focal plane parameters are the ones measured, the inverse transfer map $\mathbf{S}^{-1}$ is then calculated and used to determine the desired parameters at the target location:

$$\begin{pmatrix} a_{ta} \\ y_{ta} \\ b_{ta} \\ d_{ta} \end{pmatrix} = \mathbf{S}^{-1} \begin{pmatrix} x_{fp} \\ a_{fp} \\ y_{fp} \\ b_{fp} \end{pmatrix}. \tag{3.7}$$

Here the parameters with the subscript ta indicate beam parameters at the target while fp indicates parameters at the focal plane. In either case, x and y indicate dispersive and non-dispersive position, while a and b indicate angles in the dispersive and non-dispersive

directions, respectively. The parameter d_{ta} indicates the energy of the beam at the target. For this transformation, the spread of the beam in the dispersive direction is assumed to be negligible and so x_{ta} is set to zero, thereby allowing the energy d_{ta} to be calculated [46].

3.2.1.2 Detector calibrations

The detectors in the S800 must be properly calibrated to be of use in an experiment. As these detectors were common to both of the experiments in this work, the calibration procedures will be described here so that they do not need to be repeated in the chapters devoted to the individual studies.

3.2.1.2.1 CRDC calibrations The CRDCs determine the (x, y) position of the beam as it passes through these detectors, and this position needs to be calibrated so that any offsets are removed. This is done during the experiment by inserting a thick metal plate (called a "mask") with a specific pattern of holes and slits drilled in it in front of each CRDC. The beam is then swept across the face of the detector with the mask in front of it, with the consequence that only the parts of the detector behind the holes in the mask are illuminated. Figure 3.4 shows the signals measured in the CRDCs when the masks are inserted. Since the locations of the holes are well-determined on the masks, the signals recorded in the CRDC during a mask run correspond to known physical positions. The positions recorded in the CRDC are then linearly scaled so that the pattern that is recorded matches the physical dimensions of the pattern of holes on the mask. Several mask runs are taken throughout an experiment, since the positions that are recorded in the CRDCs are dependent upon experimental conditions such as the pressure of the fill gas and the temperature. If there is any change in the calibration between mask runs, this can be

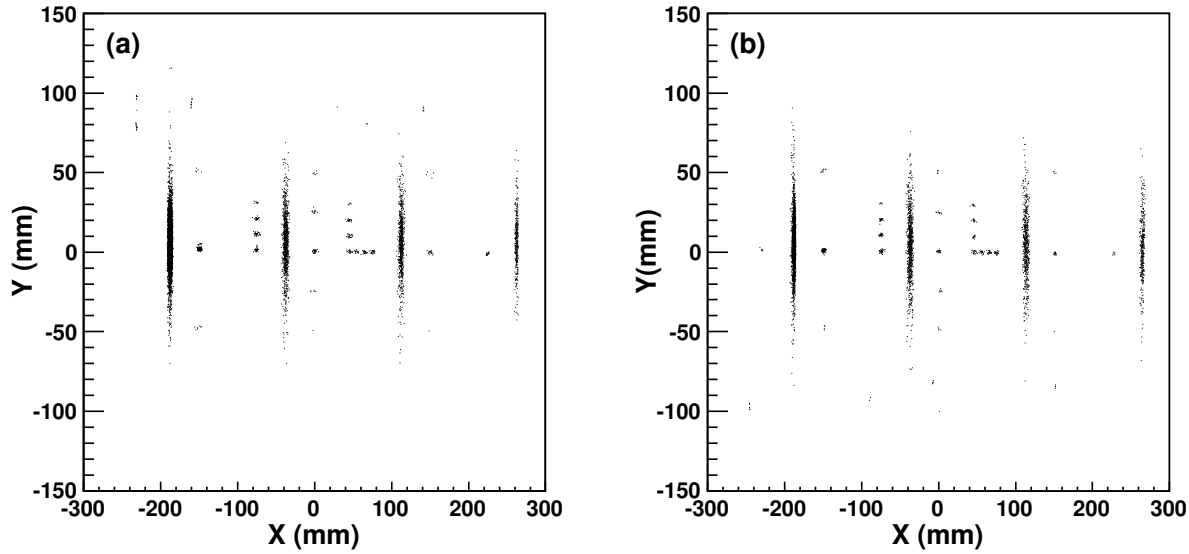

Figure 3.4: The measured signals in the CRDCs when the masks are inserted into the beamline. The first CRDC is shown on the left, and the second on the right. By matching the pattern of slits and holes on the mask to the pattern of signals generated in the CRDCs, the CRDC positions can be calibrated.

taken into account by interpolating between the mask runs to correct for any changes in the experimental conditions.

3.2.1.2.2 Ionization chamber calibration The ionization chamber has sixteen channels which are used to measure the energy loss of the beam as it passes through the detector. Since the energy loss for the detector is determined by averaging the energy loss in each channel, the channels need to be gain matched so that no single channel has a greater influence than the others. This is done by selecting at least two nuclear species and measuring their energy loss as recorded in each channel. The energy loss peaks are then fit with Gaussians, and the centroids are used to create a linear function that scales each channel to match that of the channel which has the smallest unadjusted energy loss. Figure 3.5 shows the result of this gain matching.

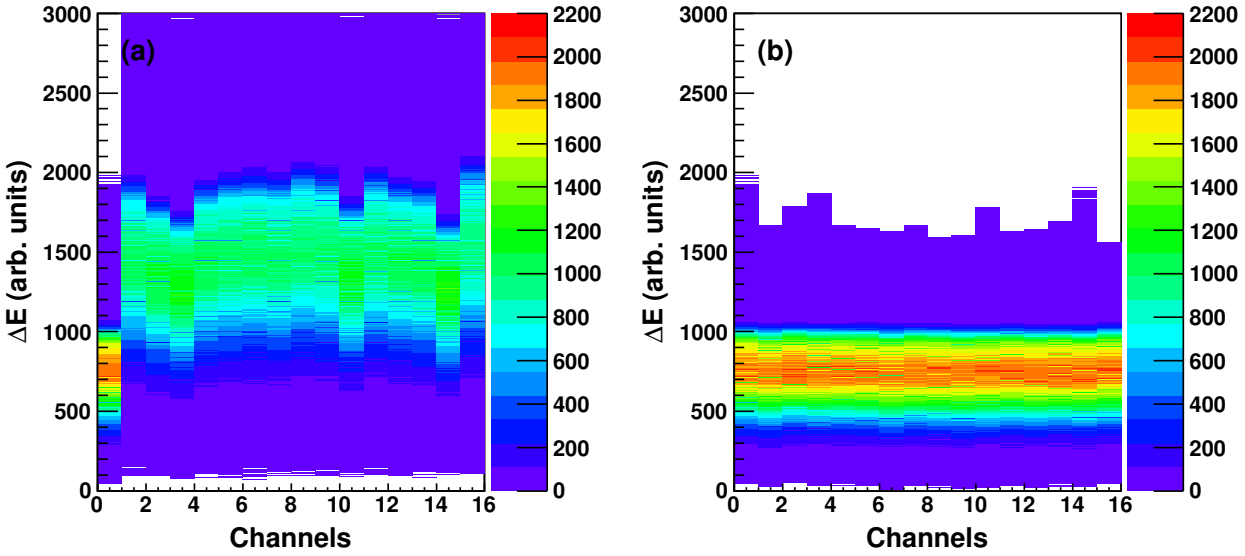

Figure 3.5: This figure shows the gain matching of the ionization chamber. On the left, the raw energy loss signals (in arbitrary units) are shown for each channel. On the right, the energy loss in each channel has been gain matched to channel zero, which has the lowest raw energy loss signal. As a result, the centroids of the energy loss in each channel are the same, and this provides much cleaner elemental separation when performing particle identification.

3.2.1.2.3 Time of flight corrections Due to the different paths that ions take through the spectrograph, there is a correlation between the time of flight measured by the scintillators and the measured angle of the ion trajectories as they pass through the CRDCs. Removing this correlation allows for better identification of nuclear species in the S800 focal plane. The form of this correction is

$$T_{scint,corrected} = T_{scint} + ma_{fp} + nx_{fp}, \tag{3.8}$$

where a_{fp} and x_{fp} are the dispersive angle and position in the focal plane, respectively, and m and n are constants to be determined. Figure 3.6 shows the effect of this correction for the extended focal plane and object scintillators, as well as for the RF signal from the cyclotrons.

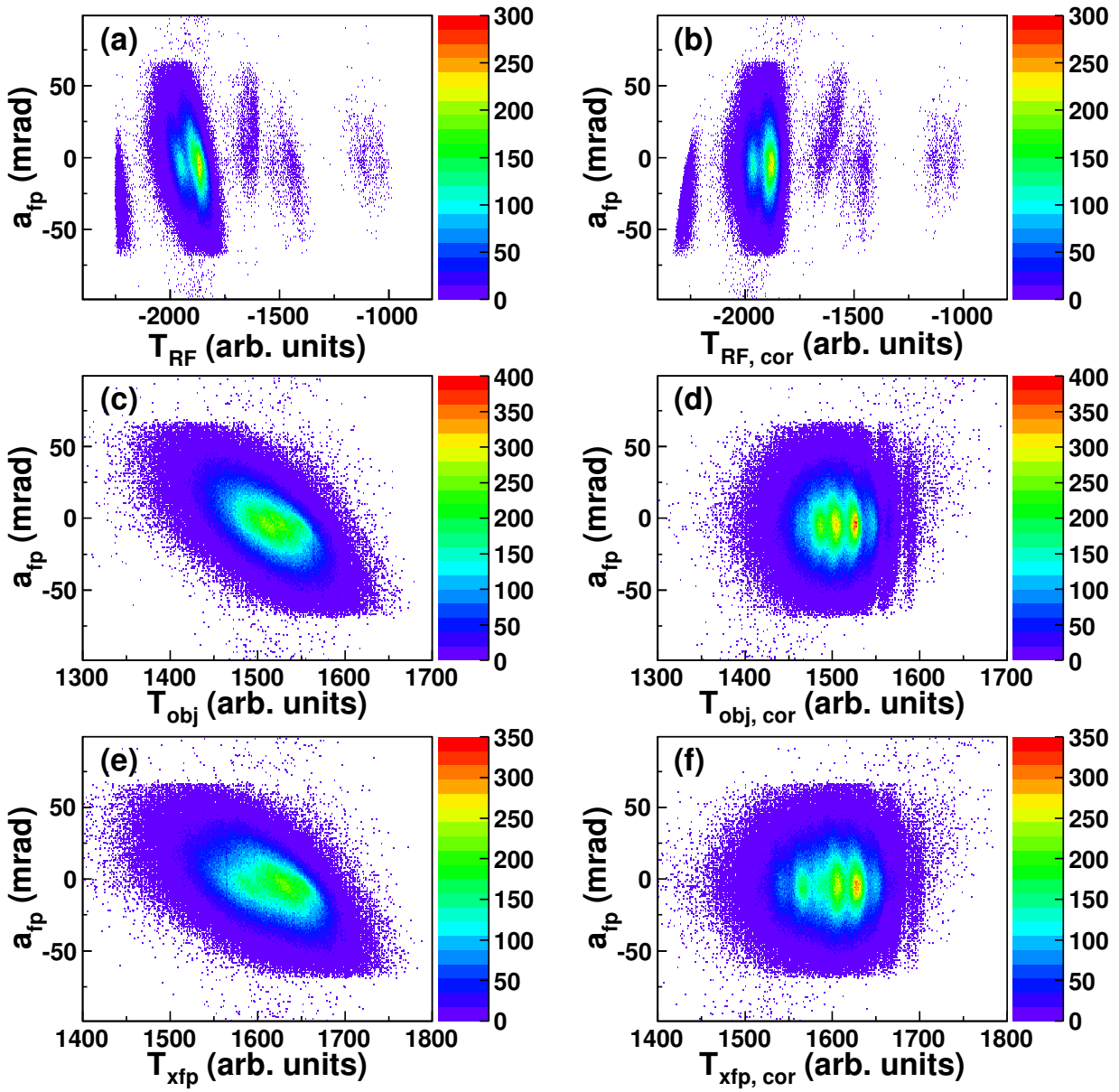

Figure 3.6: The effect of correcting the time of flight measured for the RF signal (top row), object scintillator (middle row), and extended focal plane scintillator (bottom row). Uncorrected spectra are shown on the left, corrected spectra on the right.

3.2.2 γ-ray detectors

Both of the techniques for extracting lifetimes utilized in the experiments described in this work are predicated on the detection of γ rays. The techniques themselves have already been described in detail in Ch. 2, however, neither the actual process of detecting γ rays nor the apparatus used to detect them has been discussed. This section and its subsections therefore summarize the important aspects of the measurement of γ radiation as well as the two different γ detector arrays used in each of the two analyses contained herein.

3.2.2.1 γ-ray interactions with matter

Unlike charged particles, which undergo a continuous process of slowing down in a material, γ rays interact with matter in discrete steps. For the purposes of this work, this interaction can be described by three processes which dominate at different energies: *photoelectric absorption*, *Compton scattering*, and *pair production*. While each of these processes is distinct from the others, they are similar in that each involves the transfer of energy from the photon to electrons present in the material. The remainder of this subsection will describe these processes.

Photoelectric absorption occurs when a photon interacts with and transfers all of its energy to an atomic nucleus, as illustrated in Fig. 3.7. This results in the ejection of one of the atomic electrons as a photoelectron with a kinetic energy given by

$$E_{e^-} = h\nu - E_b, \tag{3.9}$$

where h is Planck's constant, ν is the frequency of the incident photon, and E_b is the binding energy of the photoelectron. This expression neglects the recoil velocity of the nucleus, which

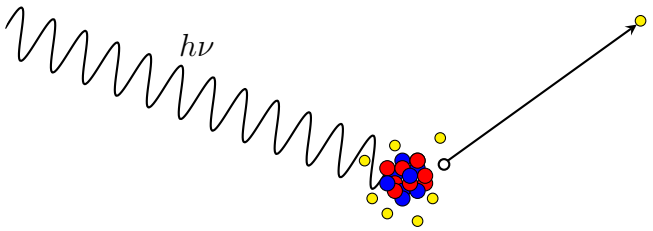

Figure 3.7: An illustration of the photoelectric effect. An incident photon interacts with an atom and deposits its energy, causing the ejection of an electron.

is very small. Characteristic X-rays or Auger electrons are generated as the vacancy left by the photoelectron is filled. If the energy of these secondary radiations is absorbed in the detector, the result is the detection of the full energy of the incident γ ray. This is the ideal case for γ-ray spectroscopy, as the identification of γ-ray energies corresponding to specific transitions may be done by inspecting the spectrum of observed photon energies. However, this process typically is dominant only at photon energies below about 140 keV (see Fig. 12.17 in Ref. [45]), and for germanium detectors gives way to Compton scattering for photon energies above roughly 200 keV (see Fig. 2.20 of Ref. [45]).

Compton scattering is another process by which a γ ray may interact with a detector and is illustrated in Fig. 3.8. In this process, a photon scatters from an electron in the medium, imparting to the electron some but not all of its energy. The electron will then recoil while the lower-energy photon propagates away at some angle θ relative to its previous trajectory. The energy of the scattered γ ray is given by

$$h\nu' = \frac{h\nu}{1 + (h\nu/m_e c^2)(1 - \cos\theta)}, \tag{3.10}$$

where $h\nu$ and $h\nu'$ denote the photon energy before and after scattering, respectively. The

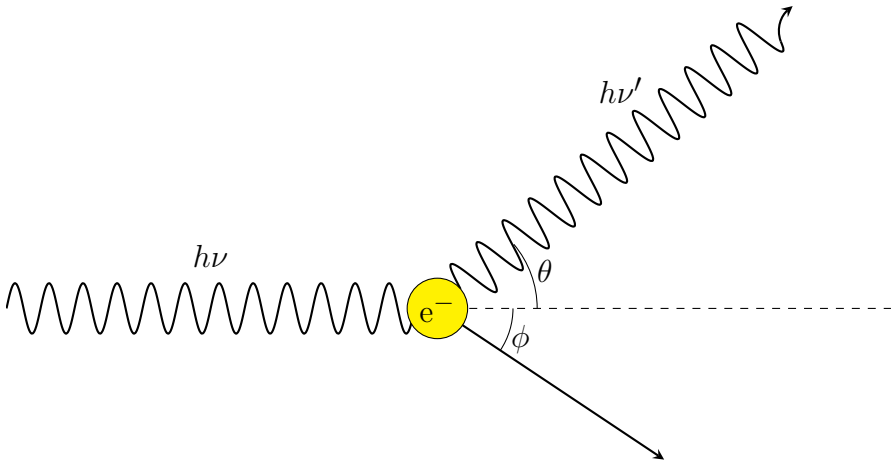

Figure 3.8: An illustration of the process of Compton scattering. An incident photon with energy $h\nu$ interacts with an electron in the medium and imparts some of its energy to it. The scattered photon then propagates away at an angle θ with respect to its original trajectory and with a lower energy $h\nu'$, given by Eq. 3.10, while the electron recoils away at some other angle ϕ and energy given by Eq. 3.11.

energy of the photoelectron, which is the amount of energy that will be registered in the detector, is then the difference between the energy of the photon before and after scattering:

$$E_{e^-} = h\nu - h\nu' = h\nu \left(\frac{(h\nu/m_e c^2)(1-\cos\theta)}{1+(h\nu/m_e c^2)(1-\cos\theta)} \right). \tag{3.11}$$

For a given photon energy, the only parameter in this expression is the scattering angle θ, and it is useful to examine the limiting cases of scattering at $\theta \approx 0$ and $\theta = \pi$. In the $\theta \approx 0$ case, it is evident from Eq. 3.10 that $h\nu' \approx h\nu$ and so the scattered photon deposits almost no energy in the detector. In this case, the photoelectron has very low energy (as shown by Eq. 3.11) and the event is essentially undetected. On the other hand, for the $\theta = \pi$ case, the energy transferred to the photoelectron is maximized:

$$E_{e^-} = h\nu \left(\frac{2h\nu/m_e c^2}{1+2h\nu/m_e c^2} \right). \tag{3.12}$$

However, the photon still carries away a portion of its original energy. There is also a probability for the photon to scatter into other angles, and the cross-section for scattering at any given angle is predicted by the Klein-Nishina formula [51]:

$$\begin{aligned}\frac{d\sigma}{d\Omega} =& Zr_0^2 \left(\frac{1}{1 + (h\nu/m_e c^2)(1 - \cos\theta)} \right) \\ & \times \left(1 + \frac{(h\nu/m_e c^2)^2 (1 - \cos\theta)^2}{(1 + \cos^2\theta)[1 + (h\nu/m_e c^2)(1 - \cos\theta)]} \right),\end{aligned} \tag{3.13}$$

where r_0 is the classical electron radius. For a given photon energy, this distribution leads to a γ-ray spectrum that has a large continuum for Compton scattering, in contrast to the single photopeak present for photoelectric absorption. Neglecting detector efficiency effects, the continuum reaches from zero energy up to the maximum given by Eq. 3.12, with no peak corresponding to the energy of the incident γ ray. However, if the scattered photon undergoes subsequent interactions within the detector volume, it may deposit some or all of its remaining energy and in this case the full-energy peak may be observed.

Finally, for sufficiently high-energy γ rays, pair production may occur. In this process, a photon is converted into a positron-electron pair in the electric field near a nucleus in the detection medium, as illustrated in Fig. 3.9. This process is only energetically allowed if the incident photon has an energy of at least the mass of the newly created particles: $h\nu \geq 2m_e c^2 = 1.022$ MeV. Any remaining energy from the photon goes into the kinetic energy of the pair. Both particles quickly slow as they travel through the medium, but the positron will eventually annihilate with another electron, creating two photons with energy $m_e c^2 = 511$ keV. One or both of these photons may then escape from the detector, giving rise to a spectrum characterized by the full-energy peak for the photon, plus a *single-escape peak* 511 keV below the full-energy peak corresponding to the escape of one photon from the

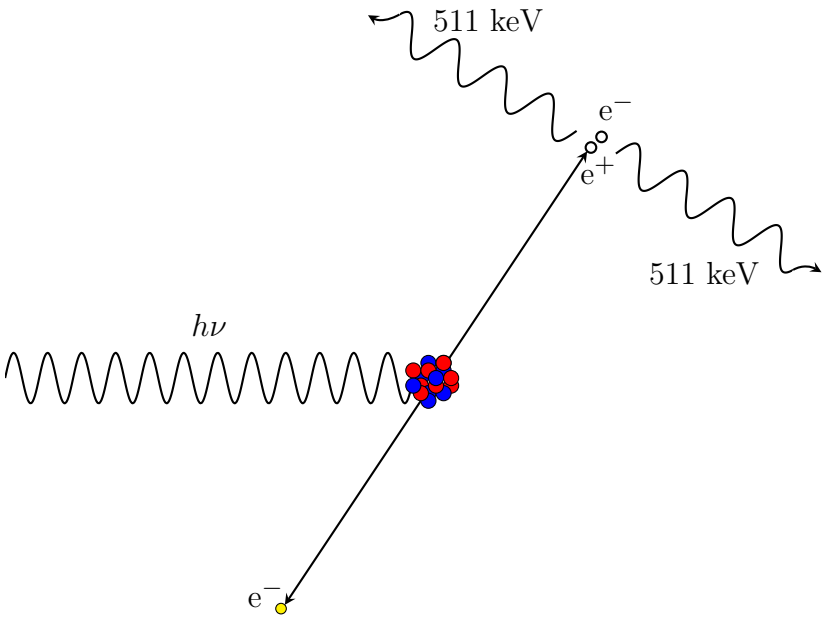

Figure 3.9: An illustration of the process of pair production. If a photon has at least 1.022 MeV of energy, it may be absorbed by a nucleus and an electron-positron pair emitted in its place. The positron will annihilate with another electron in the medium and release two 511 keV photons, one or both of which may escape the detector.

detector, and a *double-escape peak* 1.022 MeV below the full-energy peak corresponding to the escape of both of the annihilation photons.

3.2.2.2 The SeGA detector array

One of the γ-ray detection devices used in the experiments described in this work is the Segmented Germanium Array (SeGA) [52], specifically for the study on ^{70}As presented in Ch. 4. As the name implies, SeGA is an array of 18 high-purity germanium detectors whose crystals have been electrically segmented to provide sensitivity to the position at which γ rays interact with the crystal. This position sensitivity is important because the γ rays detected in the experiments in this work are Doppler shifted according to the relation

$$E_\gamma^{cm} = \gamma(1 - \beta\cos\theta)E_\gamma^{lab}, \tag{3.14}$$

where the superscripts *cm* and *lab* indicate the photon energy in the center of mass frame and in the laboratory frame, respectively, and θ is the emission angle of the photon in the laboratory frame relative to the beam axis. Since the energy is measured in the laboratory frame, the relation above must be used to find the γ-ray energy in the center of mass frame, and therefore accurate knowledge of the emission angle (as well as the beam velocity) is critical for good final energy resolution. The remainder of this section will describe the characteristics of the SeGA detectors and their use in the present work.

Each of the detectors that comprise SeGA are composed of a highly-segmented germanium crystal. The germanium itself is of high-purity n-type material (sometimes called ν-type to distinguish high-purity material with residual donor impurities from material which is intentionally doped with donor atoms). The crystals are cylindrical with a diameter of 7 cm and a length of 8 cm. Electrical contacts are placed along the outside of the crystal that divide the detector into 8 disks of 10 mm width along the axis of the cylinder, and each disk is further divided into four quadrants to give a total of 32 segments which are individually read out (see Fig. 3.10). In addition, there is a central contact in the center of the crystal so that the total energy deposited in the crystal can be read out in addition to the energy deposited in each segment. The crystal is kept cold at roughly 100 K by thermal contact with a dewar of liquid nitrogen, mounted at a 45° angle to the crystal axis.

The operational characteristics of SeGA depend heavily on the arrangement of the detectors during an experiment. While many different considerations may go into choosing an experimental configuration for the detectors, often the choice is centered around optimizing the trade-off between γ-ray detection efficiency and energy resolution. Efficiency can be increased by placing the detector crystals as close as possible to the γ-ray source in order to maximize the solid angle which the crystals cover, thereby increasing the probability that a

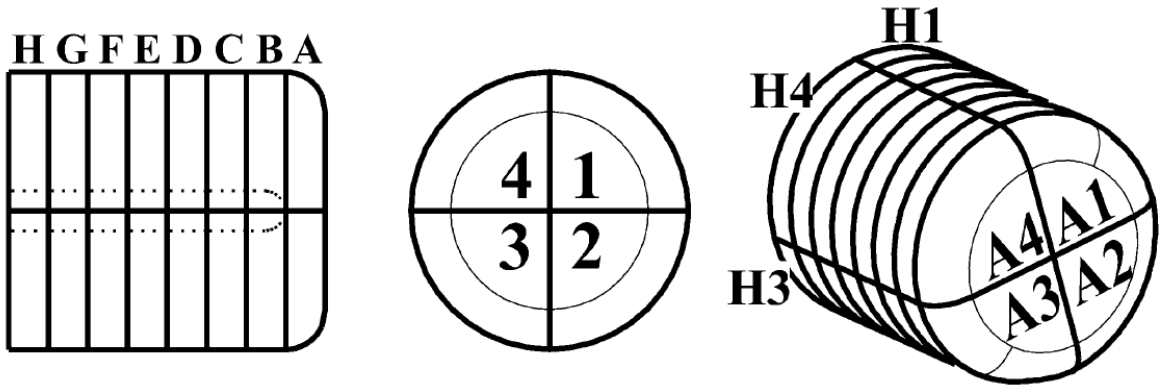

Figure 3.10: An illustration of the segmentation scheme of the crystals of the SeGA detectors, as well as the nomenclature used to identify each segment. The crystals are divided into eight disks with a width of 10 mm each, labeled A through H along the axis of the cylindrical crystal. Each disk is further segmented into quarters numbered 1 through 4, with quarters 2 and 3 closest to the beampipe for the setup described in this work. Figure adapted from [52].

photon will pass through the detectors' active volume. However, doing so has implications for the energy resolution of the array. As indicated by Eq. 3.14, there are three quantities that are needed to compute the center of mass energy of a γ ray emitted from a nucleus moving at relativistic speeds: the velocity as a fraction of the speed of light (β), the angle of emission (θ), and the photon energy measured in the lab frame (E_γ^{lab}). Each of these parameters contributes to the resolution of the γ-ray energy:

$$\left(\frac{\Delta E_\gamma^{cm}}{E_\gamma^{cm}}\right)^2 = \left(\frac{\beta \sin\theta}{1-\beta\cos\theta}\right)^2 (\Delta\theta)^2 + \left(\frac{\beta-\cos\theta}{(1-\beta^2)(1-\beta\cos\theta)}\right)^2 (\Delta\beta)^2 + \left(\frac{\Delta E_\gamma^{lab}}{E_\gamma^{lab}}\right)^2 . \tag{3.15}$$

The intrinsic resolution of the detectors (the final term in this expression) has been determined to be $\sim 0.2\%$, but the other two terms can be much larger, on the order of about 1% (see text and Fig. 1 of [52]). In particular, the first term includes a factor in $\Delta\theta$, and as the detectors are brought closer to the γ-ray source, the solid angle of the segments used to

determine the emission angle becomes wider and therefore causes this term to grow.

The trade-off between detector efficiency and energy resolution has caused several different standard configurations to be developed for SeGA, each designed to optimize the performance of the array for specific science goals. For the experiment on ^{70}As, a configuration known as the "barrel" or "beta" configuration was chosen. In this configuration, SeGA consists of fifteen detectors arranged in two rings of detectors with the crystal axes aligned with and roughly 13 cm from the beam axis. One ring is composed of eight detectors covering emission angles of roughly 95° to 125° relative to the target (the "backward" ring), and the other ring of seven detectors covering roughly 50° to 80° with respect to the target (the "forward" ring). The forward ring had one less detector to allow space for a gatevalve in the beamline. This gives a detection efficiency for 1 MeV photons of roughly 7%, which was important for the ^{70}As experiment, while still giving sufficient energy resolution. See Ref. [53] for other possible configurations of SeGA.

3.2.2.2.1 SeGA calibrations As SeGA consists of many separate germanium crystals which operate independently of one another, each detector will exhibit a different response to γ rays of the same energy, as shown in Fig. 3.11. Therefore, in order to make use of the array in an experiment, it is necessary to calibrate SeGA against a source of γ rays with known energies in order to ensure that each detector will give the same response. For this purpose, in the ^{70}As experiment data were taken with several different radioactive check sources, including ^{56}Co, ^{133}Ba, ^{152}Eu, and ^{226}Ra.

Calibrating the SeGA detectors first requires determining the centroids of the peak positions for a radioactive source with well-determined γ-ray transition energies. These peak positions are then matched to the known peak positions and a fit is performed using a second

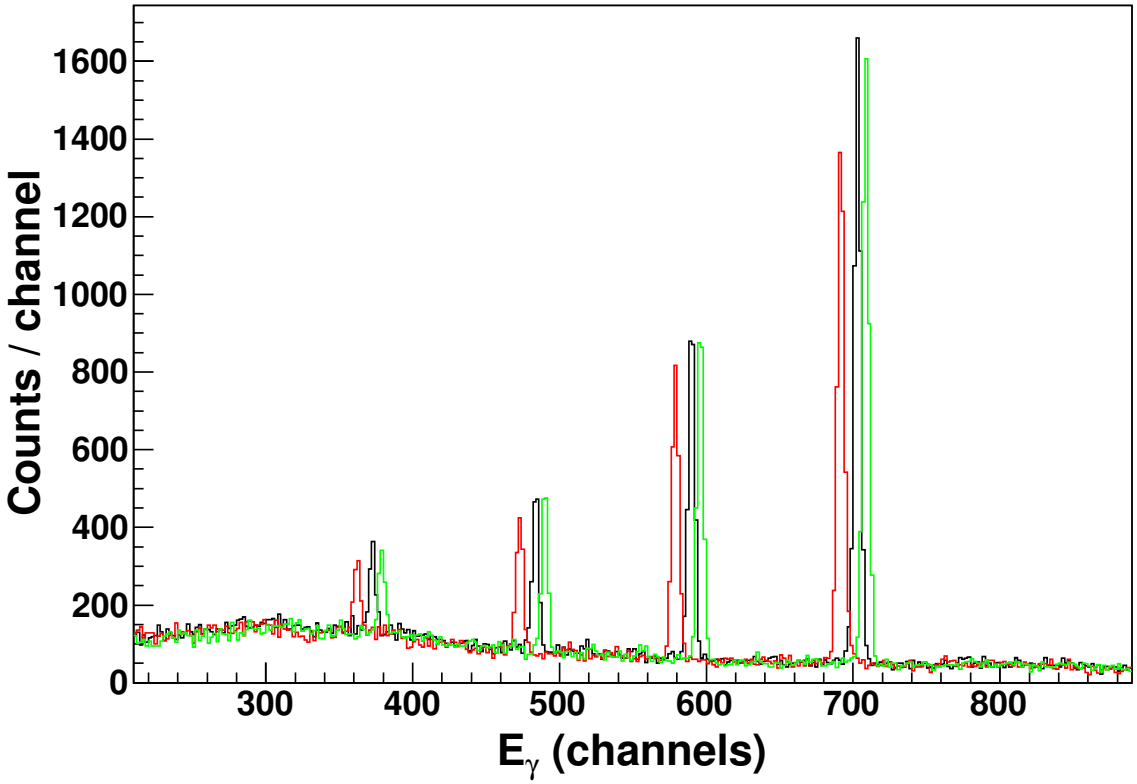

Figure 3.11: The response of several SeGA detectors to a ^{226}Ra source before calibration. The photopeaks from each detector are clearly misaligned, which would result in a γ-ray spectrum for the entire array with poor resolution. The detectors are therefore calibrated to match the raw signal in ADC channels to the actual γ-decay energies, which are well-known.

order polynomial to map the uncalibrated energies to the calibrated energies for each crystal. A χ^2 minimization is used to determine the parameters of the fit, and these parameters are then used to align the peaks in each crystal so that when the spectra from all the detectors are summed the photopeaks are aligned. However, the segments of each crystal also provide energy information and must be calibrated as well. This is a much more complicated problem, as there is cross-talk between the segments that causes the calibration to depend on the number of segments which register an interaction in an event (the "fold" of the event). For single-fold events, the energy deposited in the segment must be the same as that for the central contact, and so the second-order polynomial fit can be performed to match the

segment calibration to the central contact calibration. Similarly, a χ^2 fit is performed to match each pair of calibrated segments to the central contact energy in 2-fold events, which results in $32 \times 31/2$ sets of calibration parameters, showing how quickly the number of parameters grows with the fold of the event. Higher-fold events are therefore calibrated using a correction derived from the single-fold and two-fold events. This process is described in Ref. [54].

3.2.2.3 The GRETINA detector array

While SeGA provides good energy resolution, the next generation of γ-ray detectors aims for significantly better resolution. To this end, the development of a new detector array called the Gamma-Ray Energy Tracking In-beam Nuclear Array (GRETINA) [55] has been undertaken. This is part of a project to construct a larger array, the Gamma-Ray Energy Tracking Array (GRETA) [56], which will cover a full 4π of solid angle. The experiment on ^{74}Rb described in this work was performed using GRETINA during its first experimental campaign at the NSCL. This subsection will therefore describe the characteristics of the array as it was during this first campaign.

During the experiment on ^{74}Rb described in Ch. 5, GRETINA was composed of seven detector modules (called "quads"), each of which contains four hexagonally-shaped high-purity germanium crystals. There are two different irregular hexagonal geometries of crystal (type A and type B), and each quad contains two of each type. Similarly to SeGA, each crystal is electronically segmented; however, the GRETINA crystals are divided into six slices of width 8 mm, 14 mm, 16 mm, 18 mm, 20 mm, and 14 mm in order from the face to the back of the crystal. Each slice is further divided into six segments, for a total of 36 segments per crystal. The electronics for reading out the photon signals are housed just behind the

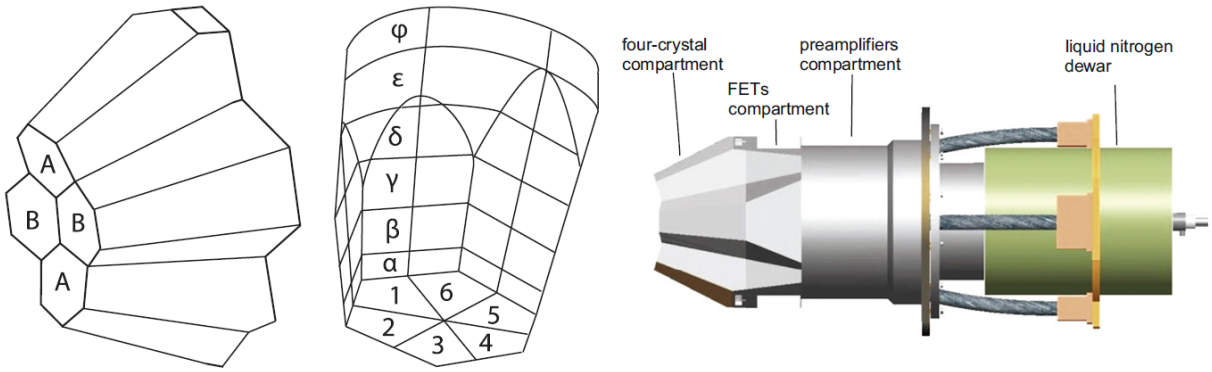

Figure 3.12: An illustration of the segmentation of the GRETINA crystals, as well as the modules as a whole. The crystals are segmented into layers which are, in order from the layer labeled α to ϕ, of thickness 8, 14, 16, 18, 20, and 14 mm. On the far left is the arrangement of the two different hexagonal geometries used for grouping the crystals into a quad. Figure adapted from [55].

crystals, and a dewar of liquid nitrogen keeps the crystals cold. For an illustration of the GRETINA detector modules, as well as the segmentation of the crystals, see Fig. 3.12.

Although both SeGA and GRETINA make use of segmented germanium crystals, the design of GRETINA actually represents a significant advancement in γ-ray detection technology. This is due to two features of GRETINA: *signal decomposition* and *γ-ray tracking*. The signal decomposition is one of the most important aspects of GRETINA, in that it allows the γ-ray interaction position to be determined with subsegment resolution. In order to do so, a set of simulated detector responses to the deposition of a unit of charge at various locations in the crystal are generated. This set of simulated responses is called a *basis*. The basis signals are generated for a grid of non-uniform spacing with an average distance between points of 1 mm. When a γ ray interacts with the crystal, it will generate a signal in the segment it hits as well as an image charge in the surrounding segments. By fitting the basis signals to the real and image charge signals in the detector, the position of the interaction can be determined. The fit can also be performed for multiple-scattering by the

same photon in the crystal, in which case the basis signals are fit to the linear combination of signals generated by the multiple hits from multiple-scattering events. During testing, the resulting position resolution of the detectors was found to be roughly 2 mm [55], significantly better than assuming that the hit occurred at the center of the segment.

GRETINA is also designed to have the ability to do γ-ray tracking. This is the capability to examine an event in which the array experienced multiple photon scattering events in the crystals and reconstruct the path(s) of the photon(s) that interacted with the detectors. This is done by grouping the interaction points according to the likelihood that they originate from the same photon. Next, for each group of points a scattering sequence is generated and compared to the Compton scattering formula (Eq. 3.11) and a figure of merit is generated according to how well the deposited energies and angles of the scattering sequence agree with the Compton formula. The sequence is permuted for all possible orderings. A detector that had perfect energy and position resolution would have a figure of merit of zero for a fully absorbed photon. In practice, the figure of merit will not be exactly zero for a correctly reconstructed scattering sequence, but the figure of merit should be large for partial absorption or incorrect reconstruction. Finally, other possible clustering arrangements of the interaction points may be iterated to seek an optimum solution. Placing a condition that only events in which the figure of merit is above a certain threshold then eliminates events that can be identified as only partial deposition of the γ-ray energy, resulting in a spectrum with an increased ratio of events in the full-energy peak compared to those that populate the Compton continuum.

For the ^{74}Rb experiment, GRETINA was set up in a "standard" configuration, with four quads positioned to cover angles of roughly 20° to 50° and the remaining three quads placed around 70° with respect to the beam axis. This provided the necessary sensitivity to the

lifetime of the state being investigated (see Ch. 5 for more details). The signal decomposition is done automatically, as it is key to the superior energy resolution of GRETINA, and is available on-line during experiment. However, it was found that γ-ray tracking was not necessary for this particular experiment, and so this capability was not used in the present work. Finally, the software GrROOT [57], which was developed for the GRETINA campaign at the NSCL, was used for unpacking the data from the NSCL event format into ROOT [58] objects.

3.2.2.3.1 Calibration of GRETINA In order to operate effectively, the GRETINA detectors must be calibrated. Similarly to SeGA, this may be done using radioactive check sources in order to map the measured energy in ADC channels to the actual γ-ray energies emitted by a given source. The experiment on ^{74}Rb presented in this work was performed as part of a year-long campaign of experiments with GRETINA at the NSCL, and so the detectors remained in a calibrated state between experiments. This calibration was checked before each experiment to ensure that the calibration parameters had not changed. For the data presented in this work, this check was done by comparing the energies recorded for a ^{152}Eu source in each crystal against the known source energies. A linear fit was performed to extract "recalibration" parameters for each crystal and these parameters were used in the data analysis to account for any drift in the calibration. For the γ-ray energies of interest for the ^{74}Rb study ($\sim$450 keV), this resulted in a typical correction of less than 1 keV.

3.2.3 The TRIPLEX plunger device

The TRIple PLunger for EXotic beams (TRIPLEX) [59, 60] is a device used to precisely position various experimental targets along the axis of the beamline. The TRIPLEX is

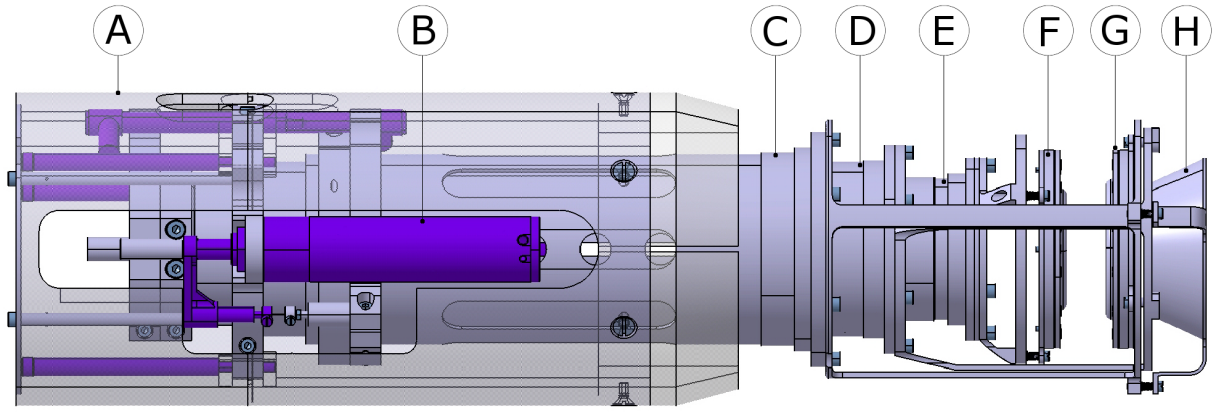

Figure 3.13: A schematic drawing of the TRIPLEX plunger device. The components are labeled as follows: (A) The outer casing of the TRIPLEX. (B) One of the piezoelectric motors for positioning the targets. (C) The outermost movable cylinder, to which the second degrader is attached. (D) The central, immobile cylinder to which the first degrader is attached. (E) The innermost movable cylinder to which the target is attached. (F) The target, positioned by the moving cylinder E. (G) The first degrader, held at a fixed position. (H) The second degrader frame, on which the second degrader (obscured by the first degrader) is mounted.

in the class of devices known as "plungers" commonly used in Recoil Distance Method lifetime measurements. Unlike most plungers, however, which typically support mounting at most two foils, the TRIPLEX is designed to support three foils in the path of the beam. This addition is critical for enabling the use of the Differential Recoil Distance Method (section 2.3), among other possible uses.

The design of the TRIPLEX is shown in Fig. 3.13, highlighting its various components. The three foils are mounted on frames which are attached to the plunger by screws. The middle foil is stationary, but the other two may be moved up to 25 mm away from the center foil. This movement is achieved by moving the cylindrical tubes on which the foils are mounted relative to the one on which the central foil is mounted. The tubes themselves are moved by two piezoelectric stepping motors. Each motor contains several pairs of piezoelec-

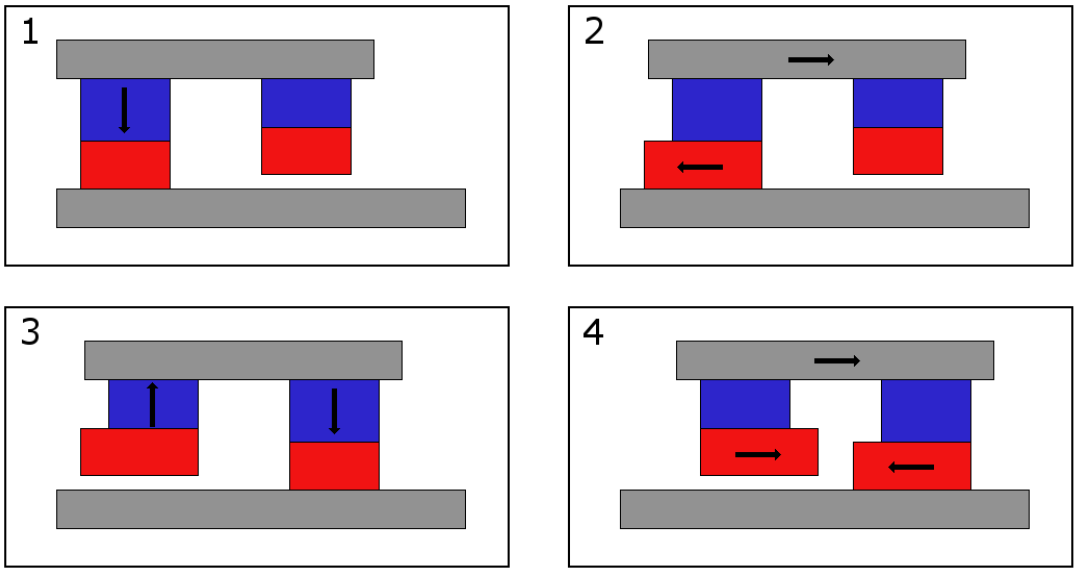

Figure 3.14: An illustration of the operation of the piezoelectric stepper motors used in the TRIPLEX plunger. The red and blue rectangles are the piezoelectric elements while the gray bars are the runner and the wall of the chamber containing the stepper motor. Starting with frame 1, a potential is applied to one of the blue piezoelectric elements, causing it to expand and clamp to the wall. Another potential is then applied to the red element on the end of the blue element, causing it to expand and move the stepper assembly to the right in frame 2. The potential is then switched from one blue element to the other, switching which one is clamped (frame 3), and then the red element on the right has a potential applied to move the assembly to the right again, while the potential on the red element on the left is reversed to prepare it for the next step. This process is then repeated until the assembly has moved the desired distance.

tric elements attached to each other as well as to a runner, as shown in Fig. 3.14. Whenever an electric potential is applied to the elements, they expand along the direction of the applied electric field. To achieve motion, a potential is applied to the elements attached to the runner so that they expand and clamp against another surface. Then, another potential is applied so that the piezoelectric elements deform along the axis of the runner, causing it to move. The remaining elements are then clamped while the original elements are allowed to unclamp and the deforming potential is reversed so that the motion is continued in the same direction. By performing this process (shown in Fig. 3.14) repeatedly, uniform motion can

be achieved.

There are three methods for verifying the position of the three foils relative to one another. First, the motors internally track how far they have moved and report a position relative to their starting position when they are initially given power. Testing has shown that these reported positions are generally reliable, but may begin to show some drift when the motors are operated near the extremes of their range. A second method involves two micrometers, one each for the position of the first foil relative to the second, and the third to the second. These micrometers are extremely precise and can be used as a check against the positions reported by the motors. However, they have a limited range which is less than the range of motion of the motors. They are also fragile and may be damaged if too much force is applied to them. Finally, the three mounting locations of the plunger are electrically isolated from each other, which allows capacitive measurements of the distance to be used. Since the foils are usually flat pieces of metal, they resemble parallel plate capacitors, and therefore the TRIPLEX is designed to allow an electrical potential to be applied to the middle foil and the induced signal read out from the other two foils. If properly calibrated, the control software of the TRIPLEX is able to translate this capacitance into a position. Under conditions in which the foils are thin enough that they may deform under the application of the beam, such as low-energy experiments with beam energies less than about 10 MeV/nucleon, the software can even use this capacitance measurement to correct the separation of the foils in real time via a feedback mechanism. However, as this was not necessary for the present work, this feedback mechanism was not used. Instead, the capacitance reading was used to note the precise moment when contact was achieved between the foils, and this was used to define the "zero distance" for the motor and micrometer readings.

3.3 Geant4 simulations

Much of the work to extract lifetimes from the experimental γ-ray spectra is performed with the aid of the Geant4 simulation package [61]. These simulations need to accurately reproduce all of the important aspects of the experimental setup as well as handle the appropriate physics processes. Geant4 itself is designed to take care of the physics processes, including the physics of the beam propagating through target materials and photon physics. For the specific needs of the experiments described in this work, a simulation package previously developed and used at the NSCL [62] was employed. This package has been updated so that it incorporates both the SeGA and GRETINA detector systems in the geometries used in this work. This section will briefly describe the operation of the simulation software and the manner in which it is used to analyze lifetime data.

The simulation software accepts many parameters in order to accurately describe an experiment. Many of these are determined by the equipment used in an experiment. As the simulation is designed to be used for lifetime measurements at NSCL, it accepts input which tells it whether to use a single target, a classic two-foil plunger, or the TRIPLEX plunger. It can also accept values for the material type, thickness, position, and a factor by which to scale the density of each target in order to reproduce the measured energy loss in the experiment. There is also the possibility to translate the plunger away from its default position within the simulation. With respect to the detector systems involved, the simulation is able to virtually construct either SeGA or GRETINA and use it as a detector system for γ rays. For SeGA, this includes the capability to translate and rotate each SeGA detector individually to precisely reproduce the experimental setup. The description of the SeGA detectors is also very complete, including both the active volumes of the detectors as well as

the crystal housings and dewars, and includes the ability to simulate the individual segments of SeGA. For GRETINA, the individual quads are described and can be positioned precisely in a similar manner to SeGA. However, instead of individual segments, the simulation mimics the position sensitivity of GRETINA by taking the actual interaction point of a photon in the simulated detector volume and shifting it according to a three dimensional gaussian distribution with a variable width parameter. In this way, the observed position resolution can be matched in the simulation.

In addition to the parameters which describe the experimental setup, the simulation also accepts many values which describe the experimental conditions specific to a given nucleus. These include the position, spatial extent, energy, momentum spread, and angular spread of the incoming beam; the change in charge and mass number undergone in a reaction in a foil, the probability that the reaction will happen in a given foil as opposed to the others, and the change in momentum of the reacted beam due to the reaction; and the charge state of the outgoing beam, a reference energy that the outgoing beam is expected to have, and the acceptance of the S800. Finally, the simulation accepts parameters which describe one or more excited states in the nucleus that results from the reaction on the target, including the excitation energy of the states, the energy of the γ rays coming from these states, the fraction of the nuclei produced which populate each state, and the lifetime of each state. In this way it is possible to describe the beam itself and reproduce a potentially complicated level scheme involving many excited states which decay to each other.

With all the relevant parameters set, the simulation program can be executed. The parameters can be set at runtime in interactive mode or a set of macros can be defined to automate the process. Once executed, the program will use Monte Carlo methods to generate incoming beam particles in a distribution defined by the given incoming beam parameters.

The simulation will then propagate the beam through the various foils, simulating the energy loss that the beam particles experience as they pass through the material. According to the parameters entered, the simulation will select one of the foils to be the one in which the beam undergoes a reaction, producing the outgoing nucleus in one of the states defined in the input file. The parameters that determine the outgoing beam momentum include a fraction of the momentum that is lost in the reaction, the width of a gaussian profile that is sampled to create a spread in the outgoing momentum, and finally the strength of a kick in a random direction. If the outgoing nucleus is in an excited state, the program will sample the decay curve of the excited state based on its entered lifetime and determine the location at which it will decay, propagating the nucleus to that point and emitting a γ-ray according to the given decay properties of that state. The photon emission distribution is isotropic, and if it encounters part of the detector volume its interaction will be determined by the included Geant4 physics processes. The response of the detector is then reproduced, including the various possible photon-material interactions, and the energy deposited in the germanium crystals recorded. This continues until the nucleus has deexcited to its ground state. This process is then repeated many times until a given number of beam particles have been simulated.

Once the program has finished simulating the experiment, it will output a set of histograms that can be compared to experimental data. Internally, it uses the ROOT analysis package [58] to store data during the simulation process, then generates a predefined set of histograms from this data. These histograms are then written to a ROOT file which can be opened and manipulated by the user. The tree structure which stores the data internally can also be written to file, although this is atypical as the files are very large. Since the experimental data in this work was also analyzed using the ROOT package, it is then possi-

ble to directly compare the simulations of data with those from the simulation for analysis purposes.

In this work, the simulations are fit to the data using a χ^2 minimization procedure. A short overview of this procedure is given here, which represents a summary of the information found in Ref. [63]. If the data is represented by a histogram with N bins denoted x_i, where i is the index of a bin, and the simulation by a histogram with the same number of bins denoted y_i, then the quantity χ^2 is calculated by

$$\chi^2 = \sum_{i=1}^{N} \frac{(x_i - y_i)^2}{\sigma_i^2}, \tag{3.16}$$

where σ_i is the uncertainty in the number of entries in bin i of the data. If the simulation reproduces the spectral shape of the experimental spectrum well, then the χ^2 will be small, as the differences between the data x and the simulation y will be small. However, if the simulation doesn't reproduce the data (if, e.g., the lifetime input to the simulations is not the true lifetime), then the χ^2 will be large. This provides a metric by which to gauge the goodness of a particular fit. By fitting many simulations with different lifetimes to the data, a distribution of χ^2 can be generated, and the minimum taken to be the "best fit." If this distribution of χ^2 is quadratic in the lifetime, then the χ^2 for a value of the lifetime which is one standard deviation away from the minimum χ^2 is given by

$$\chi^2 = \chi^2_{\text{min}} + 1. \tag{3.17}$$

This provides a useful way of determining the uncertainty in the lifetime. However, it is also important to judge whether the obtained χ^2 indicates a good fit or not. This can be done,

assuming that the individual bins of the data are independent and the simulation gives the correct spectral shape, by noting that the minimum value of the χ^2 should be distributed according to the χ^2 distribution:

$$f(z;n) = \frac{1}{2^{n/2}\Gamma(n/2)} z^{n/2-1} e^{-z/2}, \tag{3.18}$$

where z is a continuous variable (the lifetime, in this case), n is the number of degrees of freedom of the fit, and Γ is the gamma function defined by

$$\Gamma(x) = \int_0^\infty e^{-t} t^{x-1} dt. \tag{3.19}$$

The expectation value of the χ^2 distribution is the number of degrees of freedom, which in the present case is the number of bins less the number of fit parameters fixed from the data. For a good fit, then, it is expected that $\chi^2/n = 1$. This condition can therefore be used to judge the quality of the fit, and in conjunction with the procedure for finding the uncertainty, is used to determine the lifetime in the analyses presented in this work.

Chapter 4

Lifetime Measurements in ^{70}As

The first of the lifetime analyses to be discussed in this work was done on $^{70}_{33}As_{37}$ [64]. This experiment used the lineshape method to determine the lifetimes of the 8^+_1 and 9^+_1 states of this nucleus. More specifically, the analysis applied the lineshape method to γ-γ coincidence data, where it was required that a γ ray populating the state of interest be observed in the same event as a γ ray depopulating the state. This presents an experimental challenge, as the γ-ray yield is substantially reduced in a coincidence measurement and therefore maintaining sufficient statistics for an accurate measurement becomes difficult. However, as ^{70}As is an odd-odd nucleus (i.e. it has an odd number of both protons and neutrons), it has a high level density of excited states which are interconnected. This makes it difficult to ensure that the shape of the γ-ray spectrum being studied is due to just one transition and not multiple transitions superimposed on one another. In addition, with significant feeding, it is possible that a given state may appear to have a longer lifetime than it actually does due to the influence of the lifetime of a feeding level. The use of γ-γ coincidence was therefore necessary for this analysis, and also demonstrates an important tool for the determination of lifetimes in similarly complicated nuclear systems where the analysis of γ-ray singles spectra may prove insufficient.

4.1 Physics motivation

The motivation for studying ^{70}As was to understand the structure of this nucleus. ^{70}As is located in a region of the nuclear chart which is known to be a location where nuclear structure is rapidly evolving [16, 32]. For instance, nuclear systems of roughly mass 70 near the $N = Z$ line have been shown to rapidly change their shapes as a function of the number of protons and neutrons they have [60, 65, 66]. In addition, as more nucleons are added to nuclei in this mass region, they exhibit greater levels of collectivity and this behavior is attributed to increasing occupation of the $g_{9/2}$ orbital, which is understood to drive the collectivity in this region [67]. However, for nuclei which have $A \lesssim 70$, it can be expected that their low-lying states can be described by nucleons that occupy primarily the p and f shell-model orbitals. Still, in higher-lying excited states these nuclei may show evidence of the $g_{9/2}$ orbital [68] as nucleons are promoted out of the p and f orbitals. Studying the excited states of ^{70}As and looking for evidence of collective behavior can therefore provide information about the structure of these states.

Another aspect of ^{70}As that needs to be considered is that it is an odd-odd nucleus. Without collectivity, an odd-odd nucleus can be described primarily by the coupling between the last proton and last neutron which are then coupled to the rest of the nucleons in the form of an even-even core. In such an arrangement, the excited states of the nucleus are built primarily upon the interactions of the two odd nucleons, and so the transitions between these excited states can be expected to display a strongly single-particle character. On the other hand, for states that are at sufficiently high excitation energy, the odd particles may be promoted into the $g_{9/2}$ orbital, which might be expected to cause the nucleus to evolve collective characteristics as mentioned above. Therefore, it is also of interest to understand

how nuclei evolve with increasing excitation energy, as well as changing nucleon number.

There have been a number of previous studies performed on ^{70}As that have provided information about its nuclear structure. In addition to identifying many excited states and assigning spin and parity values to them, some studies have sought to interpret the structure of the nuclear states in terms of the excitations of the two odd particles. It was found that the ground state can be described by placing both the odd proton and the odd neutron into the $f_{5/2}$ orbital, and several excited states were described in terms of the coupling of the odd proton and odd neutron in the $f_{5/2}$, $p_{3/2}$, $p_{1/2}$, and $g_{9/2}$ orbital space [69, 70]. This would lend support to the premise that ^{70}As does not exhibit strong collective features. Indeed, in Ref. [70] it was found that the low-lying states are well-described by a spherical shape and in Ref. [69] there was no evidence found for collective behavior when the odd nucleons are not both in the $g_{9/2}$ orbital. However, a later study found that for the 11^+_1 and 13^+_1 states there is evidence of strong collectivity based on the lifetime measurements of these states [71]. This would indicate that at some point the structure of ^{70}As changes from non-collective to collective. The purpose of the study presented in this chapter is to provide further information about this change in structure.

The two states under investigation in the analysis presented here are the yrast (that is, lowest-lying) 8^+ and 9^+ states in ^{70}As. In both Refs. [69] and [70] the 9^+ state was suggested to belong to the configuration where both the odd proton and the odd neutron are in the $g_{9/2}$ orbital. This claim was based upon the observation that the level energies of the $\frac{9}{2}^+$ states in the neighboring odd-A nuclei sum to roughly the energy of the 9^+ state in ^{70}As (i.e. $E(^{69}\text{Ge},\frac{9}{2}^+) + E(^{69}\text{As},\frac{9}{2}^+) = 397.9$ keV $+ 1306.7$ keV $= 1704.6$ keV [72], compared to $E(^{70}\text{As},9^+) = 1752.2$ keV [73]). This would indicate that the 9^+ state behaves similarly to the lower-lying states which arise from the coupling of the valence nucleons,

in that it behaves as an excitation of the two odd nucleons to the $g_{9/2}$ orbital rather than collectively as the higher-lying states do. The 8^+ level was proposed to also belong to this configuration (referred to as $\pi g_{9/2}\nu g_{9/2}$ hereafter) based on the fact that a strong $M1$ branch was observed to connect the 9^+ and the 8^+ states, which could suggest that the two states have a similar structure since the overlap of their wavefunctions would be large. However, more experimental information can help to set these assignments on firmer ground.

In order to investigate whether the 8^+ and 9^+ states do belong to the $\pi g_{9/2}\nu g_{9/2}$ configuration, the lifetimes of these two states were measured. From this, the strengths of the transitions $B(M1; 9^+ \rightarrow 8^+)$ and $B(E1; 8^+ \rightarrow 7^-)$ can be extracted in order to discuss the structure of these states. As a prediction, the strength of the $9^+ \rightarrow 8^+$ transition should be on the order of unity in single-particle units if the assignment of these states to the $\pi g_{9/2}\nu g_{9/2}$ configuration is correct, since only the last odd nucleons should be participating in the transition. On the other hand, to make a prediction about the strength of the $8^+ \rightarrow 7^-$ transition, some knowledge of the 7^- state is necessary. The stretched configuration $\pi f_{5/2}\nu g_{9/2}$ can account for the spin-parity of the state, and the measured magnetic moment of the state agrees well with theoretical calculations [70, 74]. Therefore, the assignment of this state to the $\pi f_{5/2}\nu g_{9/2}$ configuration can be taken with some confidence. However, this means that the $8^+ \rightarrow 7^-$ transition, which has a dipole character, must connect two states in which the proton makes an angular momentum change of $2\hbar$ between the $f_{5/2}$ and $g_{9/2}$ orbitals, which is forbidden. Given that the transition occurs, it means that if the odd-particle configuration assignments of these two states are accurate then the transition is strongly hindered and proceeds because of small admixtures of other configurations. A similar situation for the starting and ending configurations occurs in the neighboring odd-odd isotope ^{72}As, where the strength of the $8^+ \rightarrow 7^-$ transition is known to be $1.22(16) \times 10^{-5}$ W.u. since the

lifetime [75] and the $E1$ character of the γ ray [76] are known. This is a strongly hindered decay [77], consistent with the proton having to make a $\Delta j = 2$ transition via a forbidden dipole decay. Therefore, if the $8^+ \rightarrow 7^-$ decay has a strength which is similarly hindered, it will support the assignment of the 8^+ state to the $\pi g_{9/2} \nu g_{9/2}$ configuration.

4.2 Experimental details

The experiment that produced the data for this analysis was run in December of 2010 at the NSCL. The primary beam from the cyclotrons was a standard ^{78}Kr beam with an energy of 150 MeV/nucleon and an intensity of 25 particle nano-Amperes (pnA). This primary beam was impinged upon a ^{9}Be target to produce ^{78}Rb via a nuclear charge exchange reaction, rather than the typical fragmentation reactions used at the facility, which was necessary to fulfill other science goals in the experiment. The ^{78}Rb was selected in the A1900 fragment separator, using an aluminum wedge of thickness 240 mg/cm^2 and a longitudinal momentum acceptance of 0.5%. This resulted in a secondary beam that was approximately 70% ^{78}Rb, with an energy of 101.6 MeV/nucleon and a rate of about 1×10^5 particles per second. Figure 4.1 shows the different species present in the secondary beam after purification in the A1900, identified by their time of flight between the extended focal plane (xfp) scintillator in the A1900 focal plane box and the object scintillator in the S800. Software gates were used to remove the remaining components besides ^{78}Rb in the offline analysis. This beam was then transported to the S800 vault for the measurement.

Once the beam reached the experimental station in the S800 vault, further reactions were necessary to produce the ^{70}As nuclei in the appropriate excited states. For this purpose, a second ^{9}Be reaction target of thickness 376 mg/cm^2 was placed at the S800 target position

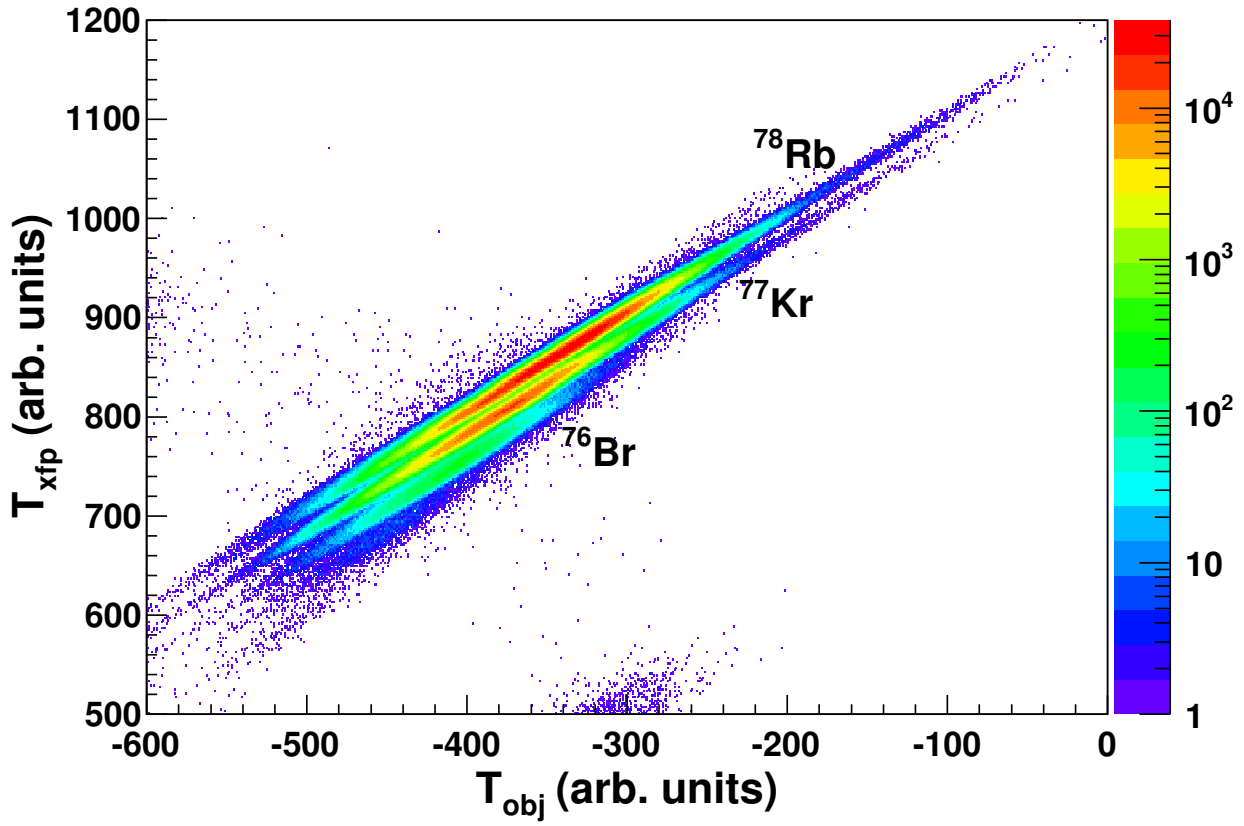

Figure 4.1: The composition of the secondary beam after purification in the A1900 fragment separator, distinguished by their time of flight between the A1900 extended focal plane (xfp) scintillator on the vertical axis and the S800 object (obj) scintillator on the horizontal axis. ^{78}Rb is the primary component, with smaller contributions from ^{77}Kr and ^{76}Br. These latter components were removed with software gates in the analysis.

to induce further reactions in the secondary beam. The beam particles that were within the acceptance of the spectrograph (which was operated in focused mode for this experiment, resulting in a large momentum acceptance of about $\pm 2.5\%$) were then bent through the analyzing dipole magnets to the S800 focal plane. In general, many species of particle will be present in the focal plane detectors. They can be identified by correlating their time of flight from one of the scintillators in the beamline (the obj scintillator in this case) with their energy loss in the S800 ionization chamber. As shown by Eq. 3.6, the energy loss of an ion in a material is proportional to the square of the charge of the ion, Z^2, which gives

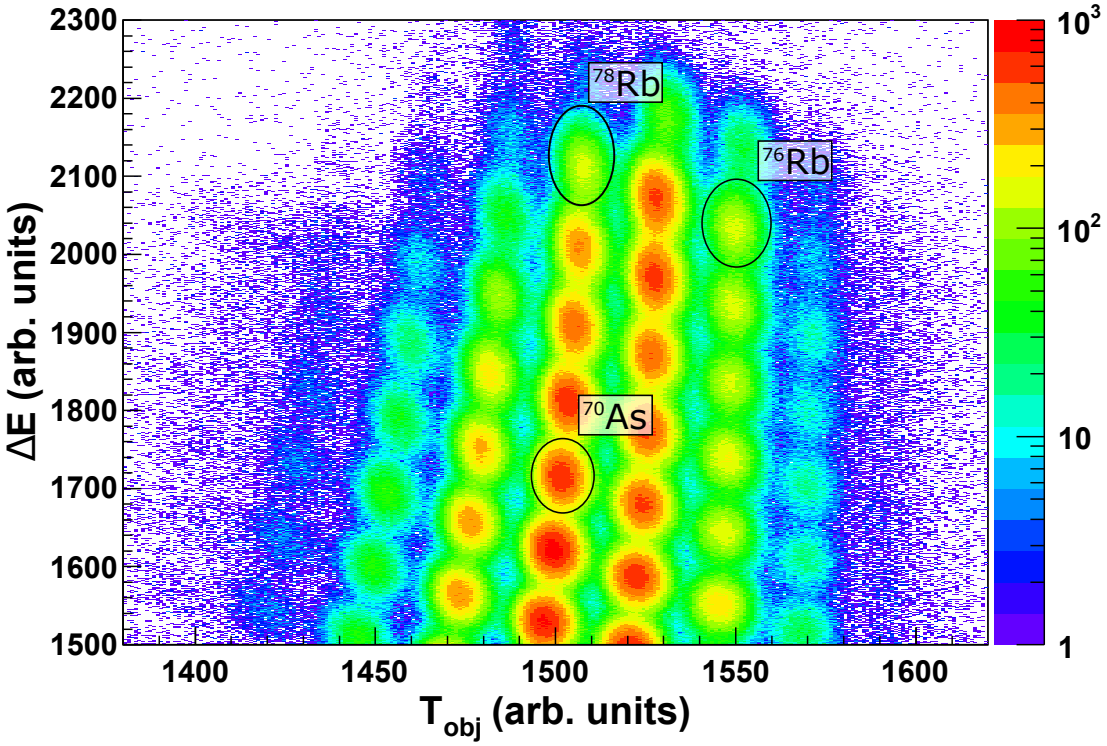

Figure 4.2: A plot of the energy loss ΔE vs. time of flight T_{obj} of each particle used to identify the various nuclei produced in the reaction of the secondary beam. The energy loss separates elements vertically according to Z^2 while the time of flight separates isotopes horizontally according to A/Z (note that for this plot, the horizontal axis has been reversed, so that increasing time of flight corresponds to decreasing A/Z). This results in the slanted lines shown. Stepping right along a "horizontal" line corresponds to removing one neutron per locus, as shown by the labeled Rb isotopes. Moving vertically downward along a "column" corresponds to removing one proton and one neutron per locus. Thus, moving the four loci from ^{78}Rb to ^{70}As in the figure corresponds to removing four protons and four neutrons.

elemental separation. Meanwhile, the time of flight T_{obj} is related to the ratio of the mass to the charge:

$$B\rho = \frac{m}{q}v \approx \frac{A}{Z}v = \frac{A}{Z}\frac{L}{T_{obj}}, \tag{4.1}$$

or $T_{obj} \propto \frac{A}{Z}$, which gives isotopic separation. Correlating the energy loss with the time of flight therefore uniquely identifies the nuclei that enter the S800 focal plane. Figure 4.2 shows the particle identification for this experiment with several nuclear species labeled, including ^{70}As. Software gates were again used to select only the nucleus under study.

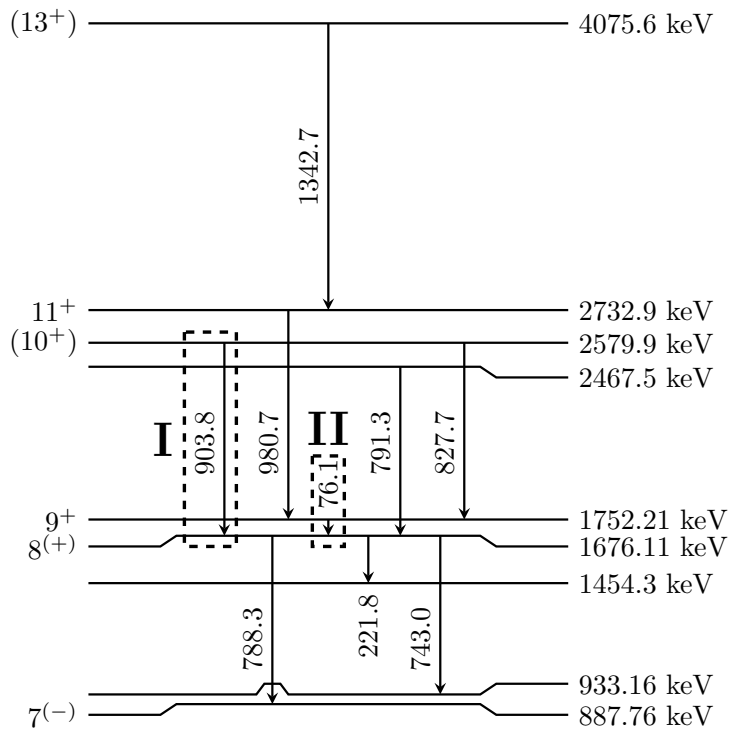

Figure 4.3: A partial level scheme for ^{70}As, showing the levels which are relevant to this study. Level energies are shown on the right, while spins and parities are shown on the left (parentheses indicate tentative assignments), and the arrows indicate transitions between levels of the associated energy. Two transitions are enclosed in boxes, indicating that these were used as gating transitions in the γ-γ analysis, described in detail in the text. Figure is from [64].

The deexcitation γ rays coming from the excited nuclei produced by reactions in the target were detected by SeGA in its barrel configuration (see Sec. 3.2.2.2). The lineshape method was used to extract the lifetimes of the states of interest in ^{70}As. To do so, γ-γ coincidence data were used, despite the large reduction in statistics that this imposes on the data. The reason for this is that the level scheme of ^{70}As is both dense and highly interconnected as illustrated by Fig. 4.3, which shows the portion of the excitation scheme of ^{70}As relevant to this study. As stated earlier, the two quantities of interest to this study are the 8^+ and 9^+ state lifetimes. However, inspection of Fig. 4.3 shows that multiple higher-lying states decay to both of these levels. This presents a problem because only some of

these higher-lying states have known lifetimes. If any of these states should have a lifetime which is comparable to or longer than the ones they feed, then the lifetimes of the 8^+ and 9^+ states measured here would be systematically higher than the true values. Therefore, gates were placed on the γ-ray spectra such that only photons coincident with a particular state with a sufficiently short lifetime were present in the spectra, thereby ensuring that feeding from long-lived states is removed.

To measure the 8^+ state lifetime, the $8^+ \rightarrow 7^-$ transition was analyzed in coincidence with a γ ray from the $10^+ \rightarrow 8^+$ transition. This transition was chosen because it was observed to be present in the experiment and, more importantly, there is good reason to expect that the 10^+ state has a short lifetime. Although the 10^+ state lifetime in ^{70}As is unknown, it is reasonable to expect that the $10^+ \rightarrow 8^+$ transition strength will be similar to that in the neighboring arsenic isotopes. Therefore, the 10^+ state lifetime in ^{70}As can be estimated based on the strength of the $10^+ \rightarrow 8^+$ transition in ^{72}As, which is known to be $B(E2; 10^+ \rightarrow 8^+) = 67$ W.u [78]. Under the assumption that the strength of this decay is identical in ^{70,72}As, this leads to an estimated lifetime of $\tau_{10^+} = 0.73$ ps, which is well below the sensitivity of this measurement and can be neglected. The possible impact of this estimation is discussed further in the discussion of the results of this measurement, Sec. 4.5. Therefore, analyzing the lineshape of the $8^+ \rightarrow 7^-$ transition when the 8^+ state is fed by the 10^+ state should ensure that the lifetime determined from this measurement is free from feeding effects.

The 9^+ state was analyzed in a similar fashion to the 8^+ state by analyzing the lifetime of the 9^+ state in coincidence with a γ ray from another state. However, several of the experimental conditions made a direct measurement of the $9^+ \rightarrow 8^+$ decay lineshape difficult. As can be seen in the spectra in Sec. 4.3, the threshold of the SeGA detectors was set such

that the transition was just on the edge of the range of energies that could be detected, and below the threshold for the forward detectors. Since a portion of the photopeak then lies over the part of the spectrum which is rapidly decreasing at the threshold, the shape of the peak is no longer reliable because the background shape cannot be accurately characterized. It was also observed during the experiment that there was a strong background component at roughly the same energy as the 76.1-keV transition depopulating the 9^+ state. This corresponds to a photon from radiative electron capture (REC) [79, 80], which is the inverse process of the photoelectric effect in which the projectile nucleus captures an electron from the target and emits a photon. The photon energy in the beam frame is the sum of the electron K-shell binding energy E_b in the projectile and the kinetic energy of the electron in the beam frame:

$$E_{REC} = \left(\frac{1}{\sqrt{1-\beta^2}} - 1 \right) m_e c^2 + E_b. \tag{4.2}$$

Since REC can have a cross section as high as tens of barns (see Fig. 1 of Ref. [79]), there is a significant chance for this process to be due to the ^{78}Rb beam before it reacts to form ^{70}As, or to the reacted beam itself. Therefore, the upper bound of REC energies corresponds to ^{78}Rb as it enters the target (traveling at $\beta = 0.43$) and the lower bound to ^{70}As as it leaves the target ($\beta = 0.34$). E_b can be approximated by assuming that the binding energy is the same as a hydrogen-like atom of the appropriate species, so that the range of energies in which an REC photon can be emitted is between 47 keV and 74 keV in the projectile frame. Considering the $9^+ \rightarrow 8^+$ photon has an energy of 76.1 keV, it will not likely be possible to distinguish it from the REC photopeak. Therefore, instead of measuring the shape of the $9^+ \rightarrow 8^+$ transition, it was decided to use the photon depopulating the 9^+ state as a gating condition and evaluate its effect on the lineshape of another transition which the 9^+ state

feeds. The $8^+ \rightarrow 7^-$ transition was the natural choice since it had already been measured in this work. With a sufficiently long lifetime, the feeding from the 9^+ state would cause the 8^+ state to appear to have a longer lifetime than that measured in coincidence with the $10^+ \rightarrow 8^+$ transition. With the 8^+ state lifetime already measured, any remaining effect would then be attributable to the 9^+ state and allow its lifetime to be determined.

4.3 γ-ray spectra

With the identification in the previous section of the particles entering and exiting the target, the γ rays that were detected in SeGA could be filtered to select only those that were detected in coincidence with ^{78}Rb particles incident on the target and ^{70}As fragments exiting the target. This insures that only the γ rays coming from excited states in ^{70}As are present in the analysis, so that transitions from other nuclei do not influence the lifetime measurement. These γ-ray spectra will be discussed in this section, both the singles spectra (those on which the only condition placed is coincidence with the incoming and outgoing beams) and the coincidence spectra (those which are gated on the presence of a specific γ ray).

The singles γ-ray spectra for ^{70}As are shown in Fig. 4.4, split into forward and backward rings and corrected for Doppler shifting. While the singles spectra may be problematic for measuring lifetimes in the present case (for the reasons discussed in Sec. 4.2), they have the highest statistics and are therefore useful for the purpose of identifying the various γ rays present. It is also important to inspect the singles spectra carefully before deciding upon the conditions for generating the coincidence spectra, as it is important to choose a gating condition which maximizes the number of true events in the gate while excluding as many

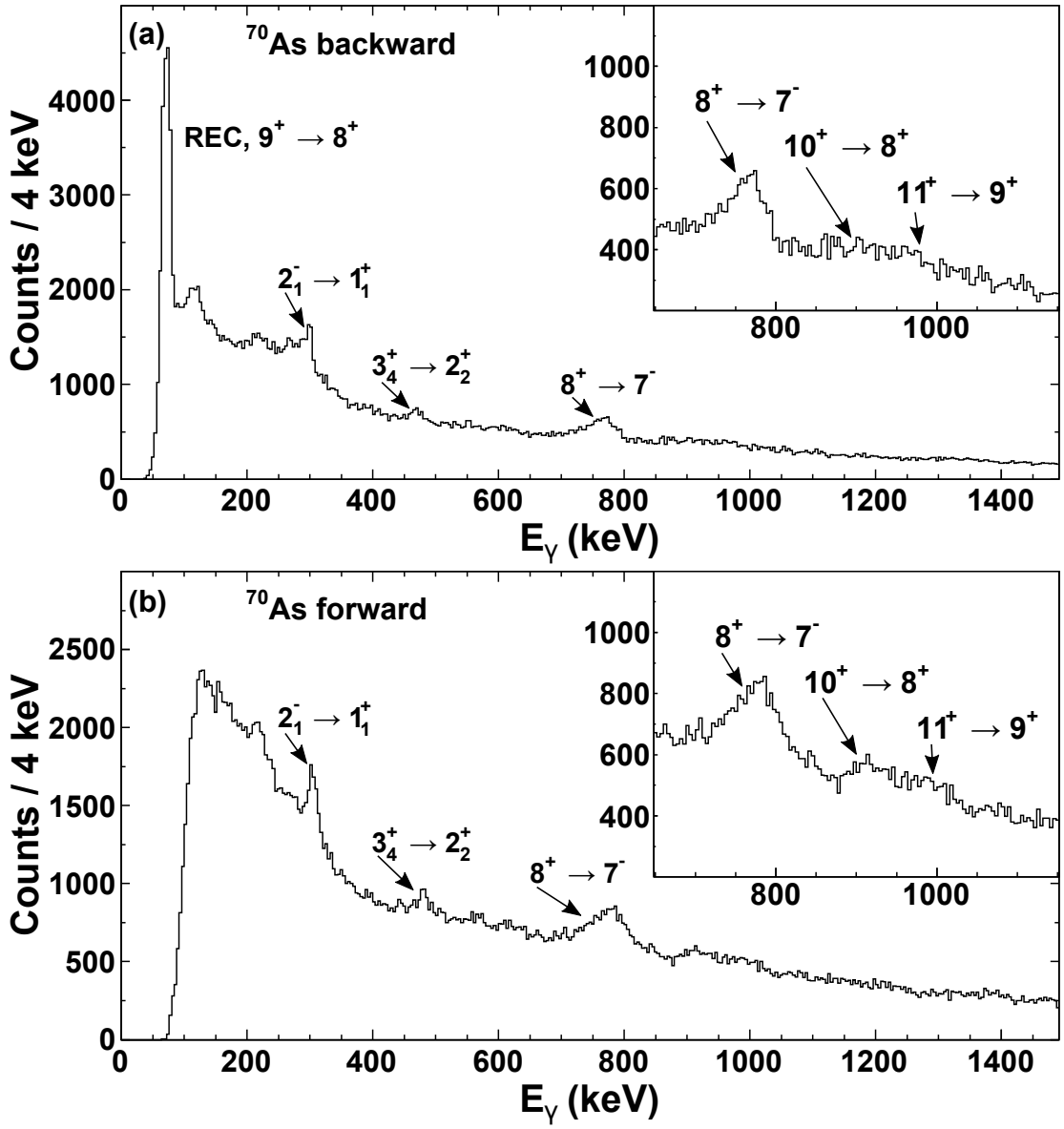

Figure 4.4: The γ-ray singles spectrum in coincidence with ^{70}As fragments detected in the S800, with panel (a) showing the γ rays detected in the backward ring and (b) those detected in the forward ring. Several prominent transitions are identified by arrows, including the $8^+ \rightarrow 7^-$ at 788.3 keV which has a noticeable asymmetry due to lifetime effects. The strong peak at low energy in the backward ring is due to both the $9^+ \rightarrow 8^+$ transition and the REC process described in Sec. 4.2, which cannot be resolved in this experiment. As mentioned, REC can have a very large cross section, which explains the large amplitude of this peak. In each panel, the inset shows the same spectrum focused around the 788.3-keV γ ray from the 8^+ state as well as weakly populated γ rays from the 10^+ and 11^+ states, which were important for choosing the coincidence gates. Figure is modified from [64].

accidental coincidences as possible. Inspection of Fig. 4.4 shows several places where clear peaks are present in the γ-ray spectrum, including the $8^+ \rightarrow 7^-$ peak and the peak which is a combination of the REC process mentioned earlier and the $9^+ \rightarrow 8^+$ transition. The insets to the figures show the peak from the 8^+ state along with two transitions from the 10^+ and 11^+ states, which are only weakly populated. These states feed the 8^+ and 9^+ states, which demonstrates the necessity of using γ-γ coincidence.

The coincidence spectra were generated by requiring that a γ ray within a given energy range corresponding to a particular transition be present and then plotting all other γ rays that were detected in the same event. The determination of the coincidence condition for the 9^+ state lifetime measurement was straightforward, as the peak from the 9^+ state lay within the large peak at low energy in the backward ring singles spectrum. Therefore, the condition for plotting γ rays for the coincidence spectrum was that a photon was detected in the range covered by this combination of the $9^+ \rightarrow 8^+$ and REC peaks in the backward ring. This gating condition can include events where REC satisfies the gating condition and creates false coincidence. However, since REC is an atomic process and not related to the nuclear states, it is completely uncorrelated with any nuclear transition and should contribute only a random background. The resulting γ-ray spectra are shown in Fig. 4.5, where the upstream and downstream rings have once again been plotted separately. Several transitions besides the $8^+ \rightarrow 7^-$ have been tentatively identified in this figure, but they are not related to the transition in question. In addition, it can be seen that the backward ring of detectors suffers from poor statistics and the shape of the $8^+ \rightarrow 7^-$ peak is not well-defined. Because of this, the backward ring was not able to be fit reliably and was excluded from the analysis and the lifetime was extracted from the forward detectors only.

The placement of the gate for generating the spectra for measuring the 8^+ state lifetime

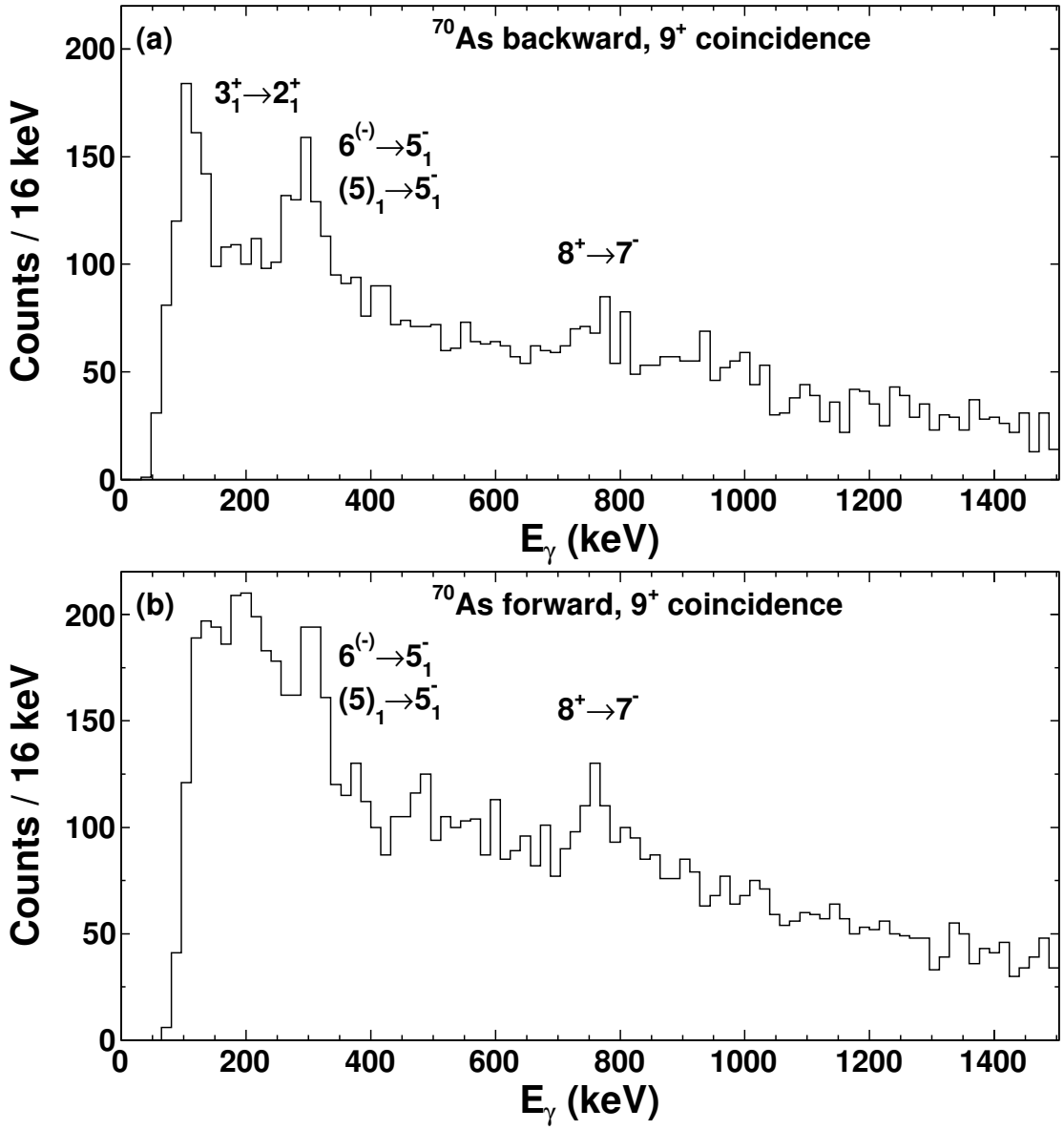

Figure 4.5: The coincidence γ-ray spectra for the lifetime measurement of the 9^+ state in ^{70}As, Doppler corrected and split into (a) the backward ring and (b) the forward ring. The gating condition is that there is a photon within the energy range covered by the combined REC and $9^+ \rightarrow 8^+$ transition peak. Several decays are labeled that can come in the coincidence gate but are not related to the decay of the 9^+ state. As can be seen in the figure, due to poor statistics the shape of the $8^+ \rightarrow 7^-$ peak is not well-defined in the backward ring and was not able to be fit reliably. For this reason, only the forward ring was used for analysis.

was more difficult to determine due to the much lower statistics in the $10^+ \rightarrow 8^+$ transition at 903.8 keV. In the end, the placement of the gates was chosen to require either a photon with an energy between 878 keV and 938 keV in the forward ring or a photon with an energy between 886 keV and 920 keV in the backward ring, as this was observed to give the best signal-to-noise ratio for the $8^+ \rightarrow 7^-$ transition. This choice was also validated later by comparing to the simulated peak shape for the $10^+ \rightarrow 8^+$ transition (see Sec. 4.5). The resulting γ-ray spectra are shown in Fig. 4.6, again split into forward and backward detectors. As with the coincidence spectra for the 9^+ state, the backward ring spectrum has very low statistics for the $8^+ \rightarrow 7^-$ transition, which does not have a clear shape for the peak. Therefore, as for the analysis of the 9^+ state lifetime, only the forward ring of detectors were used to analyze the lifetime of the 8^+ state.

Finally, given that the signal-to-noise ratio is not very high in the singles spectra, it can be asked whether the signal for the $8^+ \rightarrow 7^-$ transition observed in the coincidence spectra is due to true coincidence or accidental coincidence with background events. To evaluate the false coincidence rate, spectra were generated with gates beside the true gates that were specifically placed in locations where no coincidence with the 788.3-keV γ ray from the 8^+ state is expected. If a signal is observed in these spectra at 788.3 keV, then this will correspond to the accidental coincidence rate and can be used to determine whether it will be significant. These false-coincidence spectra are shown in Fig. 4.7, with the dots corresponding to the true coincidence data and the cross marks corresponding to the false coincidence data. In panel (a), the coincidence spectra for the 8^+ lifetime measurement are shown, and it is clear that while the background in both spectra are comparable, there is only a signal present in true coincidence data. The background spectra were generated by putting a gate on the energy spectrum around 1400 keV, with the same width as the gate on

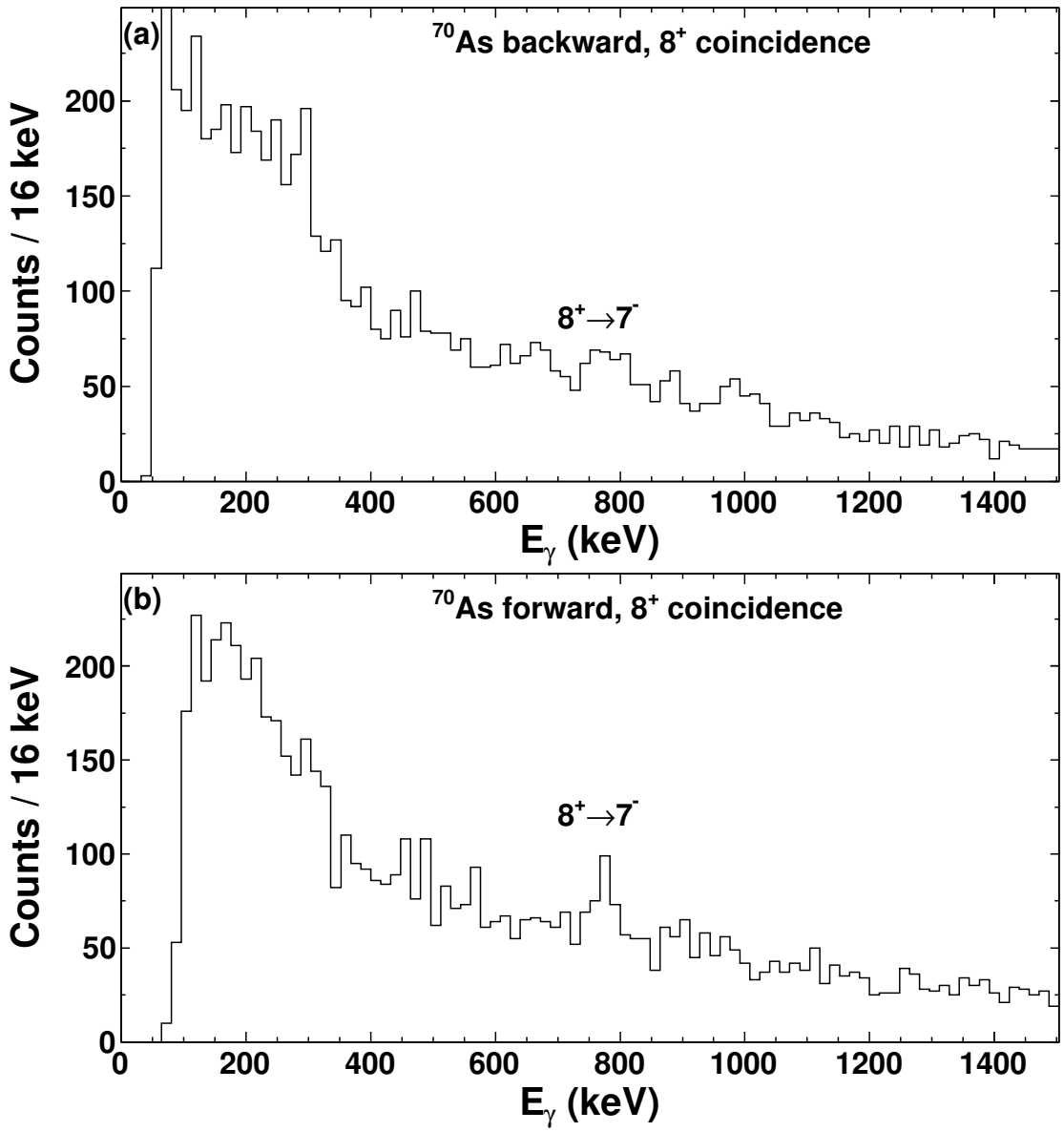

Figure 4.6: The coincidence spectra used to determine the 8^+ state lifetime in ^{70}As, split by photons detected in (a) the backward ring detectors and (b) the forward ring detectors. In contrast to the coincidence spectra for the 9^+ state lifetime, there are no other obvious transitions observed. The one bin which goes beyond the y-axis range in panel (a) is due to accidental coincidence from REC which is not important in this figure and had a bin content of 451 counts, and so the axis range was set to emphasize the rest of the spectrum. The $8^+ \rightarrow 7^-$ transition is labeled, and as for the 9^+ coincidence spectra, the peak shape is only well-defined in the forward detectors, and so the backward ring was not used in the lifetime analysis of the 8^+ state either.

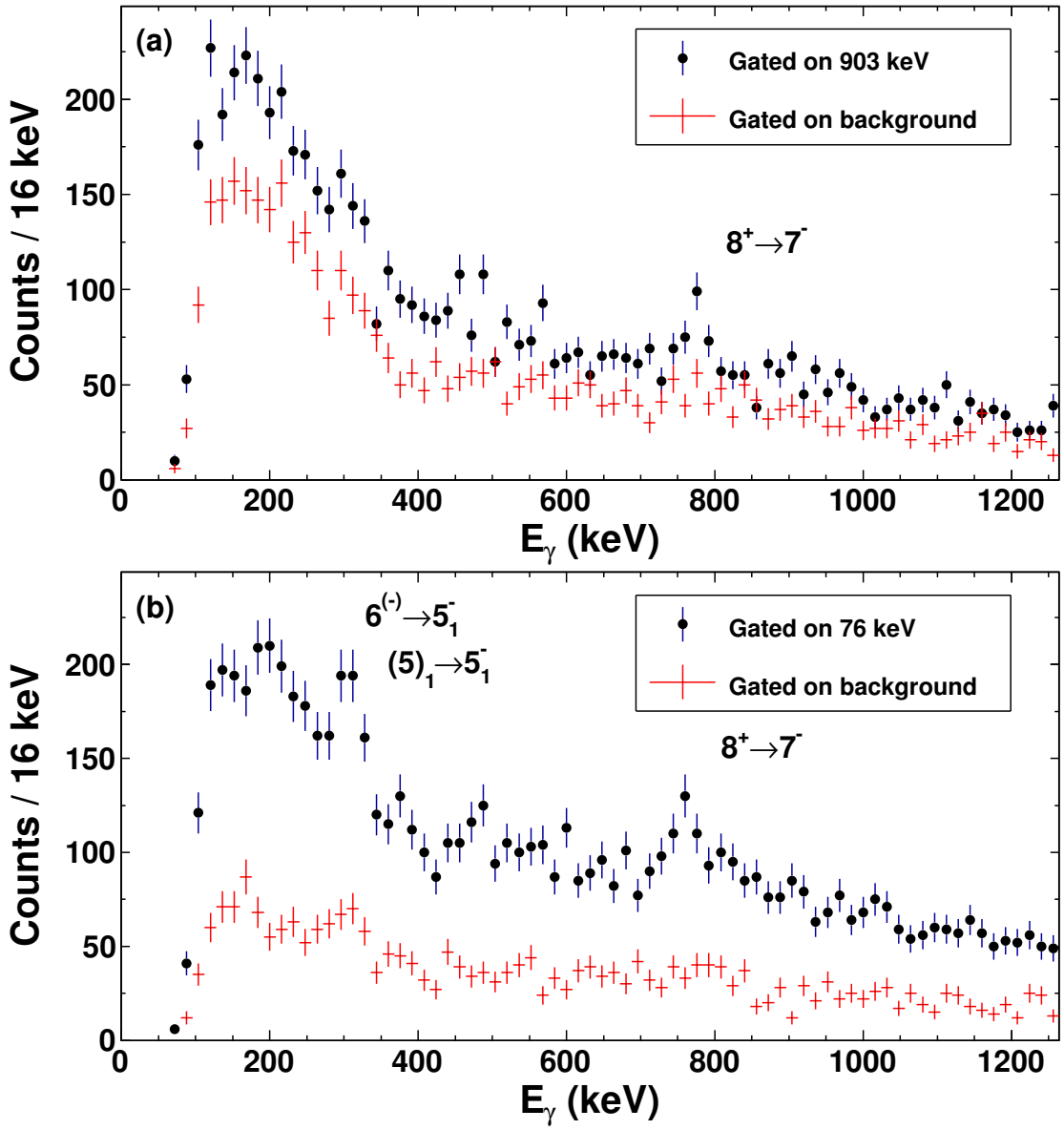

Figure 4.7: A comparison of the true coincidence rate with the background coincidence rate for (a) the $10^+ \rightarrow 8^+$ coincidence spectrum for the 8^+ lifetime analysis and (b) the $9^+ \rightarrow 8^+$ coincidence spectrum for the 9^+ state lifetime analysis. In both panels, the dots represent the true coincidence spectrum and the crosses represent the coincidence with background, and only data from the forward ring are shown. For both cases, the true coincidences show a clear presence of the $8^+ \rightarrow 7^-$ transition while the accidental coincidence spectra do not exhibit a signal from this transition. Figure is adapted from [64].

the true coincidence spectrum. A gate closer to the actual energy would have been used, but several transitions that feed the 8^+ state surround the $10^+ \rightarrow 8^+$ transition (see Fig. 4.3), and so a gate at higher energy had to be chosen to evaluate the accidental coincidences. Panel (b) shows a similar comparison for the 9^+ state lifetime analysis, and once again only the true coincidence spectrum shows a signal from the $8^+ \rightarrow 7^-$ transition, as well as a peak from other transitions as in Fig. 4.5. This false coincidence gate was set just above the true coincidence gate to try to use background as similar as possible to the true coincidence gate, and also shows no signal near the 788.3-keV γ ray from the 8^+ state. This shows that the gates used for this analysis do in fact select events which are in true coincidence with the $8^+ \rightarrow 7^-$ transition, as opposed to being in coincidence with the background. Normally, the background spectra would be subtracted from the true coincidence spectra in order to have a cleaner signal, however, it is usual to subtract a background spectrum which is an average of background gated just above and just below the transition of interest to try to minimize the impact of choosing any particular location to characterize the background. In this case, since the background in panel (a) was taken at significantly higher energies, and that in panel (b) could not be taken below the peak due to the threshold settings, no background subtraction was performed, and the background spectra are presented to demonstrate the quality of the gates.

4.4 Lifetime analysis

With the γ-ray spectra generated, the analysis of the lifetime of the 8^+ and 9^+ states could be performed. This was done by using Geant4 simulations (see Sec. 3.3) to reproduce the experimental γ-ray spectrum under the assumption of a range of different lifetimes for the

state being studied, and then fitting these simulated spectra to the real ones. In doing so, a reduced χ^2 distribution was generated as a function of the lifetime, and the minimum of this function was taken to be the lifetime. For this dataset, since coincidence data were used to determine the lifetimes, simulated coincidence spectra were also generated for use in the fitting procedure. The remainder of this section will describe the preparation of these simulations and the data analysis itself.

4.4.1 Geant4 simulations

In order to accurately reproduce experimental γ-ray spectra, it is important for the Geant4 simulations to mimic as much as possible the conditions under which the experiment was performed. The first step towards reproducing the experiment is to ensure that the placement of the SeGA detectors in the simulation corresponds to the placement of the physical detectors. While the geometry of the barrel configuration of SeGA is largely set by the detector mounting frame, there is some room for adjustment of the detectors. To determine the detector locations as accurately as possible, a device known as a "ROMER arm" is used. This device is an armature with a pressure-sensitive probe attached to the end. As the armature is moved, the device tracks the location of the probe in space and records the coordinates of the probe each time it is pressed against a surface. Known points on the SeGA detectors are then touched by the probe to record their coordinates, and the location of the ROMER arm is determined against well-known calibration locations in the lab by laser survey. These coordinates are then used to generate the simulated SeGA detectors so that their locations are the same as those used in the experiment.

With the geometry fixed, the next thing to be validated is the γ-ray detection efficiency of the simulation as a function of photon energy. This is important because the detector

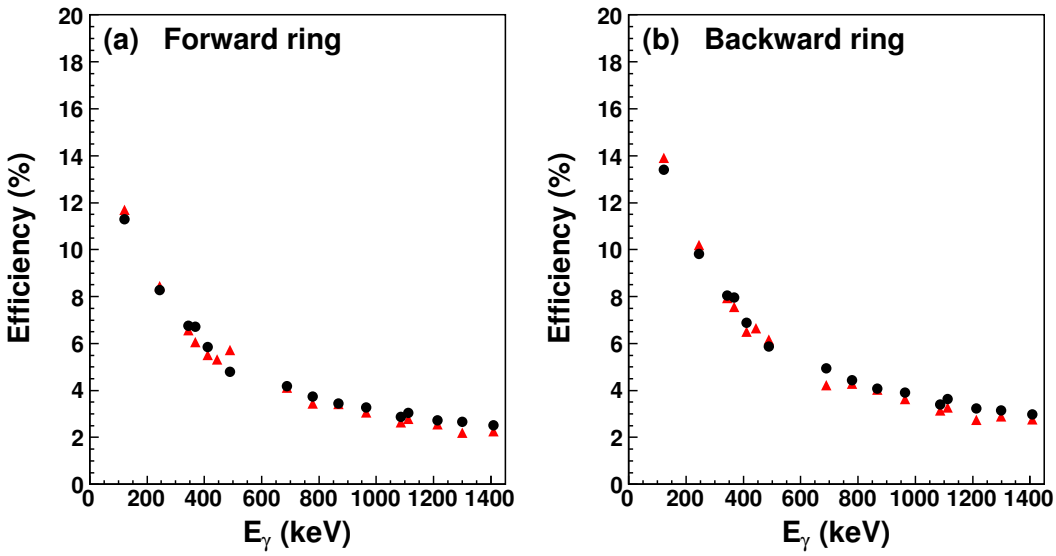

Figure 4.8: Comparison of the simulated and measured efficiency of SeGA for various γ-ray energies with a ^{152}Eu source in (a) the forward ring and (b) the backward ring. In both panels, the simulation is shown by the red triangles while the data is shown by the black dots. The simulations reproduce well the efficiency of the real SeGA detectors, especially in the $\sim$600-1000 keV energy range of interest to this experiment.

efficiency is intimately connected with the photopeak shape. If the simulation were to have a detection efficiency with a much greater slope as a function of energy than the real detectors, it would lead to an exaggerated low-energy tail and thus produce erroneous lifetime results. The efficiency can be checked by taking data with a standard radioactive calibration source with known activity and γ-ray branching ratios and comparing it to the corresponding spectrum generated by the simulation. The efficiency curve for a ^{152}Eu source is shown in Fig. 4.8, divided into the forward and backward rings. The red triangles represent the data while the black dots represent the simulations. The overall shape of the efficiency curve for the data is reproduced very well by the simulations, especially for the energy range between about 600 keV and 1000 keV which is relevant for this analysis. While some small deviation between the data and simulations may be present, this is ultimately inconsequential, as the simulations are scaled to match the data in the analysis and this will effectively normalize

the simulated efficiency. What is important is that the relative efficiency at various energies remains constant between the simulation and the data. This figure aptly demonstrates that this is the case.

With the performance and placement of the SeGA detectors determined, the properties of the beam in the experiment need to be input into the simulation. In particular, it is important to fix the physical size and direction of the beam as well as its energy, because the simulation attempts to apply the same Doppler correction to photons that it generates as is applied to the γ rays detected in the experiment. Since the real beam is tracked in the S800 and its reconstructed trajectory at the target used for the Doppler correction, this same condition needs to be recreated in the simulation as well. This was done by providing the focus point of the incoming ^{78}Rb beam as well as its spatial and angular spread in the dispersive and non-dispersive directions. The energy of the incoming beam and the energy spread as measured in the experiment are also provided. The reaction mechanism is input as the change in the number of protons and neutrons, and the momentum change of the beam is described by a loss of longitudinal momentum according to a Gaussian distribution with an adjustable width, plus a kick of adjustable strength in a random direction. The target thickness and density are also provided, and the simulation uses this information to calculate the energy loss of the ion through the target (see Sec. 3.3). The kinetic energy of the beam corresponding to the $B\rho$ setting of the S800 is provided as well as the acceptance of the spectrograph so that the acceptance of the simulation is similar to what is actually observed. In the end, the simulation outputs the distributions of the angles in the dispersive and non-dispersive direction (a_{ta} and b_{ta}, respectively), the non-dispersive position (y_{ta}), and the spread in the energy $\Delta E/E$ (d_{ta}). Figure 4.9 shows a comparison between the experimental (black) and simulated (red) properties of the beam. All of the simulated spectra reproduce

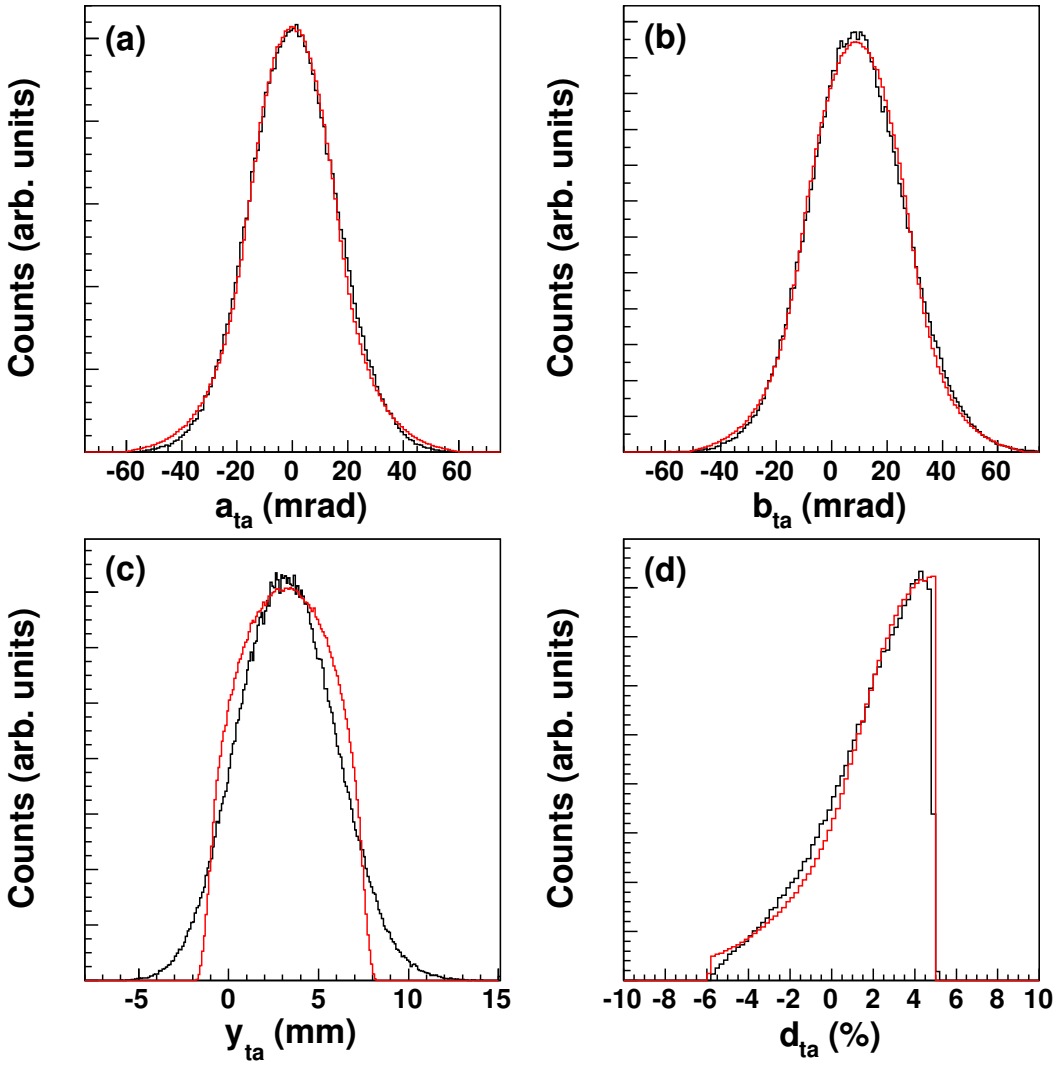

Figure 4.9: A comparison of the measured beam profile (black) with the simulated one (red). Panels (a) and (b) show the spread in the angular divergence of the beam in the dispersive and non-dispersive directions, respectively. Panel (c) shows the spatial distribution in the non-dispersive direction, and panel (d) shows the spread in the energy of the beam relative to the energy specified by the $B\rho$ of the S800. All the distributions show very good agreement with the exception of y_{ta}, where the simulation does not reproduce the tails of the data. However, the position in the non-dispersive direction does not strongly affect the γ-ray spectrum, and so this level of agreement is sufficient.

the data very well with the exception of the y_{ta}, which shows a marked deviation from the tails of the data. This is because the simulation assumes a uniform ellipsoidal beam, but in reality the beam may have any shape. However, the distribution of the beam in the non-dispersive direction does not have a strong effect on the γ-ray spectrum, and so instead of attempting to modify the simulation code to accommodate every experiment, the approximation of an ellipsoid is used and adjusted to the data as much as possible. The position in the dispersive direction is not measured, but is usually assumed to be zero in order to be consistent with the assumption made for the inverse tracking in the S800.

Finally, with the detector and beam properties constrained, the last inputs necessary to generate the simulated γ-ray spectra are the level scheme, decay energies, and lifetimes. For this work, the level and γ-decay energies were already determined in previous studies, and so these parameters were taken from the literature. The lifetime is to be determined here, and so this final parameter was varied in the simulations. The simulated spectra and the lifetimes determined from fitting them to the data are presented in the next section.

4.4.2 Lifetime determination

With the Geant4 simulations prepared, the lifetimes of the 8^+ and 9^+ states were determined by fitting the simulated γ-ray lineshapes to those observed. First, a preliminary fit with no feeding was performed on the singles spectrum in order to verify which transitions could be observed in the spectrum. Then, fits to the coincidence data were performed to determine the 8^+ and 9^+ state lifetimes. Finally, a fit to the singles data was performed with full feeding where both the 8^+ and 9^+ state lifetimes were varied simultaneously, and this was used to verify the results of the coincidence fit.

The first step in understanding the γ-ray spectra was to determine which transitions

could be observed and to have an estimate of their intensities. To do this, a preliminary investigation of the γ-ray singles spectrum in the range between roughly 600-1000 keV was performed by fitting γ-ray spectra for all of the transitions shown in Fig. 4.3 on top of an exponential background (excluding the 1342.7-keV, 76.1-keV, and 221.8-keV transitions, as these were outside of the initial fitting range chosen). A transition at 944.9 keV (not shown in Fig. 4.3) was also added in order to explain the counts observed at that energy, however, it is otherwise unrelated to the analysis. The results of this fit are shown in Fig. 4.10, where the upper panel shows the simulated γ-ray spectrum (red) fit to the data (black) in the forward ring and the lower panel shows the simulation broken up into its individual components. For this first fit, a lifetime of 150 ps for the 8^+ state was observed to give a reasonable reproduction of the experimental spectrum. However, it should be noted that feeding was ignored for this first attempt, and so this value should not be taken to be representative of the true 8^+ lifetime. What is important to see from this fit is that there are many γ rays present in the spectrum and that many of them are significantly overlapping each other. In particular, the 791.3-keV γ ray is completely unresolved from the 788.3 keV γ ray from the 8^+ state, which severely complicates the determination of the lifetime of the 8^+ state in the singles spectrum. The other point to notice about this fit is that it shows that the 903.8-keV transition from the 10^+ state is well-separated from the 827.7-keV and 980.7-keV transitions that feed the 8^+ state through the 9^+ state, which makes it ideal as a gating condition. It does have significant overlap with the 944.9-keV transition mentioned earlier, but as this is located below the 8^+ state and does not feed any of the states of interest to this analysis, it is inconsequential. This provides confirmation that the placement of the gate used to generate the 8^+ state coincidence spectrum is valid. The dashed vertical lines indicate the placement of the gate.

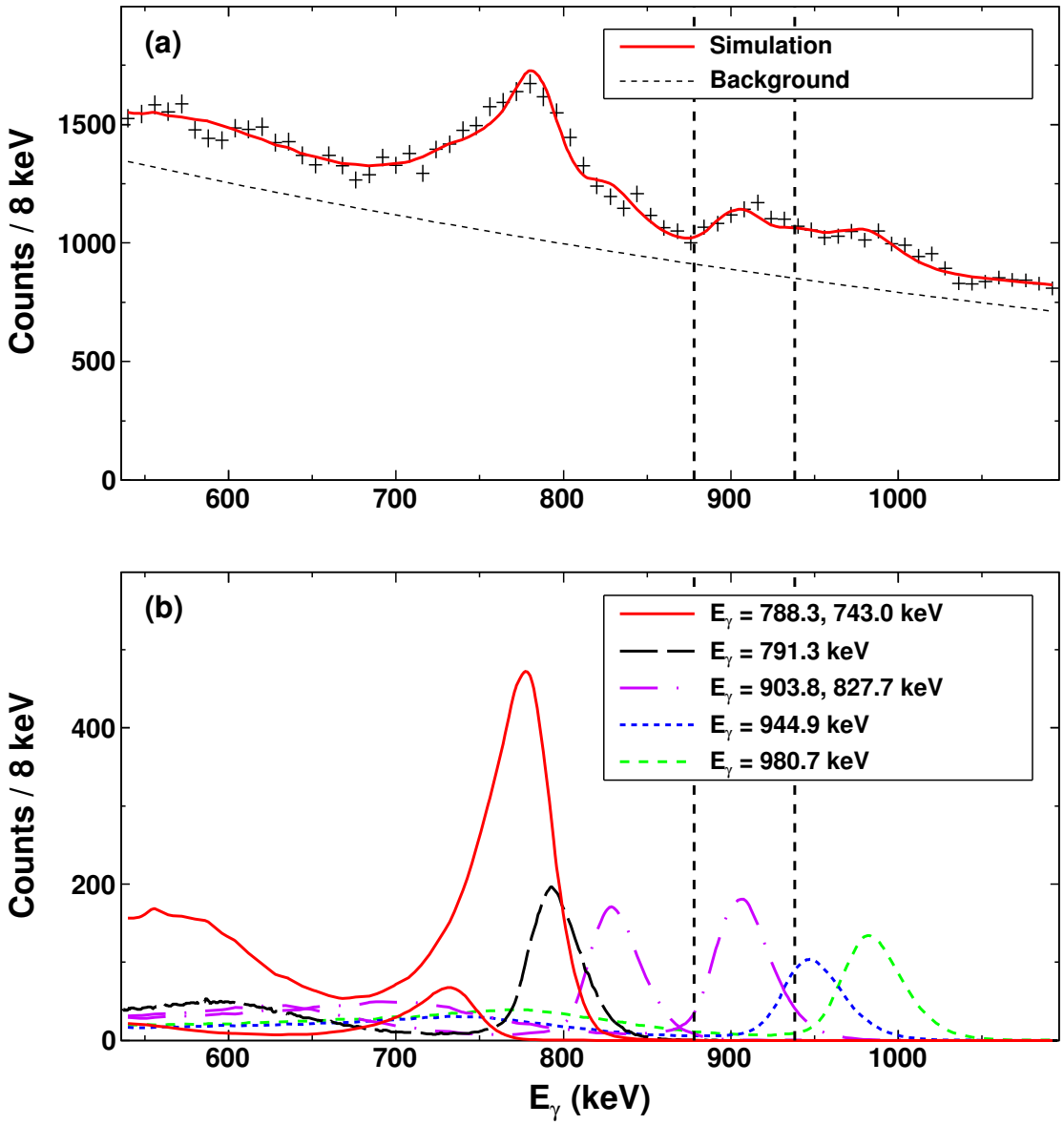

Figure 4.10: A first attempt at fitting the γ-ray singles spectrum from the forward ring. For this fit, no attempt was made to account for any feeding, and a lifetime for the 8^+ state of 150 ps was used. Panel (a) shows the data (black points with error bars) with the fit overlaid as the solid line in red. The assumed exponential background is shown by the dashed line. The individual components of this fit can be seen in panel (b). The legend identifies the various γ-ray energies, which correspond to those listed in Fig. 4.3 except for the 944.9-keV γ ray, which was included to explain the accumulation of counts at that energy. Otherwise, the 944.9-keV γ ray is unrelated to the analysis, as the state from which it originates lies below the 8^+ state. The vertical dashed lines denote the location of the gate used to generate the coincidence spectra for determining the 8^+ lifetime. Figure is from [64].

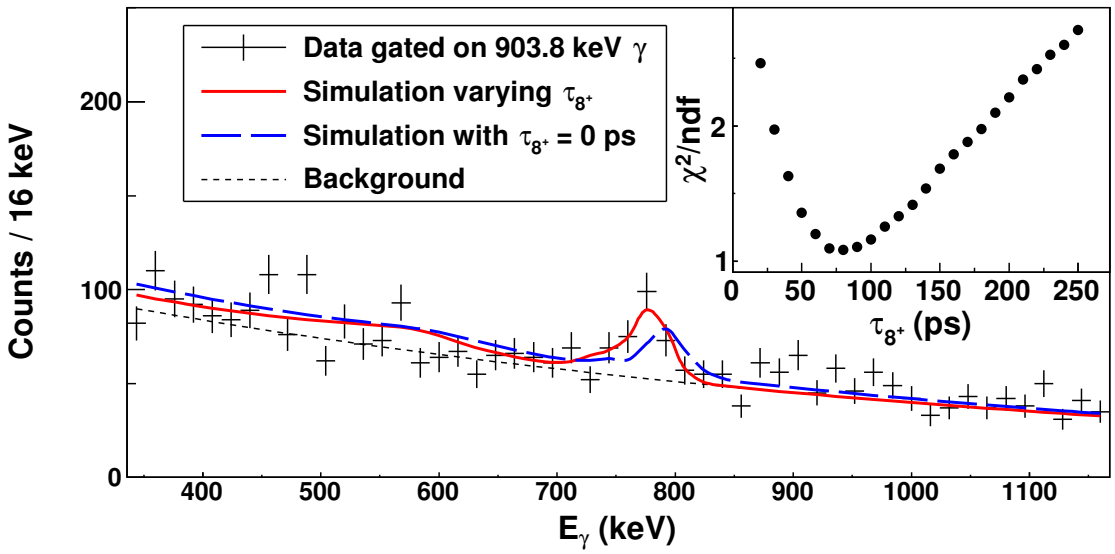

Figure 4.11: The results of fitting simulations of the 8^+ state with various lifetimes (red line) to the experimental data for the downstream ring in coincidence with the $10^+ \rightarrow 8^+$ transition (black points with error bars). The lifetime determined from the fit is $\tau_{8^+} = 80(28)$ ps, including only statistical uncertainties. Also shown is a simulation with a lifetime of 0 ps for the 8^+ state for comparison, which demonstrates the sensitivity of the data to the lifetime. The inset shows the reduced χ^2 distribution with five degrees of freedom, the minimum of which was used to determine the lifetime. Figure is from [64].

In order to determine the lifetime of the 8^+ state, simulations were fit to the coincidence spectrum for the forward detectors shown in Fig. 4.6(b). The simulations were generated with the lifetime varied in 10 ps steps, and each of these was fit to the data on top of an exponential background. The background was constrained by fitting on a region that included the $8^+ \rightarrow 7^-$ peak plus background on either side, then fixing the parameters of the exponential. The simulations were then fit to the data over a smaller region which included only the peak area, the results of which are shown in Fig. 4.11. For each simulation, the χ^2 value per degree of freedom was calculated and saved. The minimum of the distribution of reduced χ^2 values (shown in the inset of the figure) was then used to determine the 8^+ lifetime as $\tau_{8^+} = 80(28)$ ps. In the figure, the data are shown by the black points, the solid red line shows the simulation generated with a lifetime of 80 ps, and the blue dashed

line is a simulation with an 8^+ lifetime of 0 ps to show the sensitivity of the peak shape to the lifetime. The uncertainty of this measurement given in parentheses is only due to the statistical uncertainty of the fit. Systematic uncertainties were also evaluated and were mostly due to the assumptions associated with the background, including its shape and the region over which it was fit, which when varied produced a sensitivity of 6.4% of the measured lifetime value. Varying the position of the detectors relative to the target in the simulations produced a 3% variation in the results, consistent with the findings in [32] where the same setup was used. Finally, the assumption that the 10^+ state lifetime is 0.73 ps also introduces some uncertainty. To evaluate this effect, the lifetime of the 8^+ state was also evaluated under the assumption that the 10^+ state lifetime is five times longer (i.e. 3.65 ps, which would already indicate a substantial change in the structure of the 10^+ states between ^{70,72}As and can therefore be considered unlikely). In this case, the lifetime of the 8^+ state in ^{70}As is reduced by 3.4%. Added in quadrature and combined with the statistical uncertainty, this gives a final result for the 8^+ state lifetime of $\tau_{8^+} = 80(29)$ ps.

A similar approach was taken to determine the 9^+ state lifetime using the coincidence spectrum shown in Fig. 4.5(b). Simulations were generated with the 9^+ state decaying into the 8^+ state, and the 8^+ in turn decaying into the 7^- state. The lifetime of the 8^+ state was fixed to 80 ps as measured in this experiment, while the 9^+ state lifetime was varied in 10 ps increments. Since the 827.7-keV γ ray from the 10^+ state and the 980.7-keV γ ray from the 11^+ state can both be in coincidence with the $9^+ \rightarrow 8^+$ decay, simulations were also generated for these states and included in the fit. As with the 8^+ state lifetime analysis, the background as well as the amplitude of the peaks from the 10^+ and 11^+ states were fixed by fitting over a wide region including the 8^+ peak, then the simulations were fit to a region including only the peak itself and a reduced χ^2 distribution was generated.

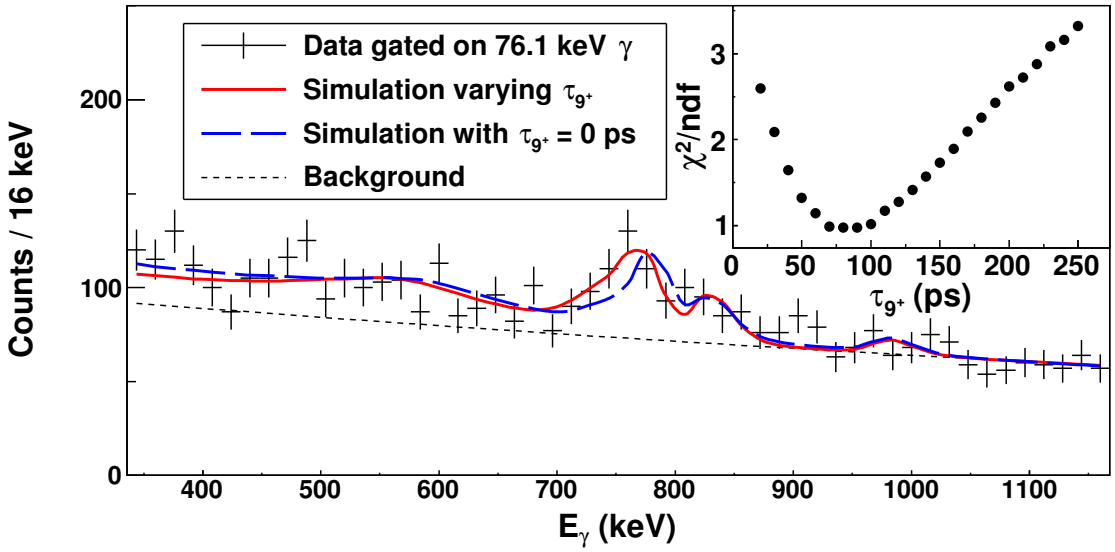

Figure 4.12: The results of fitting the coincidence spectra gated on the 9^+ state for ^{70}As. The simulation with the best fit lifetime of 85 ps is shown by the solid red line drawn over the black data points. As with the 8^+ lifetime analysis, a simulation with the 9^+ lifetime set to 0 ps is shown by the blue dashed line to show the sensitivity to the lifetime. The inset shows the reduced χ^2 distribution which was calculated with four degrees of freedom, the minimum of which was used to determine that the 9^+ state lifetime is $\tau_{9+} = 85(30)$ ps, including statistical uncertainties only. Figure is from [64].

The results of the fit are shown in Fig. 4.12. From the χ^2 distribution, the lifetime was found to be $\tau_{9+} = 85(30)$ ps, where the uncertainty is again only statistical. The sources of systematic uncertainty were similar to that for the 8^+ state lifetime analysis, with the background constraint contributing 9.4% to the uncertainty, the same 3% uncertainty due to detector placement, and the assumption of the 10^+ state lifetime gives an additional uncertainty of 4.4%. Since the lifetime of the 8^+ state was used in the determination of the 9^+ state, its uncertainty was also propagated to the 9^+ state lifetime result. Combined in quadrature, these extra sources of uncertainty give a final result for the 9^+ state lifetime of $\tau_{9+} = 85(43)$ ps.

As a check that the lifetime measured for the 9^+ state is not from differences in the lineshape due to other features of the spectrum, for example the shape of the background, a

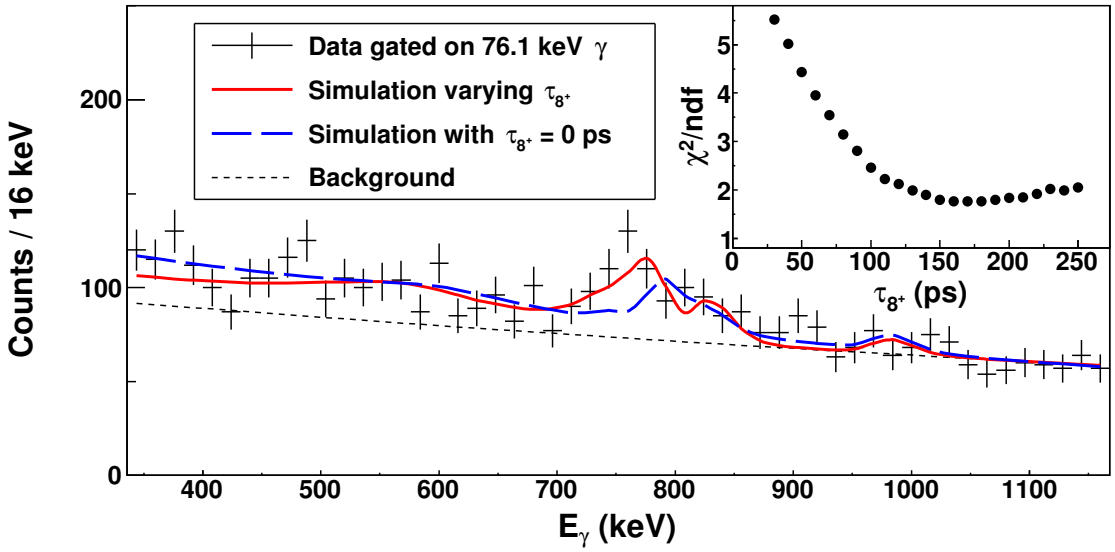

Figure 4.13: A fit to the 9^+ coincidence data using simulations which do not include the feeding from the 9^+ state. This fit should be poor if the measured lifetime is truly due to the 9^+ state. Inspecting the spectrum, it can be seen that the shape of the photopeak is not reproduced by the simulations under these conditions, which indicates that the 9^+ state lifetime has a significant effect on the 8^+ lineshape. The reduced χ^2 distribution in the inset, which was calculated using four degrees of freedom as in Fig. 4.12, does not show a sharp minimum as in Fig. 4.12 nor is it consistent with the result for the 8^+ state lifetime in Fig. 4.11. This indicates that the 8^+ state lifetime alone cannot explain the lineshape of the peak under these gating conditions. Figure is from [64].

set of simulations without feeding from the 9^+ state was generated and fit to the coincidence data gated on the 9^+ state. The results of this fit are shown in Fig. 4.13. Under these conditions, the shape of the $8^+ \rightarrow 7^-$ transition cannot be adequately reproduced for any lifetime of the 8^+ state. In addition, the reduced χ^2 value is considerably worse than the fit including feeding from the 9^+ state. This indicates that the measured lifetime is in fact attributable to the 9^+ state.

As a final check for consistency, the 8^+ and 9^+ lifetimes were analyzed by varying them simultaneously in the simulations and fitting the resulting spectra to the γ-ray singles spectrum. The full feeding of every level to the 8^+ and 9^+ levels was implemented for this fit to ensure full consistency. The result of this fitting procedure is shown in Fig. 4.14, where

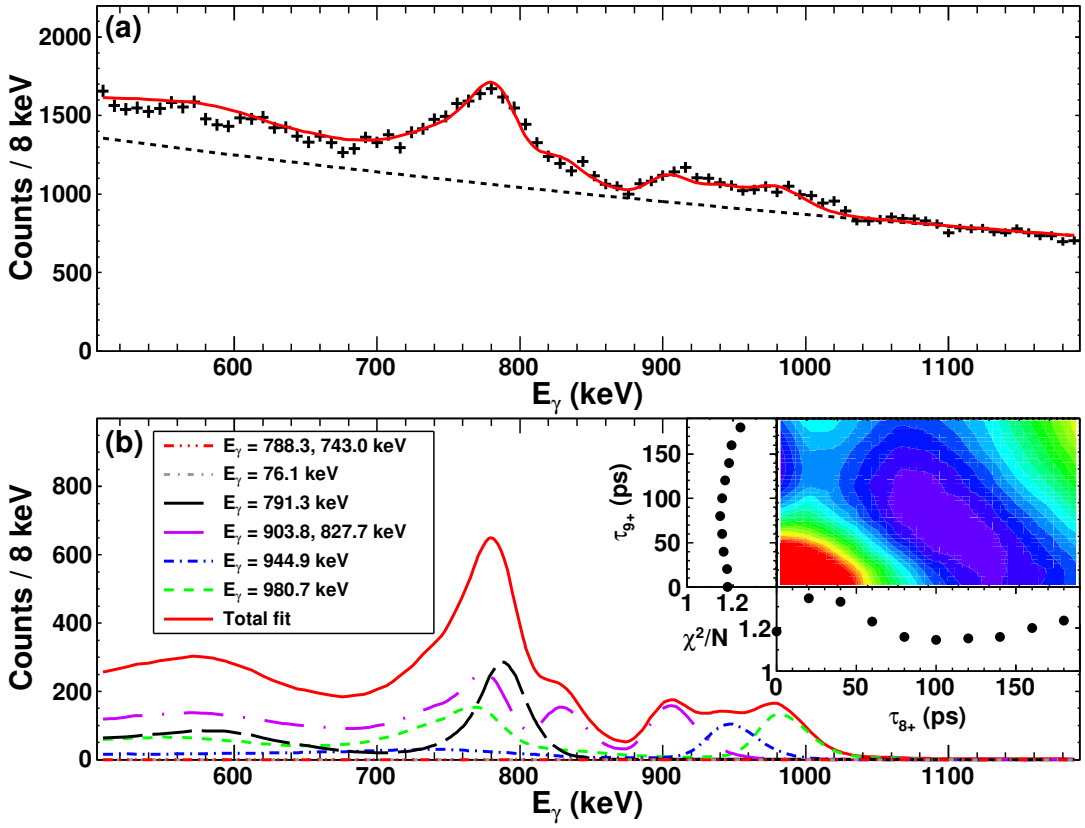

Figure 4.14: The results of a fit in which both the 8^+ and 9^+ state lifetimes are varied simultaneously. Panel (a) shows the resulting fit to the data, while panel (b) shows the individual simulations involved in the fit. Also shown in the inset to panel (b) is the 2-dimensional reduced χ^2 surface along with its projection onto the axes for the 8^+ and 9^+ state lifetimes. The minimum value is $\chi^2/N \approx 1.15$ at $\tau_{8+} \approx 100$ ps and $\tau_{9+} \approx 80$ ps, in agreement with the coincidence fits. The number of degrees of freedom for this fit is 58, which reflects the fact the fit is over a much wider energy range. For reference, the maximum value given by the red color in this contour plot is $\chi^2/N = 2$. Figure is adapted from [64].

the top panel shows the summed simulations (red line) overlayed on the data points for the downstream ring of detectors as well as the exponential background (dashed line). As shown in the inset to panel (b), a 2-dimensional χ^2 surface was generated from these fits and the projection of this surface onto the 8^+ and 9^+ χ^2 axes are also shown. Two minima can be seen in the inset, one at $\tau_{8+} \approx 0$ ps and $\tau_{9+} \approx 160$ ps, and another at $\tau_{8+} \approx 100$ ps and $\tau_{9+} \approx 80$ ps. The coincidence fits clearly exclude the possibility of $\tau_{8+} = 0$ ps, but the other minimum is fully consistent with the conclusions drawn from the coincidence fits and serves

as a validation of these results.

4.5 Results and discussion

In order to interpret the results of the measurements reported in this chapter, the lifetimes of the 8^+ and 9^+ states should be converted into reduced transition strengths. The transition strengths contain the nuclear structure information of the states involved in a transition and therefore they are useful for understanding the results of a measurement and comparing to the structure of nearby nuclei. For the 8^+ state, the decay that was measured has a primarily $E1$ character with a small $M2$ admixture ($\delta = 0.017(13)$) [73]. Knowing this, the transition strength can be calculated to be $B(E1) = 1.3(5) \times 10^{-5}\ e^2\text{fm}^2$. In single-particle units, this corresponds to $1.2(4)\times10^{-5}$ W.u. The $9^+ \rightarrow 8^+$ transition, on the other hand, has an $M1$ character with a small $E2$ admixture ($\delta = 0.01(3)$) [73], and so the transition strength is $B(M1) = 1.5(8)\ \mu_N^2$, or 0.85(42) W.u. These results can now be used to provide insight into the nature of the 8^+ and 9^+ states, and specifically whether they can be described by a $\pi g_{9/2}\nu g_{9/2}$ configuration.

As discussed in Sec. 4.1, if the 8^+ state has a $\pi g_{9/2}\nu g_{9/2}$ configuration, then it is to be expected that the $8^+ \rightarrow 7^-$ transition is strongly hindered. As explained, there is good reason to believe that the 7^- state has a $\pi f_{5/2}\nu g_{9/2}$ main configuration, and so these two states cannot be connected by an electric dipole transition since the proton must change its angular momentum by $2\hbar$ between the $f_{5/2}$ and $g_{9/2}$ orbitals. Therefore, if the transition proceeds it must be through small admixtures of other minor configurations (e.g. excitations of the core) which are allowed, and therefore the overall strength must be very hindered. To gauge the hindrance of this decay, it is helpful to compare its strength to that of other

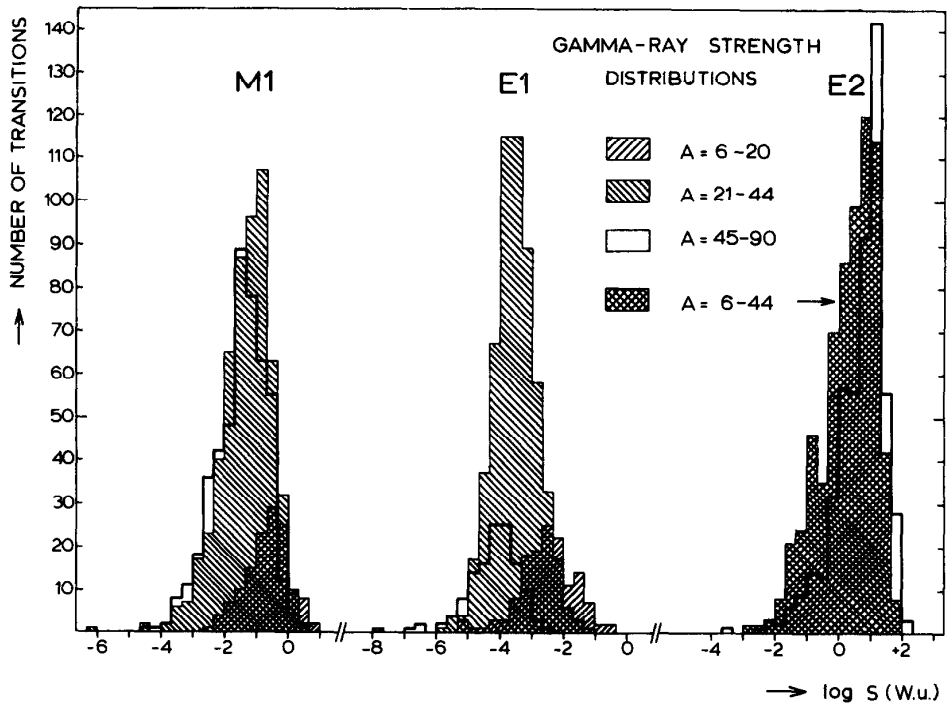

Figure 4.15: A diagram showing the distribution of transition strengths for several types of electromagnetic transitions, divided into several different mass regions [77]. The central set of distributions is for $E1$ transitions, and unfilled histogram is the relevant one for ^{70}As. This histogram includes transition strengths in the range from roughly 10^{-6} to 10^{-2} W.u. With a strength of $B(E1; 8^+ \rightarrow 7^-) = 1.2(4) \times 10^{-5}$ W.u., it is clear that this transition in ^{70}As is relatively hindered.

$E1$ transitions in this mass region. Figure 4.15 shows a figure taken from Ref. [77] which contains several histograms for different transitions in different areas of the nuclear chart. Of interest for the present discussion is the unfilled area of the central collection of histograms in this figure, which corresponds to $E1$ transitions in the mass $A = 45 - 90$ region. Inspection of this distribution shows that the $B(E1; 8^+ \rightarrow 7^-)$ value measured in this work is indeed on low end of this distribution, indicating that it is a hindered transition. This supports the assignment of the 8^+ state to the $\pi g_{9/2} \nu g_{9/2}$ configuration.

A more direct method of evaluating the configuration of the 8^+ state in ^{70}As was also mentioned in Sec. 4.1, which was comparison with the strength of the $8^+ \rightarrow 7^-$ transition

in the neighboring isotope ^{72}As. In this nucleus, it has been established already that the 8^+ state is a member of the $\pi g_{9/2}\nu g_{9/2}$ configuration, and this state also has a decay to a 7^- level with a $\pi f_{5/2}\nu g_{9/2}$ configuration, just as is believed to be the case in ^{70}As. As mentioned at the beginning of this chapter, this decay has a known strength of $B(E1) = 1.22(16) \times 10^{-5}$ W.u. The measurement of the $8^+ \rightarrow 7^-$ strength in ^{70}As in this work of $B(E1) = 1.2(4) \times 10^{-5}$ W.u. is fully consistent with that measured in ^{72}As. Since it can be expected that neighboring isotopes have similar structure, this is another indication that the 8^+ state in ^{70}As does in fact belong to the $\pi g_{9/2}\nu g_{9/2}$ multiplet of states.

Evaluating the structure of the 9^+ state relied upon interpreting the $M1$ strength of the transition between the 9^+ and 8^+ states. In Sec. 4.1, it was predicted that if the 9^+ state belongs to the $\pi g_{9/2}\nu g_{9/2}$ configuration (along with the 8^+ state), then the strength of the transition should be about 1 W.u. in terms of order of magnitude because only the last odd nucleons should be participating in the transition. Indeed, the strength that was measured was 0.85(42) W.u., which is consistent with this interpretation. However, a more quantitative prediction can be made by employing a simple model calculation for the $M1$ strength. For this purpose, a model was chosen that has been used to describe ^{70}As previously [70], specifically its lower-lying states. The model itself describes the nucleus as composed of two quasiparticles (a quasiproton and a quasineutron) coupled to an even-even core which has a vibrational character [81]. This model is a convenient choice, because it allows the $M1$ strength of a transition between two states in the same quasiparticle multiplet to be calculated analytically with the equation [81]

$$B(M1; I_i \rightarrow I_f) = \frac{3(j_p + j_n + I_i + 1)(j_p - j_n + I_i)(-j_p + j_n + I_i)(j_p + j_n - I_i + 1)}{4\pi I_i(2I_i + 1)} \times \left(\frac{\mu_p}{2j_p} - \frac{\mu_n}{2j_n}\right)^2, \tag{4.3}$$

where in this expression I_k represents the spin of the nuclear state k, $j_{p,n}$ the angular momentum of the proton and neutron, respectively, and $\mu_{p,n}$ the magnetic moment of the proton and neutron, respectively. It is important to note that this expression assumes that the initial state is the higher spin state, and if it is not then all I_i must become I_f in the numerator of Eq. 4.3. In Ref. [81], the term in the magnetic moments is evaluated by assuming a quenching of the spin-g factor for free nucleons of 0.6, such that

$$\frac{\mu_p}{2j_p} - \frac{\mu_n}{2j_n} = \frac{1}{2}\left\{1 + \frac{2.35}{2l_p+1} + \frac{2.29}{2l_n+1}\right\}\mu_N. \tag{4.4}$$

With this, and inserting $j_p = j_n = \frac{9}{2}$ and $I_i = 9$, this model gives a predicted $M1$ strength for the $9^+ \rightarrow 8^+$ transition of $B(M1) = 1.2\ \mu_N^2$, or equivalently 0.69 W.u. This is very much in line with the original prediction of $\sim$1 W.u. transition strength, and also consistent with the measured strength of 0.85(42) W.u. This model therefore supports the assignment of the 9^+ state to the $\pi g_{9/2}\nu g_{9/2}$ multiplet.

The consistency of the strength of the $9^+ \rightarrow 8^+$ transition in ^{70}As with other nuclei in the region can also be evaluated, similar to the manner done with the 8^+ state. While there is no $9^+ \rightarrow 8^+$ transition with measured strength in the neighboring arsenic isotopes, isotopes of other nearby elements do have such transitions with measured strengths, and these can be used for comparison with ^{70}As. The $9^+ \rightarrow 8^+$ strengths of transitions in several nuclei including ^{70}As are shown in Fig. 4.16. These nuclei were chosen because they have a known $B(M1; 9^+ \rightarrow 8^+)$ and also because they all have the same isospin as ^{70}As, in order to try to make as direct a comparison as possible. They also all originate from a 9^+ state found to be a member of the $\pi g_{9/2}\nu g_{9/2}$ multiplet. As can be seen, all of the nuclei shown in Fig. 4.16 have a very similar strength as that measured in ^{70}As except for ^{66}Ga. This data

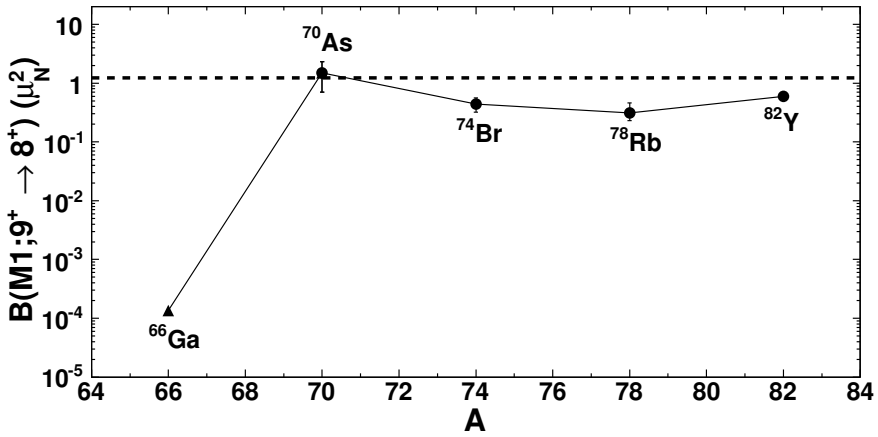

Figure 4.16: A plot of $B(M1; 9^+ \rightarrow 8^+)$ of several nuclei close to (and including) ^{70}As, as well as the strength predicted by the particle-vibration coupling model expressed in Eq. 4.3. All of the isotopes shown in the figure are believed to have a 9^+ state belonging to the $\pi g_{9/2} \nu g_{9/2}$ configuration. Most of the transition strengths in the figure are similar to that measured in ^{70}As in this work, which indicates that ^{70}As also has a 9^+ state which is a part of the $\pi g_{9/2} \nu g_{9/2}$ multiplet. The outlier is ^{66}Ga, which has a significantly smaller strength. However, this point is tentative because it is not certain that the decay is of an $M1$ nature, and this may explain the discrepancy. Figure is from [64], and data are taken from [82, 83, 84, 85].

point is, however, tentative, in that it is known that it is a dipole transition [86] but not necessarily that it is of $M1$ character. The apparent discrepancy of this point with the others in Fig. 4.16 may therefore lie in the fact that it could be an $E1$ transition. It could also be that the transition is of $M1$ character, but that the 9^+ state of ^{66}Ga is not well-described by a $\pi g_{9/2} \nu g_{9/2}$ configuration. More information would be necessary to make a statement about this situation. The remaining points in Fig. 4.16, however, show comparable strengths to that measured in ^{70}As, which indicates that it shares with them a similar structure. The dashed line indicates the strength calculated from the particle-vibration coupling model discussed earlier for comparison, which also demonstrates that it does a reasonable job of reproducing the strengths of these nuclei. Overall, this comparison further supports that the 9^+ state of ^{70}As belongs to the $\pi g_{9/2} \nu g_{9/2}$ configuration.

Chapter 5

Lifetime Measurements in ^{74}Rb

The second lifetime study presented in this work utilizes the Differential Recoil Distance Method (DRDM). As mentioned in Sec. 2.3, this is the first time that the DRDM has been successfully implemented, due in large part to the superior energy resolution of the next-generation γ-ray detector array GRETINA (Sec. 3.2.2.3). The physics goal of the study was to measure the lifetime of the 2_1^+ state of $^{74}_{37}\mathrm{Rb}_{37}$, thereby making this the heaviest odd-odd $N = Z$ nucleus with a measured $B(E2)$. This nucleus can be produced by a unique reaction path involving charge exchange reactions at intermediate energies [32, 87] and therefore has a small production cross-section. Thus, it was anticipated that the statistics for this measurement would be low. However, as discussed in Sec. 2.3, the DRDM is well-suited to such measurements as it requires fewer counts to make a lifetime measurement compared to the well-known (non-differential) Recoil Distance method. The ^{74}Rb 2_1^+ lifetime therefore provides an excellent case to demonstrate the utility of the DRDM. However, unlike the γ-γ coincidence lineshape analysis performed in Ch. 4, the DRDM produces several Doppler-shifted components for each deexcitation γ ray, and therefore requires a relatively clean spectrum with a wide separation between γ-ray decay energies compared to the dense level scheme of ^{70}As. It is also sensitive to lifetimes considerably shorter (a few picoseconds) than would normally be accessible to the lineshape method (several tens of picoseconds) under the typical fast beam conditions at the NSCL. Therefore, the DRDM is a technique complementary to the lineshape method, rather than a competing alternative.

5.1 Physics motivation

The physical motivation for undertaking this study was to measure the lifetime of the 2_1^+ state in ^{74}Rb. As this state decays to the 0^+ ground state of ^{74}Rb, the γ-ray decay is of an $E2$ nature, and so the lifetime of the 2_1^+ state can be used to calculate the $B(E2; 2^+ \rightarrow 0^+)$ of the transition. As discussed in Ch. 1, $B(E2)$ transition strengths are often used when discussing the collectivity of a nucleus and can be used to infer information about its shape. However, in the case of ^{74}Rb, there is a complication involved which makes such a discussion less clear. This complication is a phenomenon known as *shape coexistence* [88, 89], and determining whether it is present in ^{74}Rb forms the primary basis for making the measurement reported herein. This is of interest for understanding the structure of the ^{74}Rb nucleus itself, but also has implications for other physics interests as well. For instance, ^{74}Rb is one of a few nuclei that have very precisely measured superallowed Fermi beta decay strengths (also referred to as ft-values) used to test the conserved vector current (CVC) hypothesis and the unitarity of the Cabibbo-Kobayashi-Maskawa (CKM) matrix [90]. Such tests rely critically on nuclear structure corrections for their analyses, and so it is important to provide accurate nuclear structure inputs for these nuclei, including information about the wavefunctions themselves. A full discussion of the CVC hypothesis and the unitarity of the CKM matrix is beyond the scope of this work, but more information can be found in Refs. [91, 92]. It is important to note, however, that the data provided by this work can also provide information about the wavefunctions and therefore the structure of the ^{74}Rb nucleus, which is important for properly correcting for the nuclear structure effects in these tests of fundamental physics.

Shape coexistence occurs when a nucleus has available to it two or more different configurations with distinct shapes which are separated by only a small difference in energy

(typically about 1 MeV or less). Because of their close proximity, these two configurations are said to "coexist" with each other. However, the coexistence of these two different configurations has a consequence, which is that the wavefunctions of the states that belong to the two different configurations can mix via some interaction between them. Then, the states which are observed physically have wavefunctions which are superpositions of the wavefunctions of the "intrinsic" states which belong purely to one configuration or the other. The mixing causes one state to be lowered in energy while the other is raised.

Shape coexistence may be predicted in a number of ways. One is an examination of the Nilsson orbits calculated in a given region. Figure 5.1 shows the neutron single-particle orbitals calculated for the self-conjugate nucleus ^{80}Sr in the Nilsson scheme [93]. Inspection of these orbitals shows that, as expected, when the quadrupole deformation parameter β is zero, there are energy gaps between the single-particle energies at the canonical magic numbers. However, when the nucleus takes on some non-zero deformation, these gaps begin to close and new ones to appear at different particle numbers. Of particular interest to this discussion is the occurence of gaps at almost equal energy but opposite sign of the deformation parameter at nucleon numbers 36 and 38. This suggests that in nuclei which possess $N \approx Z \approx 36 - 38$, there may be competition between these two gaps and this can lead to shape coexistence. Another very useful tool for predicting the occurence of shape coexistence is the potential energy surface of a nucleus as a function of the quadrupole deformation parameter β and the triaxiality parameter γ. As discussed in Sec. 1.2.3, these calculations can be used to predict the shape of a nucleus. It can also happen that there may be multiple minima in these potential energy surfaces, which serves as another strong indicator of shape coexistence. Figure 5.2 shows such potential energy surfaces for ^{72,74,76}Kr, where the numbers along the contours give the depth of the potential in MeV. All three nuclei

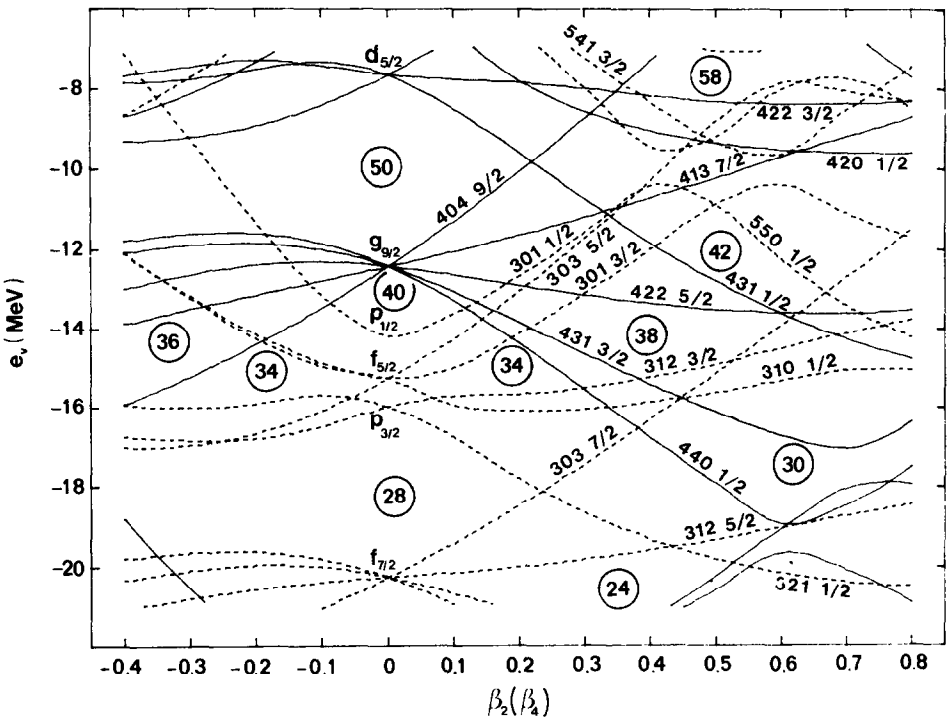

Figure 5.1: The single-particle energy levels for ^{80}Sr in the Nilsson model, calculated for neutrons but which will be similar for protons in $N \approx Z$ nuclei. The horizontal axis shows the quadrupole deformation parameter β, while the single-particle energies are plotted along the vertical axis. While the usual gaps at the magic numbers are present at $\beta = 0$, new gaps arise at non-zero values of the deformation. In particular, gaps at roughly the same energy appear at neutron number 36 and 38, but corresponding to opposite signs of the deformation. This can be a signature that shape coexistence may occur in nuclei that have proton and neutron numbers similar to these values. Figure is taken from [93].

clearly have multiple minima, one of which is prolate and the other oblate, while in ^{72}Kr the prolate minimum also has a degree of triaxiality with $\gamma \approx 15^\circ$. This suggests that these krypton isotopes exhibit shape coexistence, in agreement with the argument based on the gaps in the Nilsson orbitals in Fig. 5.1.

Experimentally, often a signature of shape coexistence is the observation of low-lying excited 0^+ states above the ground 0^+ state (in even-even nuclei). These excited 0^+ states can be considered as a kind of "alternative ground state" which might have become yrast had the energy of the various configurations been different. These 0^+ states typically also have

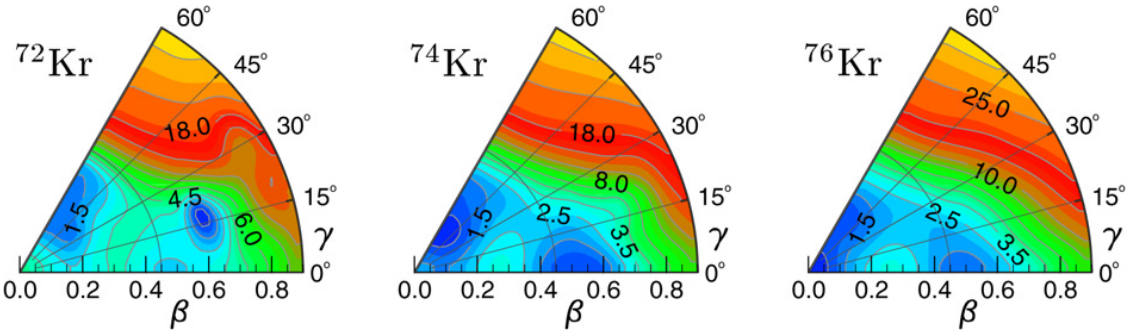

Figure 5.2: Potential energy surfaces generated for ^{72,74,76}Kr. As described in Ch. 1, the β axis gives the quadrupole deformation. Values of $\gamma = 0°$ or $\gamma = 60°$ correspond to prolate and oblate deformation, respectively, while intermediate values of γ indicate triaxiality. All three krypton isotopes clearly exhibit multiple minima, with a fairly strong prolate deformation as well as a weaker oblate minimum. ^{72}Kr also has some slight triaxiality associated with its prolate minimum. Figure taken from [94].

excited state bands built upon them. However, if the ground band mixes with an excited band, then it is usually the 0^+ states which mix most strongly, as the $J(J+1)$ energy dependence of the excited states of the two bands (assuming they are axially deformed) causes progressively greater energy separation between pairs of levels of the same J^π and hence less mixing. This causes an interruption of the regular $J(J+1)$ spacing at low-spin, and can be taken as an indication of mixing. However, the regular spacing at higher energies can be used to extrapolate down to find the locations of the bandheads if there was no mixing, and from this both the mixing matrix element and the amplitude of each of the pure configurations in the mixed states can be deduced. Figure 5.3 shows the results of such a calculation for the even-even krypton isotopes from mass $A = 72$ to mass $A = 78$ [95, 96]. For each nucleus, a few low-lying states are drawn divided into those belonging to prolate shapes on the left and oblate or spherical on the right. Also drawn is the location at which the 0^+ states associated with each shape would be found if there was no mixing. Starting with ^{78}Kr, the intrinsic states start far apart, and so there is only a small amount of mixing and repulsion. However, the intrinsic states become closer together in the lighter isotopes

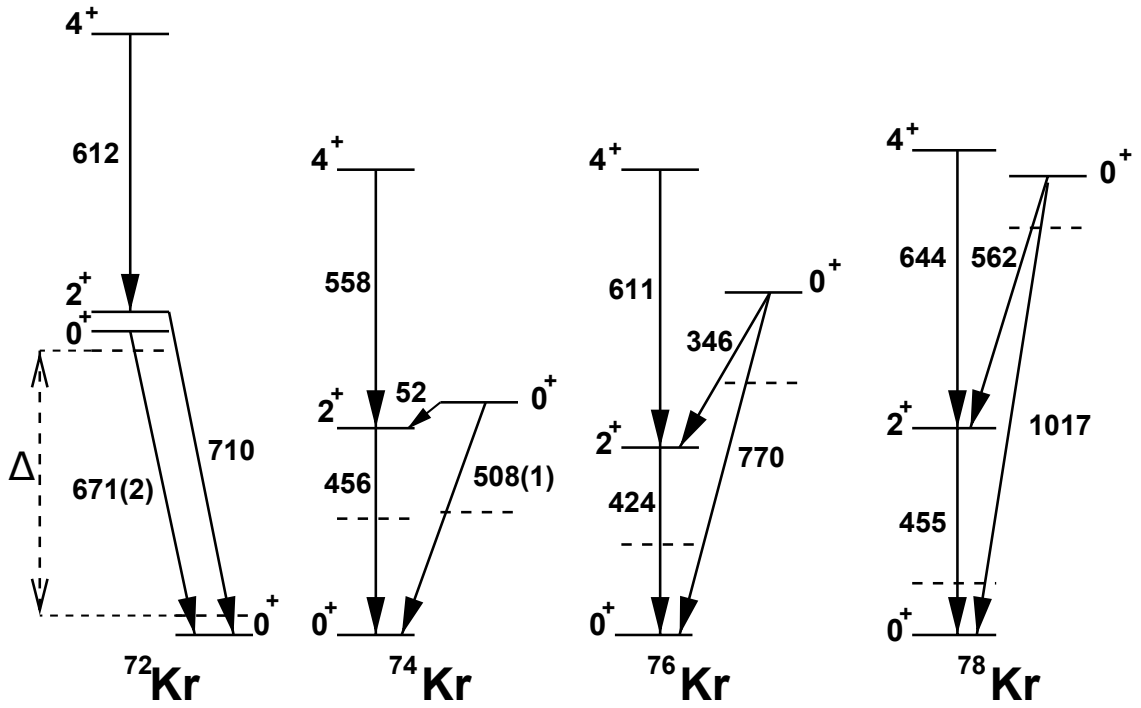

Figure 5.3: Several partial level schemes for even-even proton-rich krypton isotopes, showing the systematics of the low-lying levels. For each isotope, the set of levels on the left is associated with a prolate shape, while the 0^+ level on the right is an oblate or spherical shape. In addition to the levels themselves, the positions at which the 0^+ states would be located if there was no mixing between them are indicated by the dashed horizontal lines. These unperturbed levels become almost degenerate at ^{74}Kr, at which point the mixing has become almost maximized. The observed 0^+ states are therefore almost even mixtures of the intrinsic prolate and oblate shapes. Figure is from [95].

and even switch places in ^{72}Kr, so that the oblate state becomes the ground state. Table 5.1, which is taken from [95], summarizes the mixing of the intrinsic states in these nuclei. In ^{74}Kr, the two intrinsic states become almost degenerate, and this corresponds to almost the maximum possible mixing of the two intrinsic configurations, with half of the wavefunction amplitude coming from the prolate shape and half from the oblate shape.

Turning now to the question concerning the work presented in this chapter, namely that of shape coexistence in ^{74}Rb, the krypton isotopes just discussed offer a convenient entry point. In Ch. 1, the concept of isospin was introduced. The nuclei ^{74}Rb and ^{74}Kr are isobars with $T_z = 0$ and $T_z = 1$, respectively. Since this allows both nuclei to have states with $T = 1$,

Nuclide	Δ' [MeV]	Δ [MeV]	V [MeV]	b^2
^{78}Kr	1.01718(3)	0.80(1)	0.31(1)	0.11(2)
^{76}Kr	0.7700(2)	0.36(1)	0.34(1)	0.27(1)
^{74}Kr	0.508(1)	-0.02(1)	0.25(1)	0.52(1)
^{72}Kr	0.671(1)	-0.54(1)	0.20(1)	0.90(1)

Table 5.1: A summary of the values for the mixing of the 0^+_{gs} and 0^+_2 states for the isotopes of krypton shown in Fig. 5.3, taken from Ref. [95]. The energy difference between the observed states is given by Δ', while the energy difference between the intrinsic states is given by Δ and the mixing matrix element is V. The amplitude of the prolate wavefunction in the 0^+_2 state is given by b^2.

there should be a subset of levels in both nuclei which have similar properties. In Fig. 5.4, which shows a few of the low-lying levels of ^{74}Kr and ^{74}Rb, it can be seen that several of these levels follow a similar pattern of excitation energy up to spin 8^+, and these have been proposed to be $T = 1$ isobaric analogue states in these nuclei. These analogue states should all share similar nuclear structure properties under the assumption of isospin symmetry, and therefore the fact that there is shape coexistence in ^{74}Kr means that ^{74}Rb ought to manifest shape coexistence as well. However, as can be seen in Fig. 5.4, there is no known excited 0^+ state in ^{74}Rb, despite numerous searches [98, 99, 100, 101, 102, 103]. As has been previously suggested, this most likely means that the level exists close to an excitation energy of 500 keV in the vicinity of or even below the 2^+_1 state and decays primarily or exclusively by the emission of internal conversion electrons, to which the previous studies were not sensitive. However, the non-observation of this 0^+ state makes it difficult to investigate to what extent it may manifest shape coexistence by the extrapolation method used in the krypton nuclei. Another method is therefore required to explore this matter further.

To solve this problem, the study presented in this chapter was designed to measure the lifetime of the 2^+_1 state in ^{74}Rb. This is a useful measurement to make because the transitions

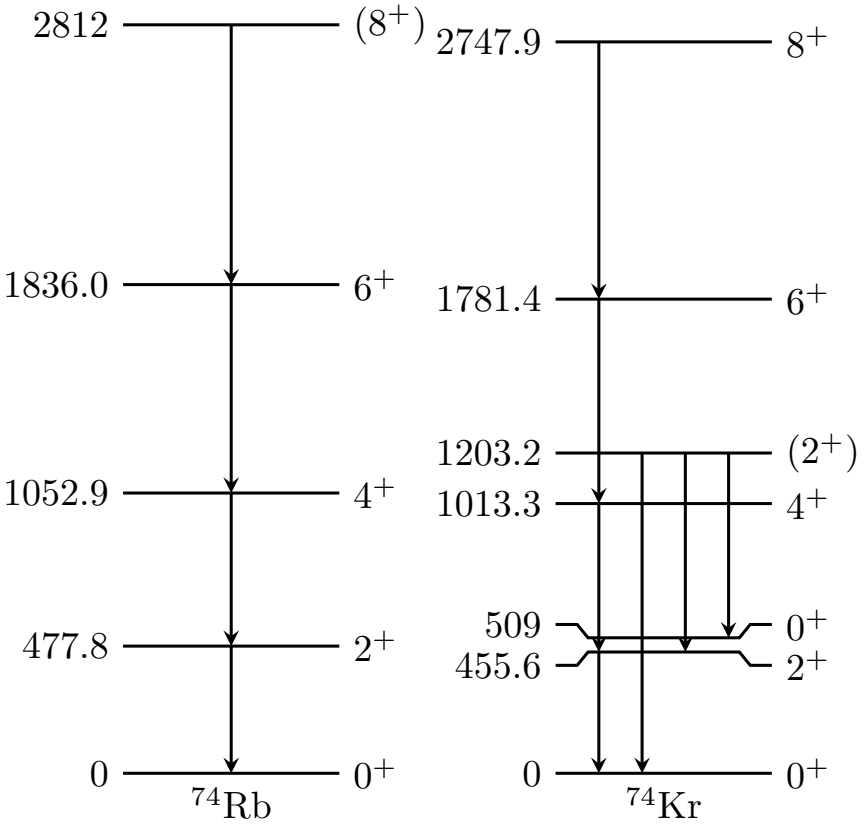

Figure 5.4: A partial level diagram of the low-lying $T = 1$ states in ^{74}Rb and ^{74}Kr. Level energies in keV are shown to the left of the states, while the spin-parities are given on the right. The isobaric analogue states can be identified based on the similar excitation energies up to spin 8^+. However, there is no known excited 0^+ state in ^{74}Rb which would be the analogue of the excited 0^+ state in ^{74}Kr. Data for ^{74}Kr are taken from [97], while data for ^{74}Rb are from [98].

between the isobaric analogue states should share similar properties. In particular, the quadrupole transition strength of the analogue $2_1^+ \rightarrow 0_1^+$ decays should be very similar due to isospin symmetry, and the lifetime can be used to calculate the strength. However, there is a caveat to this last statement about the equivalence of the transition strengths. If the matrix element M governing the transition is expressed in terms of isospin, then it is due to a sum of two terms [104]:

$$M(T_z) = \frac{1}{2}[M_0 - T_z M_1], \tag{5.1}$$

where M_0 is called the *isoscalar* matrix element and M_1 is called the *isovector* matrix element. In the $T_z = 0$ nucleus of an isobaric triplet ($T = 1$), the matrix element arises from the isoscalar matrix element only, but the isovector component also contributes in the $T_z = \pm 1$ cases. Therefore, the statement that the transition strength $B(E2) = |M(T_z)|^2/(2J_i+1)$ should be roughly equivalent between the analogue states of the $T_z = 0$ and $T_z = 1$ members of an isobaric triplet is only true as long as the isovector matrix element is small compared to the isoscalar matrix element. It has been observed in other isobaric triplets, however, that the isovector matrix element is typically on the order of 10% of the isoscalar matrix element [105], and so this statement may be reasonably expected to be true in the case of the $A = 74$ nuclei as well.

As discussed in Ch. 1, the transition strength $B(E2)$ is related to the overlap of the initial and final states of the transition. This makes this quantity sensitive to the structure of the states and can be used to infer information about the occurence of shape coexistence. In ^{74}Kr, the lifetime of the 2_1^+ state has already been measured [106] and so the $B(E2)$ is known. Since isospin symmetry (and a small isovector contribution) would predict that the $B(E2; 2_1^+ \rightarrow 0_1^+)$ is nearly identical in these two nuclei, this can be used to predict the lifetime of the 2_1^+ state in ^{74}Rb. For this electric quadrupole transition, the transition strength is given by

$$B(E2) = \frac{816}{E_\gamma^5 \tau}\, e^2\mathrm{fm}^4, \tag{5.2}$$

where E_γ is given in units of MeV and τ is given in picoseconds, which yields a predicted lifetime for the 2_1^+ state in ^{74}Rb of about 26 picoseconds. However, if there is no shape coexistence, then the 0_1^+ and 2_1^+ states should have a much larger overlap because there is only one configuration involved, and so the $B(E2)$ should be larger (by a factor of ~ 2) and

the lifetime would then be about 13 picoseconds. These predictions therefore offer a metric by which to judge whether shape coexistence persists between these two nuclei, and motivate the measurement of the 2_1^+ state lifetime.

5.2 Experimental details

As with the data on ^{70}As, the data for this analysis was obtained from an experiment run at the NSCL. The primary beam was again ^{78}Kr at 150 MeV/nucleon and 25 pnA. The secondary beam was produced by fragmentation on a ^{9}Be target and ^{74}Kr was selected in the A1900 with the aid of an aluminum wedge and 0.5% momentum acceptance. The resulting beam had an intensity of roughly 1×10^5 particles per second and a purity of about 40%. For this experiment, the timing signals from the object scintillator were not sufficiently well-separated to resolve the beam components, and so the radio frequency (RF) timing signal from the cyclotrons was used instead of the object scintillator to identify the components of the secondary beam. Figure 5.5 shows the timing signal from the A1900 extended focal plane (xfp) scintillator plotted against the RF signal from the cyclotrons. Software gates were used to isolate the ^{74}Kr from the contaminants in the beam during offline analysis. The beam was then directed to the S800 vault where the lifetime measurement was performed.

Once in the S800 vault, the secondary beam was caused to undergo further reactions in order to produce ^{74}Rb. The beam was directed to the target location of the S800 just in front of the large analyzing dipole magnets where the TRIPLEX plunger (c.f. Sec. 3.2.3) was installed in the beam line. The TRIPLEX held three metallic foils in this experiment: a 138-mg/cm^2 ^{9}Be target used to induce reactions, a 208-mg/cm^2 $^{\mathrm{nat}}$Ta degrader to reduce the beam velocity, and a 166-mg/cm^2 second $^{\mathrm{nat}}$Ta second degrader to slow the beam further.

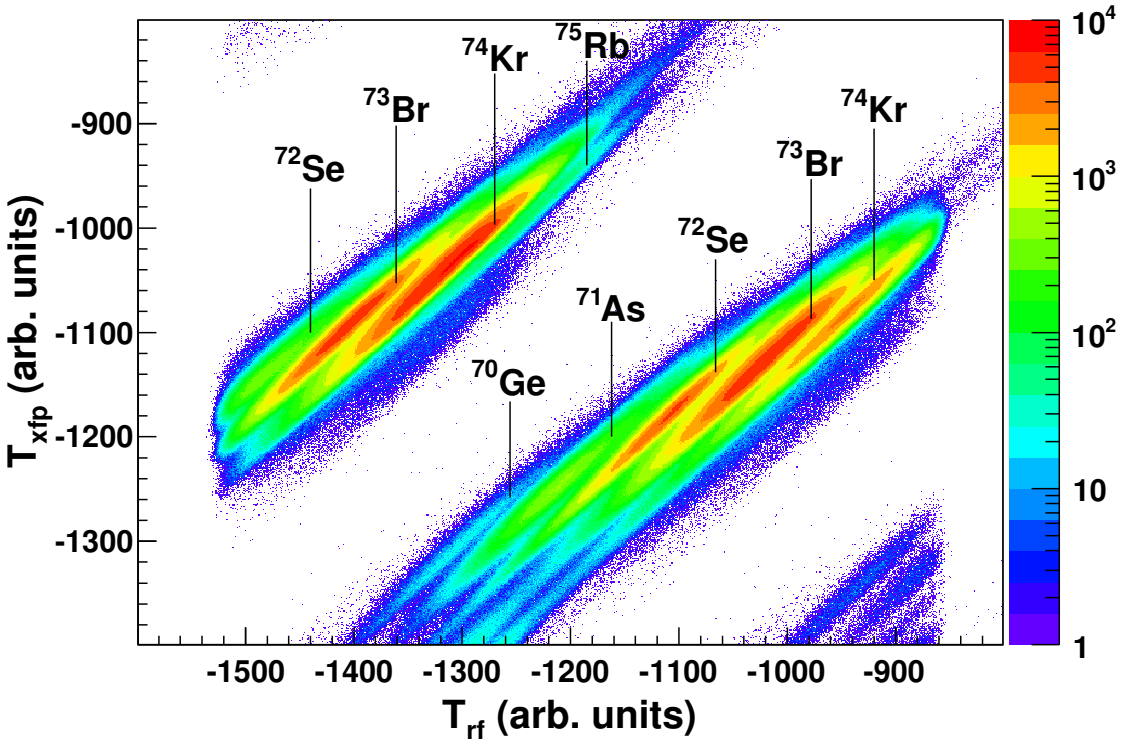

Figure 5.5: The particle identification plot for the ^{74}Rb experiment. The vertical axis gives the timing difference between the A1900 xfp scintillator and the S800 E1 scintillator while the horizontal axis is the time difference between the radio frequency (RF) signal from the cyclotrons and the E1 scintillator.

Behind the second degrader, a 7-mg/cm^2 thick foil made of polyethylene was installed in order to improve the charge-state distribution of reaction products. The beam then entered the analyzing dipoles in the S800 and were directed into the focal plane where the reaction residues were identified. Figure 5.6 shows the fragments identified by their energy loss in the S800 ionization chamber (ΔE) plotted against their time of flight between the E1 scintillator and the A1900 xfp scintillator ($T_{\rm xfp}$). The energy loss resolution in this experiment was not as high as in the ^{70}As experiment, however, it was still sufficient to identify the fragments. The location of the unreacted ^{74}Kr beam as well as ^{74}Rb reaction products are indicated by the ellipses in the figure, and software gates were used to select these species in the analysis.

The γ rays emitted from the beam after interactions with the target were detected with

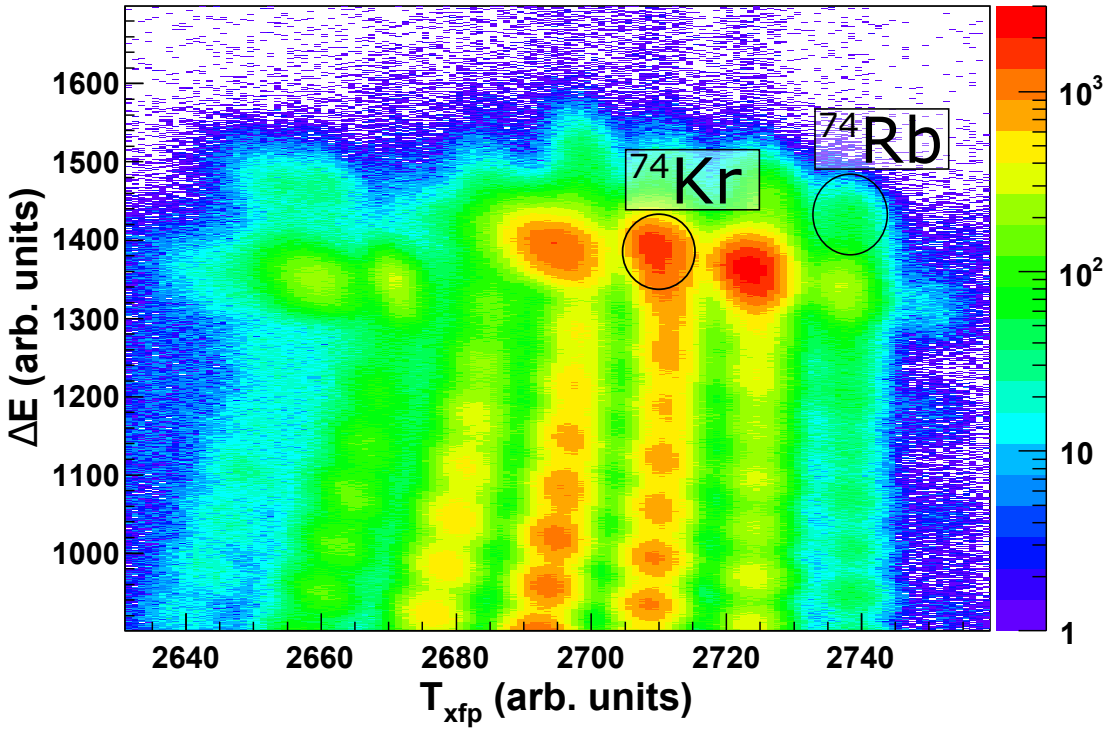

Figure 5.6: The outgoing particle identification plot for the ^{74}Rb experiment. The vertical axis gives the energy loss in the S800 ionization chamber while the horizontal axis gives the time of flight between the A1900 xfp scintillator and the S800 E1 scintillator. As in Fig. 4.2, the horizontal axis is reversed so that increasing time of flight indicates decreasing A/Z. The unreacted ^{74}Kr beam as well as the ^{74}Rb reaction products are labeled and indicated by the position of the ellipses in the figure.

the GRETINA detector array (Sec. 3.2.2.3). The seven detector modules of GRETINA were configured with four detectors in the most forward positions and the remaining three around 90° with respect to the beam axis. The TRIPLEX plunger was moved upstream from the nominal target position at the center of GRETINA in order to shift the angular coverage of GRETINA towards more forward angles, since these will show the most sensitivity to Doppler shifting at different velocities. With this plunger placement, the forward detectors covered roughly $20° - 50°$ with respect to the beam axis, and the remaining three detectors were centered around 70°. In addition, thin sheets of lead and copper were installed on the faces of the GRETINA modules in order to attenuate X-rays from the tantalum degraders,

which were observed with high intensity during the experiment. Data were taken for γ rays in coincidence with ^{74}Rb detected in the S800 focal plane as well as for ^{74}Kr. The ^{74}Kr was used as a reference measurement to demonstrate the validity of the DRDM, since it had not been implemented previously. For each nucleus, data were taken with a separation of 1 mm between the target and the first degrader and between the two degraders. A short time was also spent taking data for both nuclei with the separation between the target and the first degrader increased to 10 mm in order to quantify how many reactions are occurring in the degraders compared to the target (see Sec. 5.4.1 for a detailed discussion).

A possible concern regarding the lifetime measurement of the 2_1^+ state in ^{74}Rb arises from the potential feeding of this state by the predicted 0_2^+ state. Assuming that it lies near about 500 keV as the analogue state in ^{74}Kr does, any γ decay that it experiences to the 2_1^+ state of ^{74}Rb would have an energy of $\sim$ 20 keV, which would be stopped in the absorbers placed over the GRETINA modules even if it is not highly converted into electron emissions. This means that the possible effect of feeding from this state to the 2_1^+ state cannot be observed. However, this is not a large concern, as the analogue 0_2^+ state in ^{74}Kr has a lifetime of 20.5(14) ns [107]. Under the assumption of isospin symmetry, the 0_2^+ state in ^{74}Rb should have a similar lifetime. For the present experiment, it takes only about 20 ps for the beam to travel from the target position to the second degrader position, and so the majority of the possible population of the 0_2^+ state should decay far downstream from the TRIPLEX. As a consequence, the γ-ray spectrum should not be strongly sensitive to this lifetime and so it should not have a large effect on the 2_1^+ state lifetime measurement.

5.3 γ-ray spectra

The γ-ray spectra used to determine the lifetimes of the 2_1^+ states in ^{74}Rb and ^{74}Kr will be discussed in this section. While the placement of the GRETINA modules allowed γ rays to be observed at angles up to nearly 90° with respect to the beam axis, those γ rays emitted nearly perpendicular to that axis will have a Doppler shift which is least sensitive to the velocity at which the nucleus is moving. Since the DRDM relies critically on this velocity difference, these γ rays are not useful for the present analysis. Therefore, all of the spectra shown in this section include only those γ rays which are detected at an angle relative to the beam axis of less than 40°. This allows sufficiently large separation between the photopeaks originating from emission after each of the foils mounted in the TRIPLEX.

Figure 5.7 shows the γ-ray spectrum obtained in coincidence with ^{74}Kr nuclei detected in the S800 focal plane. Transitions can be seen in these spectra which correspond to the $6_1^+ \rightarrow 4_1^+$ decay, the $4_1^+ \rightarrow 2_1^+$ decay, and the $2_1^+ \rightarrow 0_1^+$ decay. In addition, the three-peaked structure necessary for the DRDM can be clearly seen in the inset to panel (b) of the figure, although for the 10 mm data in panel (a) most of the nuclei decay before reaching the degraders and so only the fast peak is obvious. These spectra show that ^{74}Kr is well-suited for demonstrating the validity of the DRDM, as each of the transitions shown in Fig. 5.7 originates from a state that has a known lifetime. The lifetime of the 2_1^+ state can therefore serve as an excellent test case, both by analyzing the $2_1^+ \rightarrow 0_1^+$ transition alone as well as analyzing the effects of feeding on this state.

The γ rays from ^{74}Rb are shown in Fig. 5.8. As with ^{74}Kr, the spectra have been divided into data which were taken with a separation of 10 mm between the target and first degrader in panel (a) and data which were taken with a separation of 1 mm between the

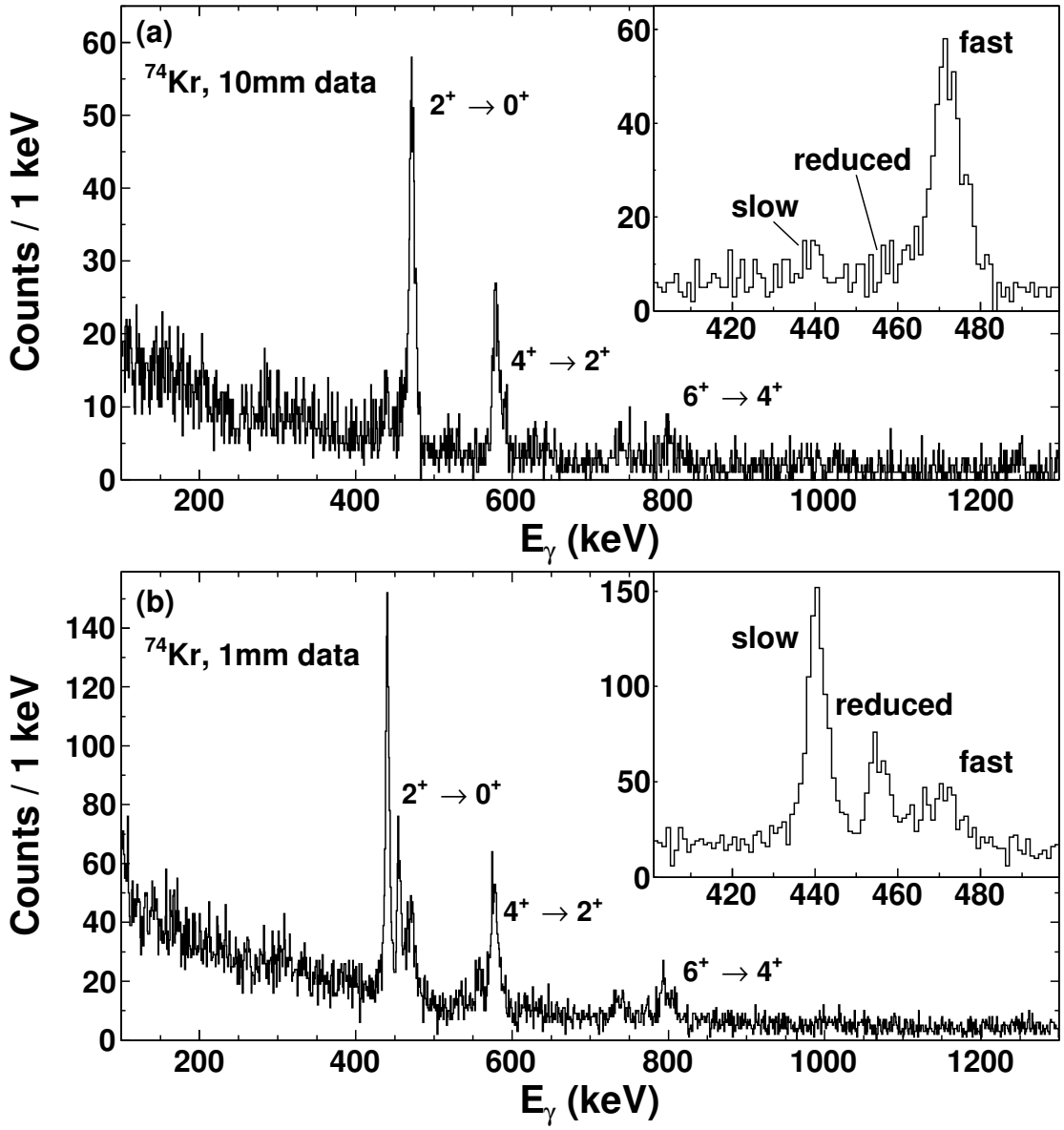

Figure 5.7: The γ-ray spectra obtained in coincidence with ^{74}Kr nuclei in the S800 Spectrograph. Panel (a) shows data taken with a 10 mm separation between the target and first degrader, while panel (b) shows data taken with only a 1 mm separation. In both panels, transitions can be clearly identified which correspond to the $2_1^+ \rightarrow 0_1^+$ transition, the $4_1^+ \rightarrow 2_1^+$ transition, and the $6_1^+ \rightarrow 4_1^+$ transition, and are labeled accordingly. The insets to each panel show the same spectra focused on the $2_1^+ \rightarrow 0_1^+$ transition to make clear the three-peaked structure, where the components of the decay from fast, reduced velocity, and slow recoils are also labeled.

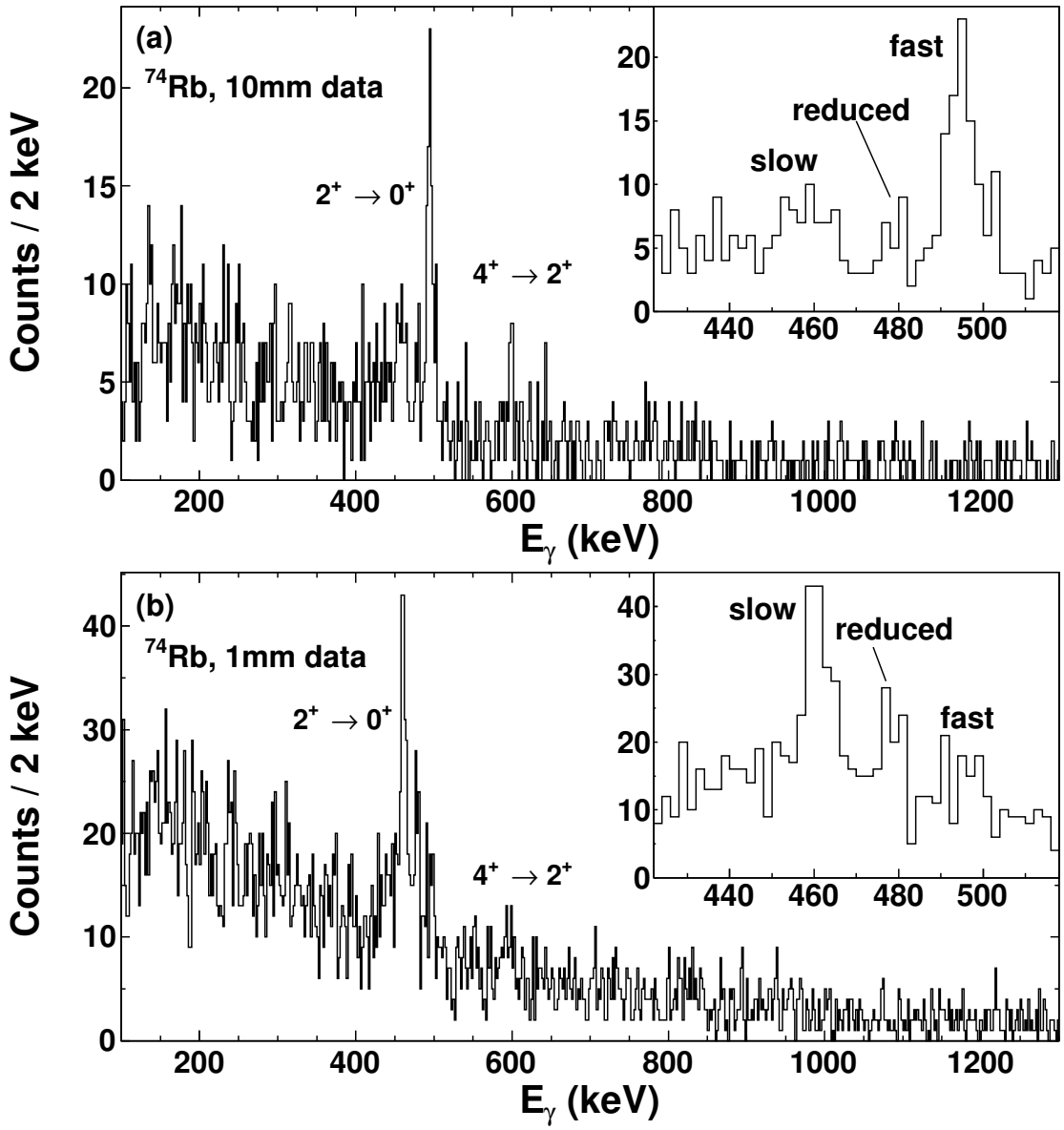

Figure 5.8: The γ-ray spectra obtained in coincidence with ^{74}Rb detected in the S800 focal plane, again divided into (a) data taken with 10 mm separation between the target and the first degrader and (b) 1 mm separation between target and degrader. The insets again focus on the $2_1^+ \rightarrow 0_1^+$ transition to show the three-peak structure. However, unlike for ^{74}Kr, there is very little population of states above the 2_1^+ state. A hint of the $4_1^+ \rightarrow 2_1^+$ transition can be seen at the position labeled in the figure, but no other transitions can be identified.

target and first degrader in panel (b), with the insets showing the $2_1^+ \rightarrow 0_1^+$ transition in greater detail. A striking difference between these data and those for ^{74}Kr is that the ^{74}Rb data have much lower statistics. As noted in Sec. 2.3, the DRDM is well-suited for such low-production rate experiments compared to the classic RDM method because it does not require multiple measurements in order to extract a lifetime. Another difference between the ^{74}Rb and ^{74}Kr data is that the ^{74}Rb spectra do not show strong population of excited states above the 2_1^+ state. There is some evidence for population of the 4_1^+ state, but it is very small and considerably less than in ^{74}Kr. This means that the analysis of the ^{74}Rb data will be simplified since feeding will not have a major impact on the 2_1^+ state lifetime measurement.

5.4 Lifetime analysis

Unlike the ^{70}As measurement presented earlier, once the γ-ray spectra were obtained very little additional processing was necessary before proceeding to the analysis. This is partially due to the relative simplicity of the low-energy level schemes of ^{74}Kr and ^{74}Rb, but is also a feature of the DRDM. To show the transparency of the method, a rough estimate of the lifetime of the 2_1^+ states in ^{74}Kr and ^{74}Rb can be obtained from Eq. 2.30. From the insets to Fig. 5.7(b) and Fig. 5.8(b), the ratio of the yield of the slow peak to that of the reduced velocity peak for both nuclei was $I_s/I_r \approx 3$. The velocity of the recoils between the two degraders was $v' \approx 0.35c = 0.1$ mm/ps, and the separation between the two degraders was $\Delta x = 1$ mm. Following Eq. 2.30, the lifetime of the 2_1^+ states can then be estimated to be:

$$\tau = \frac{\Delta x}{v'} \frac{I_{ij}^s}{I_{ij}^d} \approx \frac{1 \text{ mm}}{0.1 \text{ mm/ps}} \times 3 = 30 \text{ ps}. \tag{5.3}$$

This value is roughly consistent with the known value of $\tau = 33.8(6)$ ps [106], giving a reasonable estimate for the unknown lifetime of ^{74}Rb. For a more thorough analysis, the extraction of the 2_1^+ state lifetimes from the γ-ray spectra was performed using Geant4 simulations. Although the method as it is described in Sec. 2.3 does not require the use of simulations to perform a lifetime measurement, the use of simulations does offer certain advantages. In particular, the DRDM hinges critically upon the ability to measure the lifetime of a state using only the two photopeaks coming from decays after the first and second degraders. However, this is motivated by the approximation that the slope of the decay curve is linear in the space between the two degraders, while in actuality it is exponential. By simulating the transport of the ions through the TRIPLEX plunger as they decay, this approximation is in effect folded into the simulated spectra. Using simulations to determine the lifetime therefore corrects for the assumptions inherent in the method and allows the lifetime to be determined in a self-consistent way. It also takes into account the experimental lineshape of the peaks, possible decays occurring inside the foils, and other similar small effects which can affect the lifetime measurement. Feeding effects, if present, can also be included. The material in this section will show the details of the analysis, including the setup of the simulations and the fitting of the simulated γ-ray spectra to the data.

5.4.1 Geant4 simulations

As with the measurements performed on ^{70}As, the first step in the analysis is to set up the simulations. This setup proceeded very much as was described already for ^{70}As in Sec. 4.4.1, and so will only be summarized here. The GRETINA detectors were installed at the NSCL as part of a campaign of experiments and so the location was determined by the laboratory staff and provided to experimenters. This information and the dimensions of GRETINA

were used to fix the location of the detectors in the simulation. The beam properties were determined in exactly the same fashion as for ^{70}As, and the agreement between the simulated and measured beam properties are shown in Fig. 5.9 for ^{74}Kr and Fig. 5.10 for ^{74}Rb.

The chief difference in preparing the simulations between the analysis presented in this chapter and that in Ch. 4 is that with the DRDM it is possible that some of the incoming beam particles react not with the target as desired but instead react with the degraders. Therefore, it is necessary to constrain the relative number of reactions occurring on the target, the first degrader, and the second degrader. This is typically done by moving the foils mounted on the plunger far apart, so that there is ample time after each foil for the excited states to decay completely before the next foil is reached. Any counts observed in a given peak can then be assigned unambiguously to reactions happening on the corresponding foil. This information is provided to the simulation software as the fraction of reactions occurring on the target, and the fraction of the remaining reactions occurring on the first degrader. To fix these values for this experiment, the spectra in Fig. 5.7(a) and Fig. 5.8(a) were analyzed. The number of counts observed at a Doppler shift corresponding to decays after the target compared to those after the two degraders was used to determine the fraction of the reactions happening in the target. This was determined to be about 90% for the ^{74}Kr data and about 80% for the ^{74}Rb data. Due to a mechanical failure in the drive controlling the position of the second degrader, data with a large separation between the two degraders could not be taken during the experiment. Therefore, the ratio of the reactions happening on the first degrader compared to the second was fixed to the ratio of the thickness of the two degraders for both ^{74}Kr and ^{74}Rb, which was about 55%.

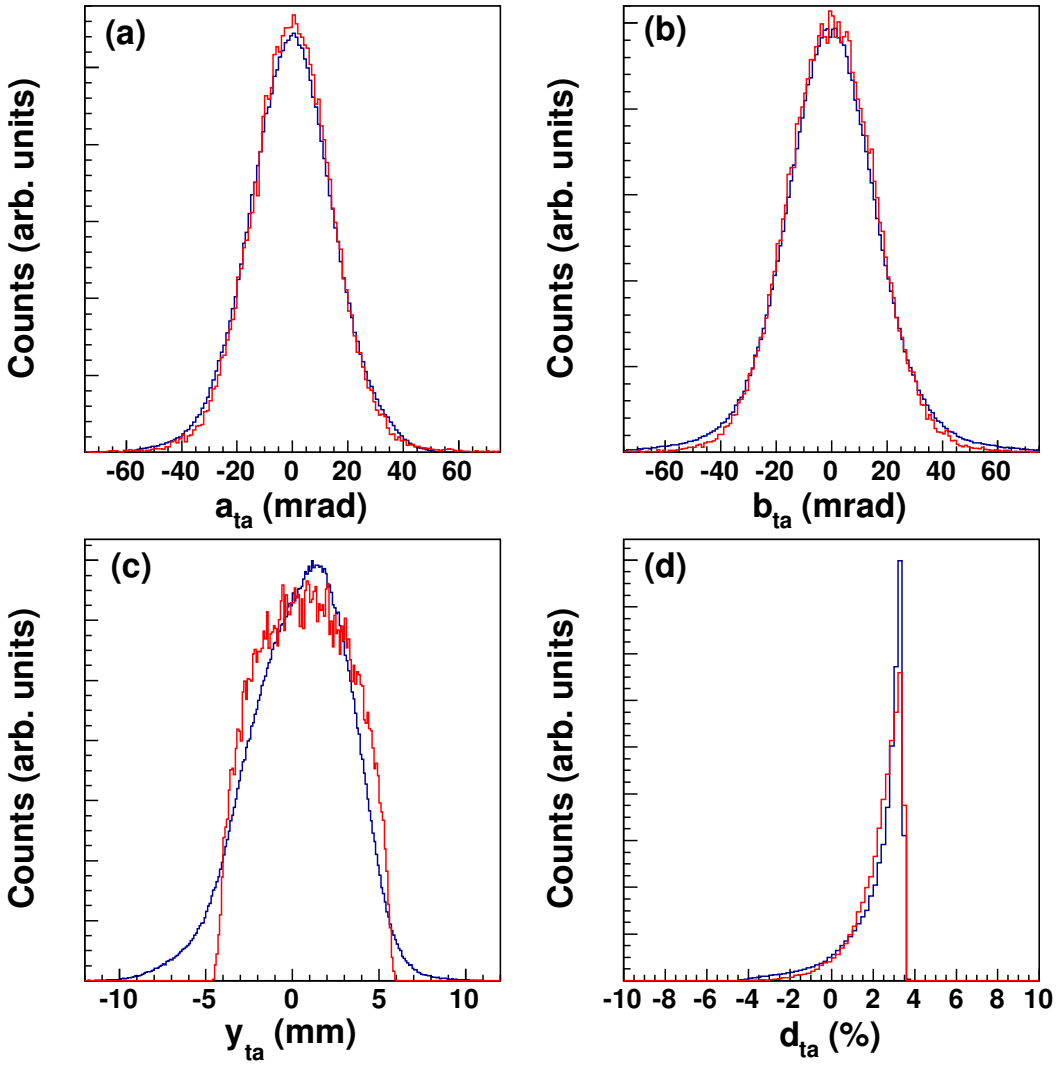

Figure 5.9: A comparison between the measured (blue) and simulated (red) beam properties. Panel (a) shows the angle of the beam in the dispersive direction, while panel (b) shows the angle in the non-dispersive direction, and both are reproduced well. As with ^{70}As, the position of the beam in the non-dispersive direction shown in panel (c) is not reproduced well because the beam is assumed to be circular in the simulation, but in reality may have any spatial distribution. The spread in the energy is shown in panel (d), and is reproduced well.

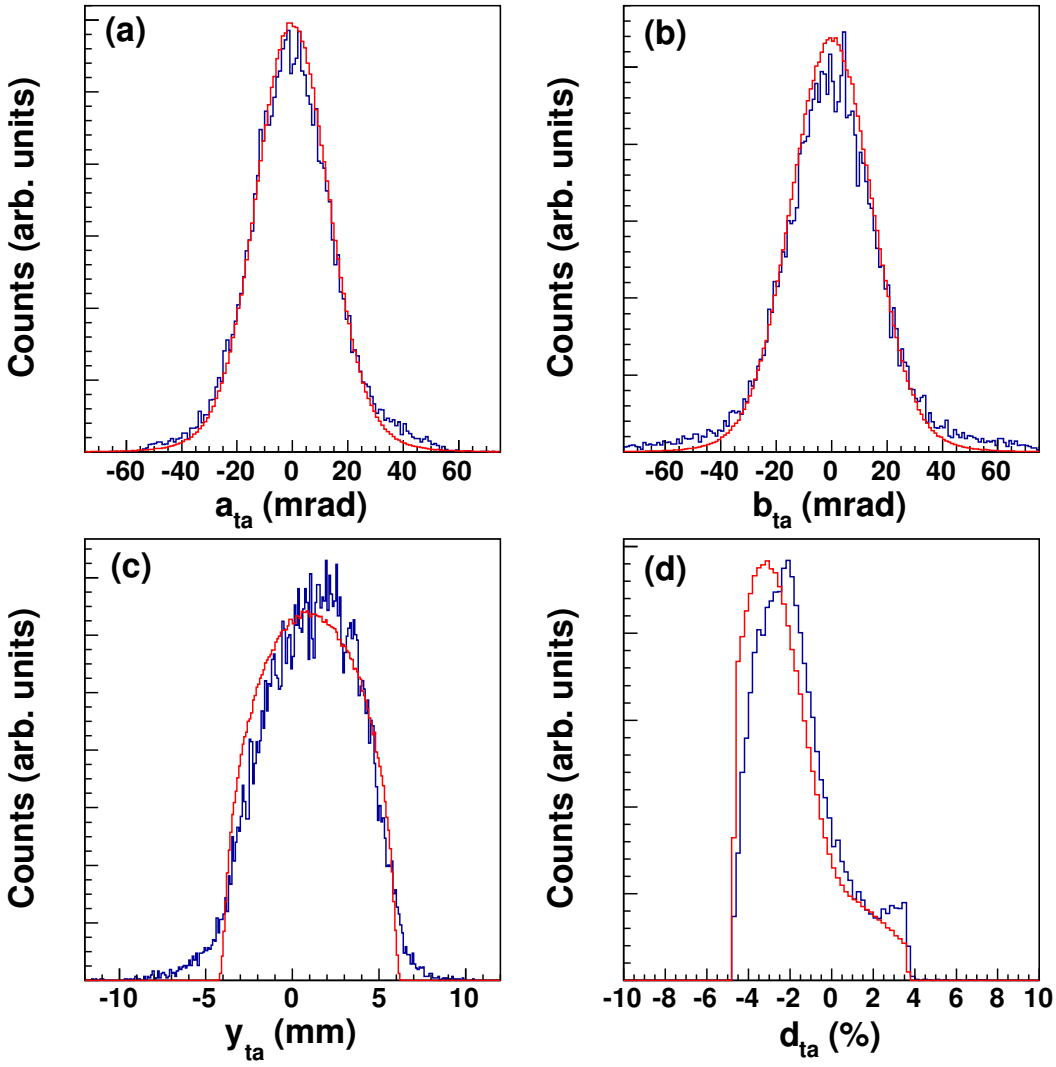

Figure 5.10: A comparison of the simulated and measured beam properties for ^{74}Rb, shown in red and blue, respectively. As for the ^{74}Kr beam, the dispersive and non-dispersive angular distributions shown in panels (a) and (b), respectively, are reproduced well, while the non-dispersive position has a different distribution in the data than is assumed in the simulation. The spread in beam energies about the central value shown in panel (d) is reproduced well.

5.4.2 Lifetime determination

After preparing the simulations, determining the lifetimes of the 2_1^+ states in ^{74}Kr and ^{74}Rb was accomplished by generating a set of simulated γ-ray spectra for each nucleus with the lifetime varying in a range from 0 ps to 50 ps. These simulations were then fit to the data along with a background which was assumed to be exponential. In accordance with the DRDM, only the peaks from the reduced and slow velocity recoils were fit, while the fast component was excluded from the fitting region. For each simulation with a given lifetime, a χ^2 value was extracted, then the distribution of χ^2 values was plotted and the minimum used to extract the lifetime. The following shows the results of this analysis for each of the two nuclei in question.

The analysis of ^{74}Kr was performed first in order to validate the DRDM. The 2_1^+ state has a lifetime of 33.8(6) ps [106], and so should lie within the range of lifetimes that was simulated. As noted previously, a significant amount of feeding is present in the spectrum obtained for ^{74}Kr, and so this data can also test how accurate the method is under these conditions. First, the data was fit using only simulations that included the 2_1^+ state, and did not account for feeding from higher-lying states. An advantage of using the DRDM is that this should give a result that is close to the true value. However, because there is significant feeding, there should be an excess of counts in the target component in the simulations compared to the data. This is because the lifetime of higher-lying states will delay the population of a portion of the 2_1^+ state, so that fewer decays from this state happen before the first degrader. Figure 5.11 shows the results of this fit. As can be seen in the figure, the slow and reduced velocity components are reproduced very well in this fit. However, the fast component is overestimated considerably in the simulations, as expected given the observed

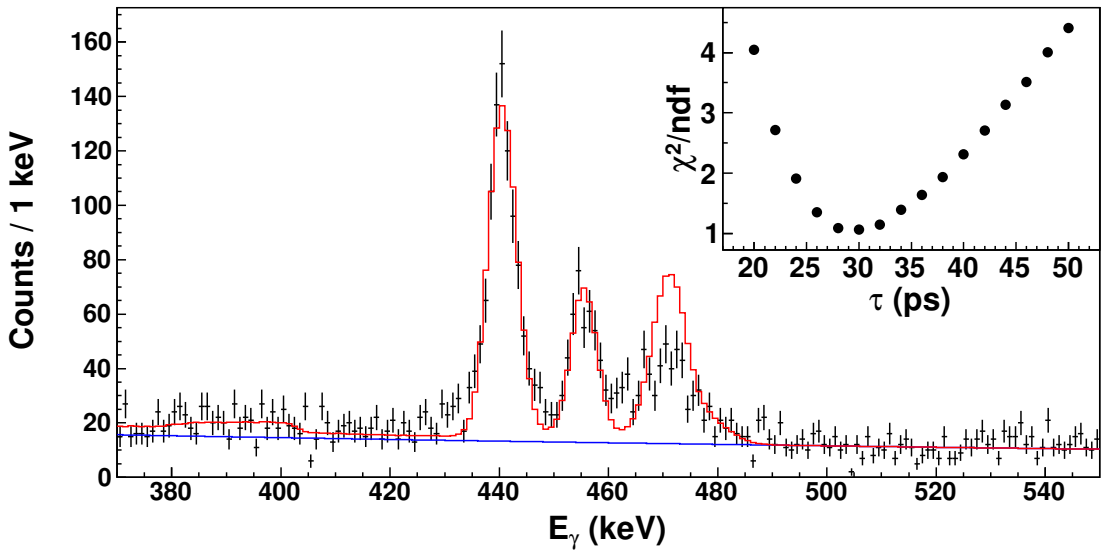

Figure 5.11: The results of fitting the simulated γ-ray spectra to the ^{74}Kr γ-ray spectrum. The data points are shown in black, while the simulation is shown in red and the background is shown in blue. The slow and reduced velocity components of the data are reproduced well by the simulation, but the fast component is not. This is expected, as the observed feeding from higher-lying states should produce a deficit of counts in this peak relative to the simulations. The inset shows the distribution of reduced χ^2 values obtained by varying the lifetime in the simulations, and the minimum of this distribution gives a lifetime of $\tau = 30.6(20)$ ps, with 15 degrees of freedom in the fit.

feeding. The inset in the figure shows the distribution of reduced χ^2 values which has a clear minimum. The lifetime extracted from this distribution is $\tau = 30.6(20)$ ps. Compared to the accepted literature value of $\tau = 33.8(6)$ ps [106], this result is consistent within two standard deviations, and demonstrates that the DRDM is giving accurate results.

To verify that it is actually the effects of feeding that are causing the overproduction of the fast component of the simulation shown in Fig. 5.11, the higher-lying states can also be included in the simulations. Doing so should reduce the contribution of the fast component relative to that of the other two peaks and result in a simultaneous reproduction of all three components. Figure 5.12 shows the result of fitting the ^{74}Kr data with simulations that include the 2_1^+, 4_1^+, 6_1^+, and 2_2^+ states as well as the feeding among them. The 2_2^+ state was

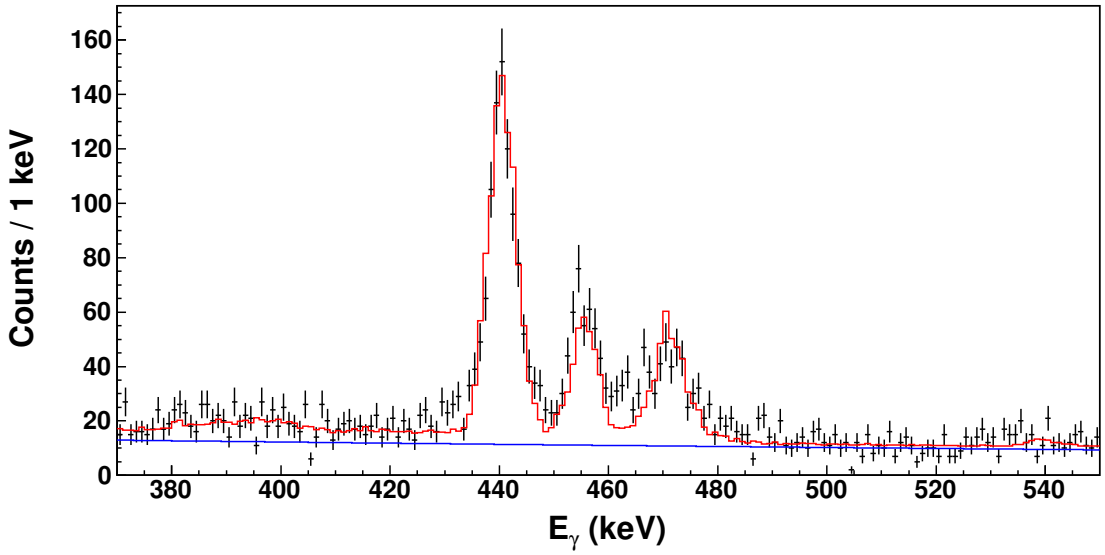

Figure 5.12: The results of fitting the ^{74}Kr γ-ray spectrum with simulations that include the effects of feeding from the 4_1^+ and 6_1^+ states. The 2_2^+ state was also included, but observed to contribute almost nothing to the fit. In this figure, the lifetime was not varied, but the literature value of $\tau = 33.8$ ps [106] was used and all three peaks were included in the fitting region. Now all three peaks are reproduced simultaneously, in contrast to Fig. 5.11, which demonstrates that all three components can be reproduced if feeding is taken into account.

included to account for any possible population of this state, but is extremely small. For this fit, instead of searching for a best-fit spectrum by varying lifetimes, the literature value of $\tau = 33.8$ ps was used for the 2_1^+ state lifetime to generate the simulations in this figure. Also, the fitting region was extended to include all three peaks. It is clear from looking at this spectrum that all three peaks are reproduced well when the feeding from higher-lying states is included, and confirms that the DRDM is performing as expected.

With the method validated, the lifetime of the 2_1^+ state of ^{74}Rb was analyzed. Since no significant feeding was observed in the data, it can be expected that even though only the slow and reduced velocity peaks are included in the fitting range, the fast peak should automatically be reproduced by the simulations if the lifetime is correctly determined. The simulations were fit to the data and the reduced χ^2 values plotted and used to determine

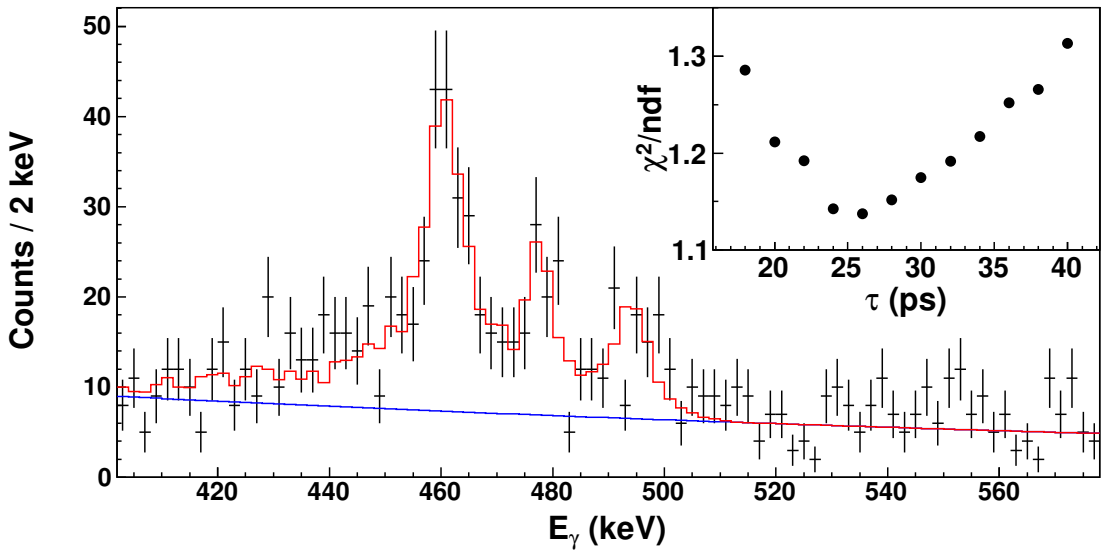

Figure 5.13: The results of the fit to the ^{74}Rb data. The data points are shown in black, while the red line shows the best-fit simulation and the blue line shows the assumption of the background. All three peaks are reproduced in this fit even though only the slow and reduced velocity components are fit, which shows that feeding is not a strong contributor in this analysis. The inset shows the reduced χ^2 distribution, where the number of degrees of freedom is 19, and the minimum of the distribution gives the lifetime as $\tau = 26.7(60)$ ps.

the lifetime. Figure 5.13 shows the results this analysis, with the data shown by the black points and the simulation shown by the red solid line. The blue curve shows the assumed exponential background. As expected, all three peaks are correctly reproduced, confirming that there is no significant impact on the 2_1^+ state lifetime from feeding. The distribution of reduced χ^2 values is shown in the inset, and the minimum gives a lifetime of $\tau = 26.7(60)$ ps.

5.5 Results and discussion

With the lifetime of the 2_1^+ state of ^{74}Rb measured, it is possible to discuss the physical meaning of the result. As mentioned in Sec. 5.1, isospin symmetry requires that the characteristics of the 2_1^+ states of ^{74}Rb and ^{74}Kr be similar. This led to the prediction that, based on the previously measured $2_1^+ \rightarrow 0_1^+$ transition strength measured in ^{74}Kr, the lifetime of

the 2_1^+ state in ^{74}Rb should be about 26 ps. This prediction is born out by the results of this study. This suggests that, similarly to ^{74}Kr, ^{74}Rb exhibits shape coexistence in its ground state, and likely there is a similar amount of mixing between its ground state and the excited 0^+ state that is hypothesized to exist at about 500 keV.

In order to have a quantitative discussion of the results of this study, it is useful to discuss the $2_1^+ \rightarrow 0_1^+$ transition strength in ^{74}Rb instead of the lifetime. From Eq. 5.2, the transition strength can be calculated to be $B(E2; 2_1^+ \rightarrow 0_1^+) = 1227(276)\ e^2\text{fm}^4$. The two-state mixing model described earlier in this chapter can be used to investigate to what extent this result indicates mixing of intrinsic shapes. This can be done by formulating the transition strength in terms of the overlap of the wavefunctions of the intrinsic states. For the intrinsic wavefunctions of the 0^+ and 2^+ states of the different configurations, this would be written as

$$\begin{aligned} |0^+\rangle &= \cos\theta_0 |0_p^+\rangle + \sin\theta_0 |0_o^+\rangle \\ |2^+\rangle &= \cos\theta_2 |0_p^+\rangle + \sin\theta_2 |0_o^+\rangle, \end{aligned} \tag{5.4}$$

where $\theta_{0,2}$ is the mixing angle between the 0^+ or 2^+ states, respectively, and $|0_p^+\rangle$ denotes the intrinsic wavefunction of the 0^+ state belonging to the prolate configuration while $|0_o^+\rangle$ represents the same for the oblate configuration. Then, the $B(E2; 2_1^+ \rightarrow 0_1^+)$ can be constructed by writing the overlap of these wavefunctions through the $E2$ transition operator:

$$\begin{aligned} B(E2; 2_1^+ \rightarrow 0_1^+) &= \frac{|\langle 0^+ || \mathcal{M}(E2) || 2^+ \rangle|^2}{2J_i + 1} \\ &= \frac{1}{5} |\cos\theta_0 \cos\theta_2 \langle 0_p^+ || \mathcal{M}(E2) || 2_p^+ \rangle + \sin\theta_0 \sin\theta_2 \langle 0_o^+ || \mathcal{M}(E2) || 2_o^+ \rangle|^2, \end{aligned} \tag{5.5}$$

where it has been assumed that the oblate and prolate intrinsic configurations are orthogonal

and therefore all terms such as $\langle 0_o^+ || \mathcal{M}(E2) || 2_p^+ \rangle = 0$. From this expression the mixing amplitudes $\cos^2\theta_0$ and $\cos^2\theta_2$ can be extracted if the transition strengths between the intrinsic configurations are known.

Unfortunately, a lifetime measurement of the 2_1^+ state alone is not enough to deduce the individual matrix elements on the right hand side of Eq. 5.5. However, an analysis was performed in Ref. [108] on ^{74}Kr in which the matrix elements $\langle 0_p^+ || \mathcal{M}(E2) || 2_p^+ \rangle$ and $\langle 0_o^+ || \mathcal{M}(E2) || 2_o^+ \rangle$ were determined from the experimental data, as well as the mixing amplitudes $\cos^2\theta_{0,2}$. The technique used in the study is known as Coulomb excitation [109] (more precisely, multiple Coulomb excitation), in which the nucleus is excited via the electromagnetic interaction with a high-Z material. This technique is sensitive to the shape of the nucleus through the so-called "reorientation effect," in which transitions occur between magnetic substates of an excited state which gives access to the quadrupole moment of the nucleus in that state. In order to discuss ^{74}Rb further, the assumption can be made that these matrix elements have the same values in ^{74}Rb as in ^{74}Kr. While this is a strong assumption, it is motivated by the expectation that isospin symmetry should preserve the structure between the isobaric analogues states of these nuclei. There is also indirect evidence to support this assumption, in that the $B(E2; 2_1^+ \rightarrow 0_1^+)$ values in these two nuclei are very similar, which in itself suggests that the structure of these states in these two nuclei remains the same. With this justification, the values of the matrix elements from [108] can be adopted here: $\langle 0_p^+ || \mathcal{M}(E2) || 2_p^+ \rangle = 114(15)\ e\text{fm}^2$ and $\langle 0_o^+ || \mathcal{M}(E2) || 2_o^+ \rangle = -21(27)\ e\text{fm}^2$. Since the oblate term is both small and consistent with zero, it can be neglected in Eq. 5.5, which becomes

$$B(E2; 2_1^+ \rightarrow 0_1^+) = \frac{1}{5} \cos^2\theta_0 \cos^2\theta_2 (114 e\text{fm})^2. \tag{5.6}$$

In Ref. [108], the term $\cos^2\theta_2 = 0.82(20)$, and therefore it is reasonable to set this value to unity in Eq. 5.6. With the experimental value of the $B(E2)$ measured in this work, the only undetermined quantity left is $\cos^2\theta_0$, which is the amplitude of the prolate configuration in the 0_1^+ state. Solving for this quantity, it is found that

$$\begin{aligned} \cos^2\theta_0 &= 0.47(16) \\ \sin^2\theta_0 &= 0.53(16), \end{aligned} \tag{5.7}$$

where the equation in $\sin^2\theta_0$ is the amplitude of the oblate configuration. These values indicate that the 0_1^+ state in ^{74}Rb is nearly an equal mixture between intrinsic prolate and oblate states. This is not a surprising result, as the assumptions made along the way essentially necessitate this conclusion. However, what is important to note is the uncertainty associated with these values, which indicates that even at the edge of the 1σ uncertainties, there is still at least a 30%-70% mixture of the intrinsic shapes in ^{74}Rb. Therefore, within the assumptions that have been made herein, this study provides good evidence for significant shape coexistence and configuration mixing in ^{74}Rb.

Unfortunately, relatively few theoretical predictions which have published a $B(E2; 2_1^+ \rightarrow 0_1^+)$ value exist for ^{74}Rb due to difficulties with performing detailed calculations in this mass region. One spherical shell model study was published that used a truncated model space of $f_{5/2}p_{1/2}g_{9/2}d_{5/2}$ (i.e. the $p_{3/2}$ orbital was omitted) and presented results for several $N = Z$ nuclei in this mass region, including ^{74}Rb [110]. The $B(E2; 0_1^+ \rightarrow 2_1^+)$ values from this study are shown in Fig. 5.14, which is taken from the paper. While a numerical value for the $B(E2)$ value for ^{74}Rb was not provided, from the figure the $B(E2; 0_1^+ \rightarrow 2_1^+)$ value can be estimated to approximately 0.22 $e^2\text{b}^2$. Noting that $B(E2; 2_1^+ \rightarrow 0_1^+) = \frac{1}{5}B(E2; 0_1^+ \rightarrow$

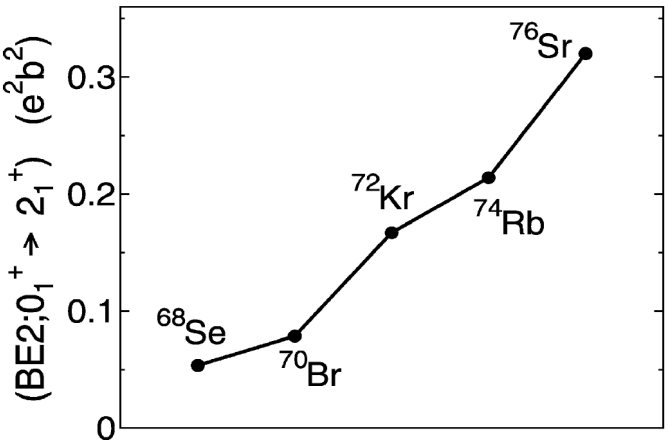

Figure 5.14: Theoretical $B(E2; 0_1^+ \rightarrow 2_1^+)$ values for several $N = Z$ nuclei calculated using the shell model with the $f_{5/2}p_{1/2}g_{9/2}d_{5/2}$ model space. The value for ^{74}Rb is underpredicted by roughly a factor of three, which the authors of the study note is due to the omission of the $p_{3/2}$ orbital. Figure taken from [110].

2_1^+), this corresponds to a calculated transition strength of $B(E2; 2_1^+ \rightarrow 0_1^+) \approx 440\ e^2\text{fm}^4$. This is considerably smaller than the experimentally measured value of 1227(276) $e^2\text{fm}^4$. However, the authors of the study note that their calculation underpredicts the other $B(E2)$ strengths in the figure as well, and attribute this to the omission of the $p_{3/2}$ orbital from the calculations. They make reference to another paper [111] in which the $pf_{5/2}g_{9/2}$ model space was used (i.e. the $d_{5/2}$ orbital was not included but the $p_{3/2}$ was) and note that the magnitude of the $B(E2)$ value calculated for ^{68}Se therein is increased by a factor of three compared to the present calculation without the $p_{3/2}$ orbital. Applying the same factor of three increase to the calculated strength estimated from Fig. 5.14 for ^{74}Rb gives $B(E2; 2_1^+ \rightarrow 0_1^+) \approx 1320\ e^2\text{fm}^4$, which is consistent with the value measured within this work. It would be informative to see the results of a calculation performed for ^{74}Rb with the $p_{3/2}$ orbital included to see whether this factor of three increase is justified.

A different approach to predict the $B(E2)$ strength can be taken by predicting the deformation parameter β of the nucleus and using Eq. 1.13 to convert this into a transition

strength. This procedure relies on the assumption that the nucleus is axially symmetric, which can justified if the characteristic $J(J+1)$ energy dependence is observed in the energy spectra. It then remains to find a suitable way to calculate the deformation parameter. Using a macroscopic-microscopic model, these deformation parameters have been calculated for an extremely wide range of nuclei in Ref. [112]. The macroscopic portion of the model used was the "finite range droplet model," which is essentially the well-known liquid-drop model [113] that models the nuclear binding energy with terms such as the volume, surface area, and charge of the nucleus, just as if it were a drop of charged liquid, but with refinements to account for the nuclear deformation. The microscopic portion of the model provides corrections to the macroscopic portion from shell effects and nucleon pairing and is based on a folded-Yukawa potential. A full discussion of these models, which is beyond the scope of this work, can be found in [112]. The result of this calculation, however, is a predicted deformation parameter of $\beta = 0.381$ for the ground state of ^{74}Rb. Putting this into Eq. 1.13 and using the typical choice that the nuclear radius is given by $R = 1.2A^{1/3}$ fm, this predicts a value of $B(E2; 2_1^+ \rightarrow 0_1^+) = 1459\ e^2\text{fm}^4$, which is in agreement with the experimental value of 1227(276) $e^2\text{fm}^4$ measured here. Values predicted by this model for several neighboring $N = Z$ nuclei are plotted in Fig. 5.15. For the most part, this model does well in reproducing the $B(E2)$ transition strengths for these nuclei, although it fails in the case of ^{70}Br. However, it should be noted that this macroscopic-microscopic model only calculates the ground-state deformation, and so it will not have any sensitivity to the higher-lying states and possible mixing between them and the ground state. Therefore, the results of this model in the particular case of ^{74}Rb should be interpreted with caution.

As a final remark about the comparison between the two models referenced above, while the details of the calculations may not be exactly correct, it is important to note that

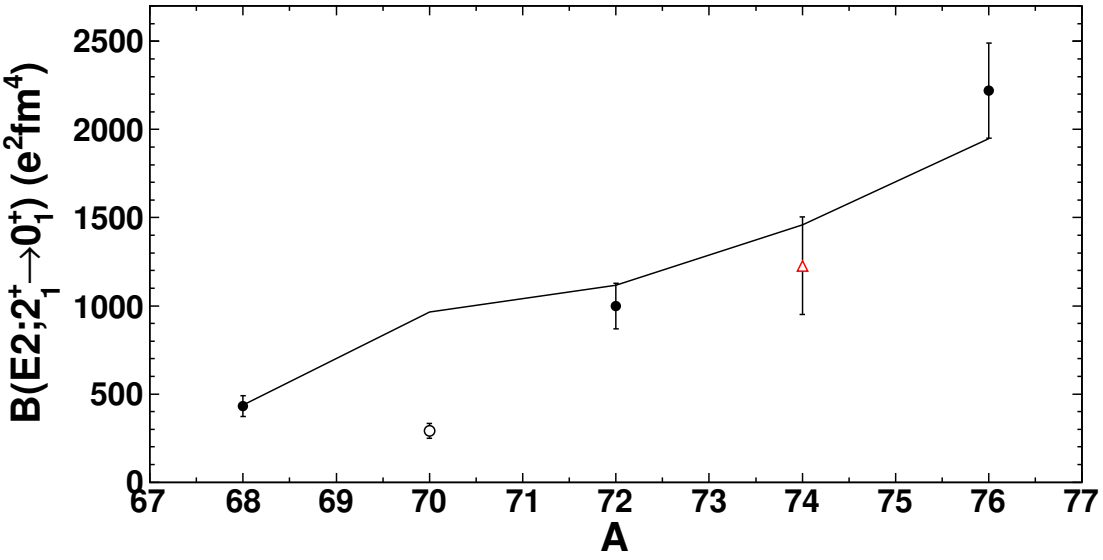

Figure 5.15: Systematics of the measured $B(E2)$ values for several $N = Z$ nuclei, where the even-even nuclei are indicated by the filled symbols and the odd-odd nuclei correspond to the open symbols. The red point is the $B(E2)$ value for ^{74}Rb measured in this work. These values are compared to the predictions calculated from the results of the macroscopic-microscopic model in [112] (solid line). Overall, the trend is reproduced well, although the prediction for ^{70}Br differs significantly from the measured value. Data are taken from [32, 60, 66, 114].

both models do correctly reproduce the overall trend of the $B(E2)$ values in this region. Specifically, for both the shell model and the macroscopic-microscopic model, there is a rapid rise in collectivity that begins around ^{72}Kr and continues through ^{76}Sr which is reflected in the increasing $B(E2)$ values predicted by both models (see Figs. 5.14 and 5.15). The macroscopic-microscopic model does predict that the increase in collectivity begins slightly earlier in ^{70}Br, at variance with the data, but the overall agreement is still fairly good. It will be very interesting to compare the results of these calculations with future theoretical predictions, e.g. that can account for the full fp model space while including the $g_{9/2}d_{5/2}$ orbitals as well.

Chapter 6

Concluding Remarks

In this work, two studies have been presented which used lifetime measurements to study the structure of rare isotopes, namely ^{70}As and ^{74}Rb. In both cases the data presented challenges to the analyses which required the use of advanced techniques in order to extract results from the experimental spectra. A summary of these studies is given here as well as a few words on the future prospects generated by this work before concluding.

For the ^{70}As experiment detailed in Ch. 4, data were taken with the intention of using the lineshape method to extract lifetimes based on the asymmetric photopeaks produced by long-lived states moving at relativistic speeds. However, the very high density of excited states in this odd-odd nucleus necessitated a more sophisticated analysis, as the presence of many photopeaks in close proximity introduced too much uncertainty into the determination of the lineshape. To remedy this situation, the lineshape method was extended to use γ-γ coincidence data in order to isolate the levels of interest, both from the perturbing effect of feeding and to remove the presence of any possible background peaks in the singles spectrum. While this improved the purity of the spectra greatly, as a consequence it reduced the statistics available for the analysis considerably. However, with careful analysis, it was possible to determine the lifetimes of the yrast 8^+ and 9^+ states. This study therefore constitutes an important tool in the arsenal of nuclear spectroscopy for measuring excited state lifetimes, particularly for complex spectra as is typical of odd-odd nuclei.

The physics goal of this study on ^{70}As was to provide a firmer experimental determination

of the configuration of the 8^+ and 9^+ states. As mentioned in Ch. 4, previous studies on this nucleus had suggested that these states arise from a coupling of both the last proton and the last neutron in $g_{9/2}$ orbitals. This was based on the energy systematics of levels in neighboring nuclei, however, and the lifetime measurements in this work were intended to provide an independent verification of this assignment. The results of these measurements support the assignment of the 8^+ and 9^+ states to the $\pi g_{9/2} \nu g_{9/2}$ configuration, based upon both the systematics of the reduced transition strengths calculated from the measured lifetimes, and upon the agreement with the prediction of a particle-vibration coupling model calculation.

The analysis of ^{74}Rb presented in Ch. 5 also presented an experimental challenge in that it is difficult to produce this nucleus in large quantities with the current generation of experimental facilities. To address this problem, this experiment implemented for the first time the Differential Recoil Distance Method (DRDM). The analysis of ^{74}Rb is well-suited to the use of the DRDM, as the technique is able to measure the lifetime of nuclear states with considerably lower γ-ray yields than more conventional Recoil Distance methods. The method was demonstrated to reproduce the measured lifetime of the 2_1^+ state of ^{74}Kr, which has been determined very precisely by previous measurements, and then successfully applied to the 2_1^+ state of ^{74}Rb. This analysis provides a way to retain the precision of the Recoil Distance Method while simultaneously increasing the economy of the measurement by reducing the number of counts necessary to determine the lifetime. This result therefore paves the way to access very exotic nuclei which previously could not be produced in sufficient quantities for lifetime measurements.

In addition to providing an opportunity to demonstrate the DRDM, the choice to measure the lifetime of ^{74}Rb offered the chance to obtain important physics information as well. In

the isospin partner nucleus ^{74}Kr, it is well known that shape coexistence is present and that this causes the two low-lying configurations that are present in this nucleus to experience strong mixing. Because of isospin symmetry, states that arise from the same structure should also be present in ^{74}Rb and their transitions should exhibit similar spectroscopic properties. As discussed in Ch. 5, these isobaric analogue states in ^{74}Rb had been identified, and the transition strength calculated from the lifetime measurement of the 2_1^+ state in this work agrees very well with the measured value in ^{74}Kr. This can be taken as an experimental indication that shape coexistence persists across the isospin triplet at mass 74. By making the assumption that the intrinsic shapes of the two coexisting configurations are the same, the degree of mixing in ^{74}Rb was also quantified and found to be consistent with the roughly equal mixing that occurs in ^{74}Kr, even with the relatively large uncertainty of $\sim 20\%$.

Finally, a few comments are offered about the future prospects that are raised by these two studies. The preceding paragraphs have already mentioned how the techniques presented in this work can facilitate the analysis of challenging data. However, it is also worth discussing the future physics interests that can be conceived based on this work. For ^{70}As, the origin of the 8^+ and 9^+ states in the $\pi g_{9/2}\nu g_{9/2}$ configuration was the sole focus, and little consideration was given to the possible shape that the nucleus may adopt. However, while it was mentioned that previous studies did not find strong evidence for deformation in the lower-lying states, with both the odd nucleons populating the deformation driving $g_{9/2}$ orbital a non-spherical shape might be expected. This can provide the motivation for future studies which are designed specifically to quantify the degree of variation from sphericity in the high-spin states of ^{70}As. Likewise, as was discussed in Ch. 5, the lifetime measurement on ^{74}Rb presented in this work can be used to infer the presence of shape coexistence, but cannot be used to directly determine its existence. However, future measurements specifi-

cally designed to detect the decay of the analogue of the excited 0^+ state in ^{74}Kr, specifically decays that proceed through the emission of conversion electrons, would provide more direct evidence of shape coexistence. In addition, a multiple Coulomb excitation experiment similar to the one used to determine the shapes and mixing of the intrinsic configurations similar to that reported in [108] for ^{74}Kr should provide clear evidence for shape coexistence. Future advances in experimental facilities may enable the successful use of these techniques in ^{74}Rb. Lastly, as mentioned at the end of Ch. 5, there are relatively few theoretical treatments of ^{74}Rb, and therefore future calculations that can reproduce the $B(E2; 2_1^+ \rightarrow 0_1^+)$ value for this nucleus are desirable.

In closing, lifetime measurements provide a sensitive probe of the structure and behavior of exotic nuclei. They can provide a measure of the collectivity of a nucleus and are sensitive to the wavefunctions of nuclear states. They are also model-independent and can serve as a valuable tool for benchmarking the results of nuclear theory as well as evaluating systematic trends in the data. The studies presented in this work demonstrate two advanced techniques for measuring excited state lifetimes which are suitable for challenging systems with complicated level schemes or low production cross sections. The methods were developed and used to study the 8^+ and 9^+ states in ^{70}As and the 2_1^+ state in ^{74}Rb, and the results used to understand the structure of these exotic nuclei.

BIBLIOGRAPHY

BIBLIOGRAPHY

[1] M. G. Mayer, Phys. Rev. **74**, 235 (1948).

[2] J. Erler, N. Birge, M. Kortelainen, W. Nazarewicz, E. Olsen, A. M. Perhac, and M. Stoitsov, Nature **486**, 509 (2012).

[3] W. Heisenberg, Z. Phys. **77**, 1 (1932).

[4] E. Wigner, Phys. Rev. **51**, 106 (1937).

[5] Y. Fujita, B. Rubio, and W. Gelletly, Prog. Part. Nucl. Phys. **66**, 549 (2011).

[6] M. G. Mayer and J. H. D. Jensen, *Elementary Theory of Nuclear Shell Structure* (John Wiley & Sons, New York, 1955).

[7] B. A. Brown and W. A. Richter, Phys. Rev. C **74**, 034315 (2006).

[8] T. Otsuka, Y. Utsuno, T. Mizusaki, and M. Honma, Nucl. Phys. A **685**, 100 (2001).

[9] E. Caurier, A. P. Zuker, A. Poves, and G. Martínez-Pinedo, Phys. Rev. C **50**, 225 (1994).

[10] B. A. Brown, "Lecture notes in nuclear structure physics," (2011).

[11] M. G. Mayer, Phys. Rev. **75**, 1969 (1949).

[12] O. Haxel, J. H. D. Jensen, and H. E. Suess, Phys. Rev. **75**, 1766 (1949).

[13] S. G. Nilsson, Mat. Fys. Medd. Dan. Vid. Selsk. **29**, 16 (1955).

[14] R. F. Casten, *Nuclear Structure from a Simple Perspective* (Oxford University Press, Inc., 200 Madison Avenue, New York, New York 10016, 1990).

[15] A. Bohr and B. R. Mottelson, *Nuclear Structure*, Vol. 1 (Benjamin, 1969).

[16] J. P. Delaroche, M. Girod, J. Libert, H. Goutte, S. Hilaire, S. Péru, N. Pillet, and G. F. Bertsch, Phys. Rev. C **81**, 014303 (2010).

[17] V. F. Weisskopf, Phys. Rev. **83**, 1073 (1951).

[18] K. Alder and R. M. Steffen, in *The Electromagnetic Interaction in Nuclear Spectroscopy*, edited by W. D. Hamilton (North-Holland Publishing Company, 1975) pp. 173–236.

[19] S. Raman, C. W. Nestor Jr., and P. Tikkanen, At. Data Nucl. Data Tables **78**, 1 (2001).

[20] P. J. Nolan and J. F. Sharpey-Schafer, Rep. Prog. Phys. **42**, 1 (1979).

[21] K. E. G. Löbner, in *The Electromagnetic Interaction in Nuclear Spectroscopy*, edited by W. D. Hamilton (North-Holland Publishing Company, 1975) pp. 173–236.

[22] Z. Bay, Phys. Rev. **77**, 419 (1950).

[23] T. K. Alexander and K. W. Allen, Can. J. Phys. **43**, 1563 (1965).

[24] D. B. Fossan and E. K. Warburton, in *Nuclear Spectroscopy and Reactions: Part C*, edited by J. Cerny (Academic Press, New York, 1974) pp. 307–377.

[25] A. Dewald, O. Möller, and P. Petkov, Prog. Part. Nucl. Phys. **67**, 786 (2012).

[26] P. Voss *et al.*, Phys. Rev. C **90**, 014301 (2014).

[27] K. W. Allen, in *The Electromagnetic Interaction in Nuclear Spectroscopy*, edited by W. D. Hamilton (North-Holland Publishing Company, 1975) pp. 311–339.

[28] W. M. Currie, Nucl. Instrum. Methods **73**, 173 (1969).

[29] J. Lindhard, M. Scharff, and H. E. Schiott, Mat. Fys. Medd. Dan. Vid. Selsk. **33**, 14 (1963).

[30] A. E. Blaugrund, Nucl. Phys. **88**, 501 (1966).

[31] P. Doornenbal *et al.*, Nucl. Instrum. Methods, Sect. A **613**, 218 (2010).

[32] A. Lemasson *et al.*, Phys. Rev. C **85**, 041303 (2012).

[33] A. Dewald, S. Harissopulos, and P. von Brentano, Z. Phys. A **334**, 163 (1989).

[34] P. Miller, F. Marti, D. Poe, M. Steiner, J. Stetson, and X. Wu, in *Proceedings of the 2001 Particle Accelerator Conference*, Vol. 4 (2001) pp. 2557–2559.

[35] D. J. Morrissey, Nucl. Phys. A **616**, 45 (1997).

[36] D. J. Morrissey, B. M. Sherrill, M. Steiner, A. Stolz, and I. Wiedenhoever, Nucl. Instrum. Methods, Section B **204**, 90 (2003).

[37] P. A. Zavodszky *et al.*, Nucl. Instrum. Methods, Sect. B **241**, 959 (2005).

[38] P. A. Zavodszky *et al.*, Rev. Sci. Instrum. **77**, 03A334 (2006).

[39] G. Machicoane, D. Cole, J. Ottarson, J. Stetson, and P. Zavodszky, Rev. Sci. Instrum. **77**, 03A322 (2006).

[40] D. Leitner and C. Lyneis, in *The Physics and Technology of Ion Sources*, edited by I. G. Brown (Wiley-VCH Verlag GmbH & Co. KGaA, 2005) 2nd ed., pp. 203–231.

[41] H. G. Blosser, IEEE Trans. Nucl. Sci. **NS-26**, 2040 (1979).

[42] C. K. Gelbke, Phys. Scr. **1990**, 107 (1990).

[43] G. D. Westfall, L. W. Wilson, P. J. Lindstrom, H. J. Crawford, D. E. Greiner, and H. H. Heckman, Phys. Rev. C **19**, 1309 (1979).

[44] J. P. Dufour, R. Del Moral, H. Emmermann, F. Hubert, D. Jean, C. Poinot, M. S. Pravikoff, A. Fleury, H. Delagrange, and K.-H. Schmidt, Nucl. Instrum. Methods, Sect. A **248**, 267 (1986).

[45] G. F. Knoll, *Radiation Detection and Measurement*, 4th ed. (John Wiley & Sons, Inc., 2010).

[46] D. Bazin, J. A. Caggiano, B. M. Sherrill, J. Yurkon, and A. Zeller, Nucl. Instrum. Methods, Sect. B **204**, 629 (2003).

[47] J. Yurkon, D. Bazin, W. Benenson, D. J. Morrissey, B. M. Sherrill, D. Swan, and R. Swanson, Nucl. Instrum. Methods, Sect. A **422**, 291 (1999).

[48] "S800 service level description," `http://nscl.msu.edu/_files/documents/s800_sld.pdf`, accessed February 6, 2015.

[49] K. Meierbachtol, D. Bazin, and D. J. Morrissey, Nucl. Instrum. Methods, Sect. A **652**, 668 (2011).

[50] M. Berz, K. Joh, J. A. Nolen, B. M. Sherrill, and A. F. Zeller, Phys. Rev. C **47**, 537 (1993).

[51] O. Klein and Y. Nishina, Z. Phys. **52**, 853 (1929).

[52] W. F. Mueller, J. A. Church, T. Glasmacher, D. Gutknecht, G. Hackman, P. G. Hansen, Z. Hu, K. L. Miller, and P. Quirin, Nucl. Instrum. Methods, Sect. A **466**, 492 (2001).

[53] "Sega service level description," `http://nscl.msu.edu/_files/documents/sega_sld_2007.pdf`, accessed February 10, 2015.

[54] K. Starosta *et al.*, Nucl. Instrum. Methods, Sect. A **610**, 700 (2009).

[55] S. Paschalis *et al.*, Nucl. Instrum. Methods, Sect. A **709**, 44 (2013).

[56] I. Y. Lee, M. A. Deleplanque, and K. Vetter, Rep. Prog. Phys. **66**, 1095 (2003).

[57] K. Wimmer and E. Lunderberg, "Grroot," `http://nucl.phys.s.u-tokyo.ac.jp/wimmer/software.php`, accessed April 9, 2015.

[58] R. Brun and F. Rademakers, Nucl. Instrum. Methods, Sect. A **389**, 81 (1997).

[59] H. Iwasaki *et al.*, Phys. Rev. Lett. **112**, 142502 (2014).

[60] A. J. Nichols *et al.*, Phys. Lett. B **733**, 52 (2014).

[61] S. Agostinelli *et al.*, Nucl. Instrum. Methods, Sect. A **506**, 250 (2003).

[62] P. Adrich, D. Enderich, D. Miller, V. Moeller, R. P. Norris, K. Starosta, C. Vaman, P. Voss, and A. Dewald, Nucl. Instrum. Methods, Sect. A **598**, 454 (2009).

[63] G. Cowan, *Statistical Data Analysis* (Oxford University Press, New York, 1998).

[64] C. Morse *et al.*, Phys. Rev. C **90**, 034310 (2014).

[65] K. Starosta *et al.*, Phys. Rev. Lett. **99**, 042503 (2007).

[66] A. Obertelli *et al.*, Phys. Rev. C **80**, 031304 (2009).

[67] K. Langanke, D. J. Dean, and W. Nazarewicz, Nucl. Phys. A **728**, 109 (2003).

[68] M. Honma, T. Otsuka, T. Mizusaki, and M. Hjorth-Jensen, Phys. Rev. C **80**, 064323 (2009).

[69] A. Filevich, M. Behar, G. Bermúdez, M. A. J. Mariscotti, E. der Mateosian, and P. Thieberger, Nucl. Phys. A **309**, 285 (1978).

[70] T. Bădică, V. Cojocaru, D. Pantelică, I. Popescu, and N. Scîntei, Nucl. Phys. A **535**, 425 (1991).

[71] G. García Bermúdez, J. Döring, G. D. Johns, R. A. Kaye, M. A. Riley, S. L. Tabor, C. J. Gross, M. J. Brinkman, and H. Q. Jin, Phys. Rev. C **56**, 2869 (1997).

[72] M. R. Bhat, Nucl. Data Sheets **58**, 1 (1989).

[73] J. K. Tuli, Nucl. Data Sheets **103**, 389 (2004).

[74] Zs. Podolyák, T. Fényes, and J. Timár, Nucl. Phys. A **584**, 60 (1995).

[75] D. Pantelica *et al.*, J. Phys. G **22**, 1013 (1996).

[76] J. Döring, D. Pantelică, A. Petrovici, B. R. S. Babu, J. H. Hamilton, J. Kormicki, Q. H. Lu, A. V. Ramayya, O. J. Tekyi-Mensah, and S. L. Tabor, Phys. Rev. C **57**, 97 (1998).

[77] P. M. Endt, At. Data Nucl. Data Tables **23**, 547 (1979).

[78] J. Döring, S. L. Tabor, J. W. Holcomb, T. D. Johnson, M. A. Riley, and P. C. Womble, Phys. Rev. C **49**, 2419 (1994).

[79] R. Anholt *et al.*, Phys. Rev. Lett. **53**, 234 (1984).

[80] Zs. Podolyák, P. H. Regan, P. M. Walker, M. C. ano, K. Gladnishki, J. Gerl, M. Hellström, P. Mayet, M. Pfützner, and M. Mineva, Nucl. Phys. A **722**, C273 (2003).

[81] M. Bogdanović *et al.*, Nucl. Phys. A **470**, 13 (1987).

[82] T. Bădică, V. Cojocaru, D. Pantelică, I. Popescu, and R. Ion-Mihai, Hyperfine Interact. **36**, 171 (1987).

[83] G. García-Bermúdez, M. A. Cardona, A. Filevich, R. V. Ribas, H. Somacal, and L. Szybisz, Phys. Rev. C **59**, 1999 (1999).

[84] R. A. Kaye, L. A. Riley, G. Z. Solomon, S. L. Tabor, and P. Semmes, Phys. Rev. C **58**, 3228 (1998).

[85] S. D. Paul, H. C. Jain, S. Chattopadhyay, M. L. Jhingan, and J. A. Sheikh, Phys. Rev. C **51**, 2959 (1995).

[86] E. Browne and J. K. Tuli, Nucl. Data Sheets **111**, 1093 (2010).

[87] A. Gade *et al.*, Phys. Rev. Lett. **102**, 182502 (2009).

[88] K. Heyde and J. L. Wood, Rev. Mod. Phys. **83**, 1467 (2011).

[89] A. Petrovici, K. Schmid, A. Faessler, J. Hamilton, and A. Ramayya, Prog. Part. Nucl. Phys. **43**, 485 (1999).

[90] J. C. Hardy and I. S. Towner, Phys. Rev. Lett. **94**, 092502 (2005).

[91] D. H. Wilkinson, Nucl. Instrum. Methods, Sect. A **488**, 654 (2002).

[92] J. C. Hardy and I. S. Towner, Phys. Rev. C **91**, 025501 (2015).

[93] W. Nazarewicz, J. Dudek, R. Bengtsson, T. Bengtsson, and I. Ragnarsson, Nucl. Phys. A **435**, 397 (1985).

[94] M. Girod, J. P. Delaroche, A. Görgen, and A. Obertelli, Phys. Lett. B **676**, 39 (2009).

[95] E. Bouchez *et al.*, Phys. Rev. Lett. **90**, 082502 (2003).

[96] F. Becker *et al.*, Eur. Phys. J. A **4**, 103 (1999).

[97] B. Singh and A. R. Farhan, Nucl. Data Sheets **107**, 1923 (2006).

[98] S. M. Fischer *et al.*, Phys. Rev. C **74**, 054304 (2006).

[99] J. M. D'Auria, L. C. Carraz, P. G. Hansen, B. Jonson, S. Mattsson, H. L. Ravn, M. Skarestad, and L. Westgaard, Phys. Lett. B **66**, 233 (1977).

[100] P. H. Regan *et al.*, Acta Phys. Pol. B **28**, 431 (1997).

[101] M. Oinonen *et al.*, Nucl. Phys. A **701**, 613 (2002).

[102] D. Rudolph *et al.*, Phys. Rev. Lett. **76**, 376 (1996).

[103] C. D. O'Leary *et al.*, Phys. Rev. C **67**, 021301 (2003).

[104] A. M. Bernstein, V. R. Brown, and V. A. Madsen, Phys. Rev. Lett. **42**, 425 (1979).

[105] P. D. Cottle, AIP Conf. Proc. **638**, 37 (2002).

[106] A. Görgen *et al.*, Eur. Phys. J. A **26**, 153 (2005).

[107] R. Dunlop *et al.*, Phys. Rev. C **88**, 045501 (2013).

[108] E. Clément *et al.*, Phys. Rev. C **75**, 054313 (2007).

[109] K. Alder and A. Winther, *Electromagnetic Excitation, Theory of Coulomb Excitation with Heavy Ions* (North-Holland, Amsterdam, 1975).

[110] M. Hasegawa, K. Kaneko, T. Mizusaki, and Y. Sun, Phys. Lett. B **656**, 51 (2007).

[111] K. Kaneko, M. Hasegawa, and T. Mizusaki, Phys. Rev. C **70**, 051301 (2004).

[112] P. Möller, J. R. Nix, W. D. Myers, and W. J. Swiatecki, At. Data Nucl. Data Tables **59**, 185 (1995).

[113] C. F. v. Weizsäcker, Z. Phys. **96**, 431 (1935).

[114] A. Gade *et al.*, Phys. Rev. Lett. **95**, 022502 (2005)